Development of Pd Based Alloy Catalysts Highly Selective for deNO$_x$ reactions

（deNO$_x$ 反応に高い選択性を示す Pd 系合金触媒の開発）

全 載完

Graduate School of Chemical Sciences and Engineering

Hokkaido University

2020

Contents

Chapter 1

General Introduction

1. General Introduction

1.1 Environmental issues of NO_x gases

Since the industrial revolution, the invention of internal combustion engines has benefited human development and civilization. The increasing dependence of internal combustion engines in the chemical plant and the automotive industry, resulting in an increase in the use of fossil fuels, increases the emissions of harmful gases every year. This is pointed out as a serious cause of environmental pollution.[1]

Exhaust emissions due to the combustion of fossil fuels are composed of carbon monoxide (CO), hydrocarbon (HC), nitrogen oxides (NO_x) and particulate matter (PM).[2] Among them, nitrogen oxide (NO_x) are usually generated from reaction among nitrogen and oxygen during combustion of fuels. Representative sources of NO_x are automobiles, aircraft, ships, industrial boilers, incinerators, and electric furnaces. NO_x is the main source of acid rain, ozone layer depletion, and photochemical smog.[3] Reacts with moisture in the atmosphere to produce nitric acid (HNO_3), which is the main cause of acid rain. N_2O, a well-known non-CO_2 gas, is a stable substance used as a medical anesthetic, but the Global Warming Potential is 310 times higher than CO_2.[4] N_2O destroys the ozone layer when decomposed by ultraviolet light in the stratosphere. The destruction of the ozone layer increases the influx of short wavelengths, which means that the amount of ultraviolet light that reaches the earth's surface is increased. Ultraviolet rays can cause skin cancer, cataracts, and can also damage plastic products such as PVC. The main emissions from fossil fuel combustion are nitrogen monoxide (NO), which is oxidized when released into the atmosphere, and the produced nitrogen dioxide (NO_2) causes respiratory diseases in the human body.[5]

Table 1.1. The main greenhouse gases.

Gas	Formula	GWP
Carbon dioxide	CO_2	1
Methane	CH_4	21
Nitrous oxide	N_2O	310
Perfluoromethane	CF_4	6500

A Global warming potential for a 100-year time horizon.

As described earlier, NO_x gases, which cause a variety of environmental problems, are doing great harm. In order to solve this problem, it has been agreed to reduce the emission of harmful gases worldwide, and in particular. As shown in Tables 1.2 and 1.3, The environmental regulations (EURO[6,7], LEV[2,6,8,9]) has been enforced and strengthened. So that, vehicle manufacturers, component companies and post-treatment catalyst companies are working on the development of harmful gas emission control and treatment technologies.

Table 1.2. EU Emission standard for gasoline passenger cars.

Stage	Date of Registration	Emission standard of exhaust gases, [g/km]					
		CO	HC	VOCs	NO_x	HC+ NO_x	PM
EURO 1	Jan. 1993	2.72	-	-	-	0.97	-
EURO 2	Jan. 1997	2.2	-	-	-	0.5	-
EURO 3	Jan. 2001	2.30	0.20	-	0.15	-	-
EURO 4	Jan. 2006	1.0	0.10	-	0.08	-	-
EURO 5	Jan. 2011	1.0	0.10	0.068	0.06	-	0.005
EURO 6	Jan. 2015	1.0	0.10	0.068	0.06	-	0.0045

Table 1.3. LEV III Emission standards for passenger cars.

Vehicle Type	Emission Category	NMOG[a] + NO_x [g/mi]	CO [g/mi]	HCHO[b] [mg/mi]	PM [g/mi]
All PC[c]s LDTs≤ 8,500lbs All MDPV[d]s	LEV[e]160	0.160	4.2	4	0.01
	ULEV[f]125	0.125	2.1	4	0.01
	ULEV70	0.070	1.7	4	0.01
	ULEV50	0.050	1.7	4	0.01
	SULEV[g]30	0.030	1.0	4	0.01
	SULEV20	0.020	1.0	4	0.01

[a] NMOG: Non-Methane Organic Gases
[b] HCHO: Formaldehyde
[c] PC: Passenger Cars
[d] MDPV: Medium Duty Passenger Vehicle
[e] LEV: Low Emission vehicle
[f] ULEV: Ultra Low Emission Vehicle
[g] SULEV: Super Ultra Low Emission Vehicle
Durability 150,000 miles

1.2 Three-way catalytic reactions for deNO_x system

Catalysts in the post-treatment field can be classified into diesel oxidation catalysts (DOC),[10] selective reduction catalysts (SCR),[3,11] and three-way catalysts (TWC)[12] in which redox reactions occur simultaneously, depending on the fuel and the removal method of the exhaust.

Since 1970, three-way catalysts simultaneously purify HC, CO, and NO_x, and are essential for gasoline vehicles. Three-way catalyst applied to the gasoline engine is composed of platinum group metals (Pt, Rh, and Pd) as the main active site, and is dispersed on an oxide support (SiO_2, Al_2O_3, CeO_2) having excellent thermal and mechanical stability.[11] Generally, Pt and Pd oxidize CO and unburned HC into CO_2 and H_2O, and Rh reduces NO_x into N_2 that is harmless to the human body.[13] However, Non-CO_2 greenhouse gas, N_2O, is also generated when the catalyst temperature is lower than 300°C,[14] and there is a chronic problem in that NO_x reduction was deactivated in lean conditions containing a large amount of oxygen.[12]

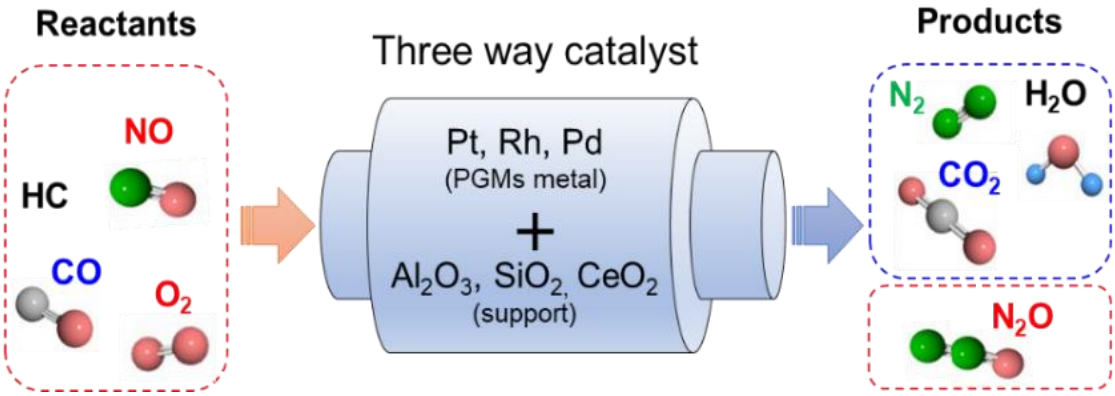

Scheme 1.1. Three-way catalyst reaction.

Platinum group metals used in various catalytic reactions have high catalytic activity and excellent durability.[15] However, metal supply is very limited compared to demand, and their prices are fluctuating and very unstable.[16] Therefore, there is a need for research on catalyst development with excellent activity while reducing or replacing PGMs in future catalyst development.

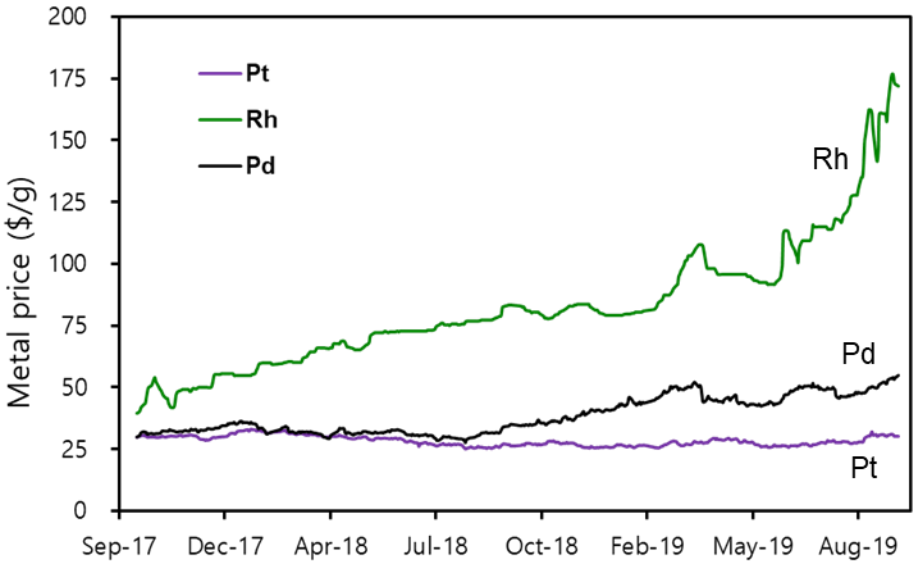

Figure 1.1. Price trends of Platinum group metals in the past three years.

1.3 Alloy in catalytic reaction

Catalytic reactions by metallic materials are the main method used for various chemical transformations in industrial chemistry. In order to improve the performance of metallic catalysts, other metal elements have been frequently added to catalysts as modifiers. The development of such bimetallic materials remains an interesting field of research in catalytic chemistry.[17]

Alloys are classified into two categories depending on their structure: solid-solution alloys and intermetallic compounds. Substitutional solid-solution alloys consist of metals having similar atomic sizes and electronic characters with a crystal structure identical to that of the parent metals with random atomic arrangements (Figure 1.2a). when the atoms of one element are sufficiently small to fit within the lattice void of the counterpart element, interstitial solid-solution alloys can be formed (Figure 1.2b). On the other hand, intermetallic compounds involve the opposite situation to Figure 1.2a, where the component metals have significantly different characters and comprise distinct crystal structures with highly ordered atomic arrangements (Figure 1.2c).

After mixing of the metals, the electronic and geometric states are drastically changed by the formation of alloy or intermetallic phases.[18] Therefore, Alloying is one of the promising approaches to modify the performances of metallic catalysts.

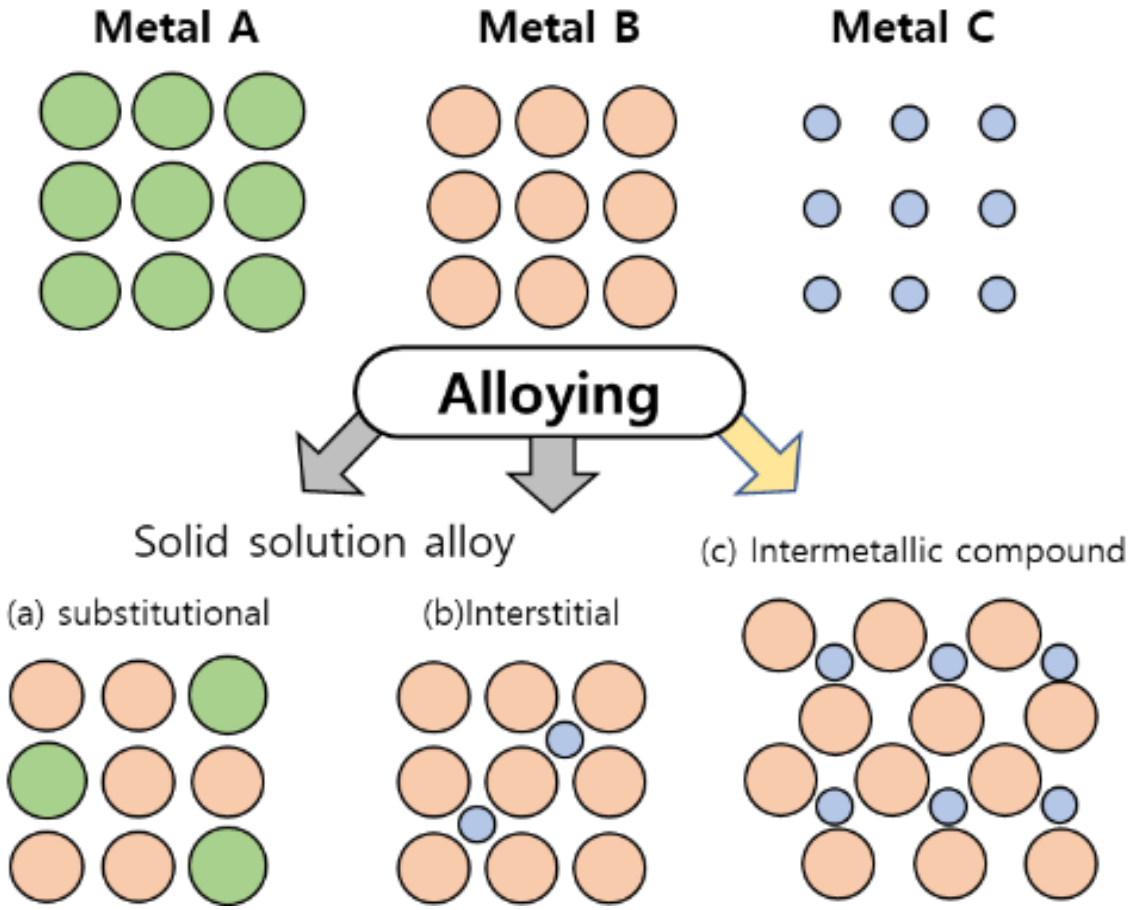

Figure 1.2. Structure of bimetallic alloys.

1.4 Aim of this thesis

In my thesis, I focused on Pd-based alloy materials to design for more effective catalysts that solve the chronic problems (low activity and selectivity in the low-temperature region) of three-way catalysts:

1. Development of highly active and selective NO reduction catalyst by improving the redox properties
    - ✓ Design of Pd-based pseudo-binary alloy catalyst
    - ✓ Design of Cu-Pd single-atom alloy catalyst
2. Development of highly efficient deNO_x system under excessive lean conditions
    - ✓ Design of Pd-Pt based pseudo-binary alloy catalyst
    - ✓ Lean-rich test of prepared catalysts

1.4.1 Development of Pd-based pseudo-binary alloy catalysts for framework 1.

Attention has been increasingly focused on the use of Pd because of its prominent oxidation activity for hydrocarbons and CO,[19] cheaper than Rh, and its superior thermal stability.[20] However, controlling the selectivity of NO reduction to N_2 remains a significant challenge because a significant amount of undesired by-products, such as N_2O, which is a powerful greenhouse effect gas, are particularly generated when CO is used as a reductant under low temperature.[14]

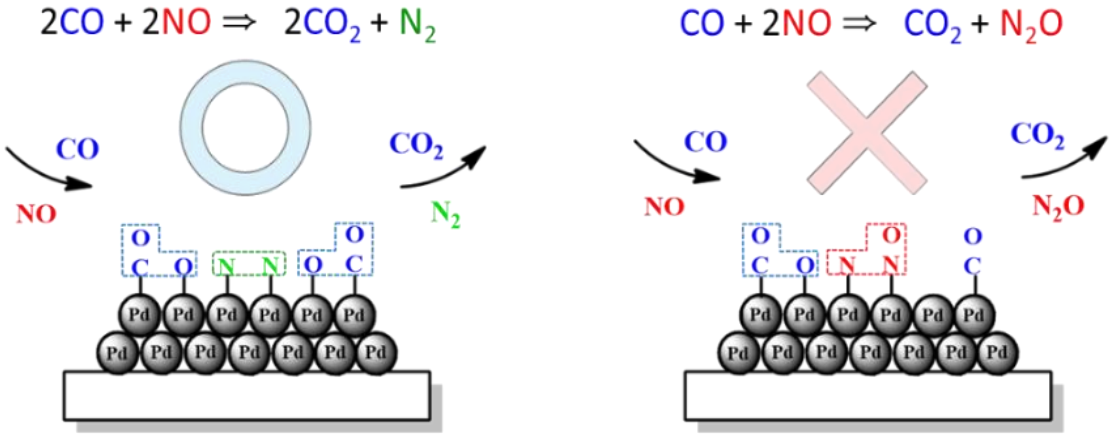

Scheme 1.2. Mechanism of N_2 and N_2O formation in NO reduction by CO over Pd metal

In the previous report of Pd catalyst, Gandhi and co-workers reported that the addition of WO_3 to Pd enhanced N_2 selectivity.[21] Muraki et al. observed that the performance of the Pd catalyst could be enhanced by the addition of lanthanum oxide.[22] However, to the best of our knowledge, no Pd based catalyst that shows high NO reduction ability without N_2O emission even at low temperatures (< 250°C) has been reported in the literature.

Therefore, after alloying of Pd with some other metals to obtain excellent thermal stability, the change in low-temperature activity and selectivity was Investigated, and it was performed to have an alloy design for rational use of Pd metal.

1.4.2 Development of Cu-Pd single-atom alloy catalyst for framework 1

As mentioned in Figure 1.1, platinum group metal (PGM) are rare and expensive. So, one of the possibilities to reduce PGM use is to develop bimetallic catalysts with a minimum amount of PGM alloyed by excess non-precious metals. In particular,

three-way catalysts have developed since the 1990s using transition metals (Cu,[5,23–25] Ni,[17,26–28], Fe,[29] Co,[30] Cr,[31] Mg[32] and Mn[33]) that are inexpensive and rich in reserves. In the previous report, Cu showed high catalytic activity similar to precious metals.[32] Ni is on the traditional borderline in the periodic table between purely molecular and purely dissociative adsorption of NO.[17,34] One previous study reported that NO molecules dissociate above 300 K on Ni(111) at low coverage.[35] Therefore, in line with the next-generation research and development trend, developing catalysts that are economical, highly activity and selective with minimum use of precious metals.

1.4.3 Design of highly active and selective catalyst under lean conditions for framework 2

In the past, gasoline automobiles had used oxidation catalysts for purifying CO and HC by oxidation, while nowadays, three-way catalysts for simultaneous purification of NO_x are used.[13] Figure 1.3 shows the conversion efficiency of the three-way catalysts. Here, lambda (λ) represents the relative air-to-fuel (A/F) ratio.[9,11–13] In fuel lean (excess O_2) conditions, although the purification rates of CO and HC are typically higher than 90%, that of NO_x decreases drastically. In fuel rich conditions, on the other hand, this trend inverts. Therefore, to reduce these three components simultaneously, the A/F ratio supplied to an engine should be stoichiometric.[19,21,22,36] In practical vehicle operation, the A/F ratio is controlled by using an electronic control unit (ECU, Scheme 1.3) so that λ comes into the window for efficient catalytic conversion.[9] However, it is not always the case depending on the operation condition. Therefore, there is a strong need to design a new catalyst that can work well even under lean conditions for efficient deNO_x.

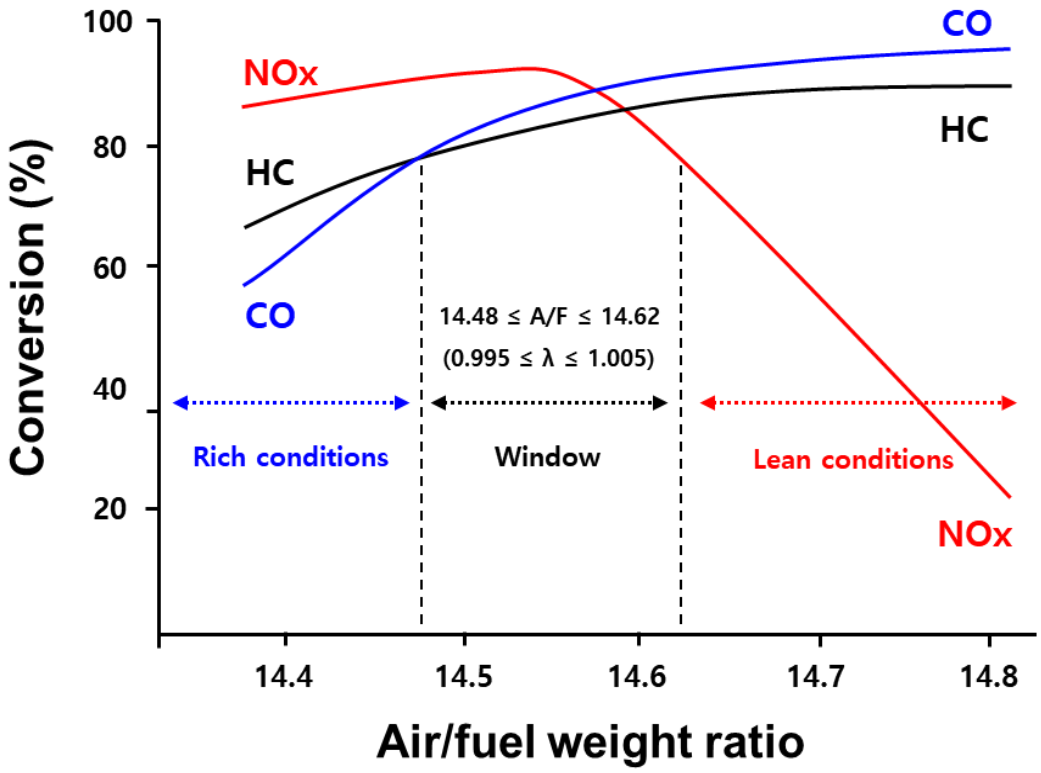

Figure 1.3. The typical performance of three-way catalysts as a function of air/fuel (A/F) ratio.

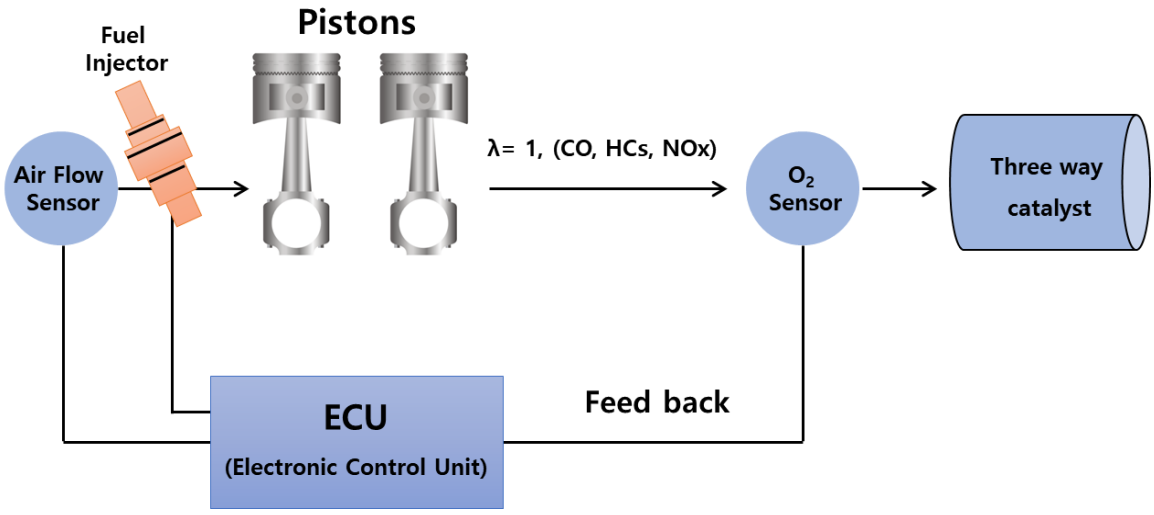

Scheme 1.3. Specific diagram for an exhaust system of a gasoline engine.

1.5 Outline of thesis

This thesis effort on the purification of NO_x gas by using three Pd-based alloy catalysts. 1) Pd-based pseudo-binary alloy catalyst, 2) Cu-Pd single atom alloy, and 3) Pd-Pt based pseudo-binary alloy catalyst. Three different types of alloy systems are developed for efficient reduction of NO_x.

Chapter 2 presents the development of a Pd-based pseudo-binary alloy catalyst for selective reduction of NO without emission of N_2O at low temperatures, which has been unprecedented previously by conventional Pd based catalysts. First, I screened various Pd based bi-metallic catalysts for NO–CO reaction. The results showed that a Pd-Cu alloy catalyst, $PdCu/Al_2O_3$, gave high NO conversion at the low-temperature region and Pd-In intermetallic catalysts, $PdIn/Al_2O_3$, gave high N_2 selectivity below 250°C. $PdIn/Al_2O_3$ catalyst displayed excellent N_2 selectivity even at low temperatures (100% at 200°C). The catalytic activity of PdIn was further improved by substituting a part of In with Cu, where a $Pd(In_{1-x}Cu_x)$ pseudo-binary alloy structure was formed. The optimized catalyst, $Pd(In_{0.33}Cu_{0.67})/Al_2O_3$, facilitated the complete conversion of NO to N_2 (100% yield) even at 200°C and higher, which has never been achieved using metallic catalysts. The formation of the pseudo-binary alloy structure was confirmed by the combination of HAADF-STEM-EDS, EXAFS, and CO-FT-IR analyses. A detailed mechanistic study based on kinetic analysis, operando XAFS, and DFT calculations revealed the roles of In and Cu in the significant enhancement of catalytic performance.

Chapter 3 presents the Cu–Pd single atom alloy catalyst for the reduction of NO, which minimizes the use of precious metal. A series of Cu–Pd alloy nanoparticles supported on Al_2O_3 were prepared by a deposition-precipitation method using urea and tested as catalysts for deNO_x reactions. XRD, HAADF-STEM, XAFS, and FT-IR analyses revealed that single-atom alloy structure was formed when the Cu/Pd ratio was 5, where Pd atoms were well isolated by Cu atoms. Compared with Pd/Al_2O_3,Cu_5Pd/Al_2O_3 exhibited outstanding catalytic activity and N_2 selectivity in NO reduction by CO: the complete conversion of NO to N_2 was achieved even at 175°C for the first time, with long-term stability for at least 30 h. High catalytic performance was also obtained in the presence of O_2 and C_3H_6 (model exhaust gas), where a 90% decrease in Pd use was achieved with minimum evolution of N_2O. Kinetic and DFT

studies demonstrated that N–O bond breaking of the $(NO)_2$ dimer was the rate-determining step and was kinetically promoted by the isolated Pd.

Chapter 4 shows Pd-Pt based pseudo-binary alloy catalyst efficient for deNO_x reaction under excess O_2 lean conditions, which has never been achieved by three-way catalysts. The catalytic performance of PdIn catalyst was further improved by substituting a part of Pd with Pt, where a $(Pd_xPt_{1-x})In$ pseudo-binary alloy structure was formed. The optimized catalyst, namely, $(Pd_{0.5}Pt_{0.5})In/CeO_2$, improved the N_2 yield (>80%) even in the presence of excess oxygen (λ~1.50), where the operating λ window was significantly expanded toward the lean side. The long-term stability and lean-rich cycle tests were performed to evaluate the catalytic performance. The formation of the pseudo-binary alloy structure was confirmed by the combination of HAADF-STEM-EDS and CO-FT-IR analyses.

Chapter 5 shows the general conclusion of the thesis. Chapter 2 concludes that a Pd based pseudo-binary alloy catalysts, $Pd(In_{1-x}Cu_x)/Al_2O_3$, three improved points of redox properties: (1) N_2O adsorption and decomposition ($N_2O \rightarrow N_2 + O$) were drastically enhanced by In, thus resulting in high N_2 selectivity; (2) CO oxidation was promoted by In, thus leading to enhanced low-temperature activity; and (3) Cu substitution improved NO adsorption and dissociation ($NO \rightarrow N + O$). Chapter 3 concludes that N–O bond breaking of the $(NO)_2$ dimer was the rate-determining step and was kinetically promoted by the isolated Pd. Chapter 4 concludes that a PdPt based alloy, $(Pd_{0.5}Pt_{0.5})In$, effectively react the NO reduction by CO in excess O_2 lean condition. Substituted Pt of this alloy structure provided an expanded operating window of the three-way catalytic system. And, the combination of the positive effect of Pt and PdIn enabled the development of a highly active and selective NO reduction by CO at various O_2 concentration and temperatures.

1.6 Concluding remarks

I have developed Pd-based alloy catalysts for NO reduction, which are effective even in the low-temperature region. The catalyst design developed in this study provides highly sophisticated surface structures consisted of two or more metals, which were highly active and selective for the reduction of NO_x. The present study provides a

novel concept of flexible metallic catalyst design based on the pseudo-binary alloy structure.

References

1. B. K. Bose, L. Fellow and C. Science, *IEEE Ind. Electron. Mag.*, 2010, **1**, 6–17.
2. S. L. Winkler, J. E. Anderson, L. Garza, W. C. Ruona, R. Vogt and T. J. Wallington, *npj Clim. Atmos. Sci.*, , DOI:10.1038/s41612-018-0037-5.
3. P. Forzatti, *Appl. Catal. A Gen.*, 2001, **222**, 221–236.
4. J. Pérez-Ramírez, *Appl. Catal. B Environ.*, 2007, **70**, 31–35.
5. T. Franken and R. Palkovits, *Appl. Catal. B Environ.*, 2015, **176**–**177**, 298–305.
6. N. Hooftman, M. Messagie, J. Van Mierlo and T. Coosemans, *Renew. Sustain. Energy Rev.*, 2018, **86**, 1–21.
7. R. O'Driscoll, M. E. J. Stettler, N. Molden, T. Oxley and H. M. ApSimon, *Sci. Total Environ.*, 2018, **621**, 282–290.
8. K. Vijayaraghavan, C. Lindhjem, A. DenBleyker, U. Nopmongcol, J. Grant, E. Tai and G. Yarwood, *Atmos. Environ.*, 2012, **60**, 109–120.
9. R. J. Farrauto, M. Deeba and S. Alerasool, *Nat. Catal.*, 2019, **2**, 603–613.
10. L. Ma, C. Y. Seo, X. Chen, K. Sun and J. W. Schwank, *Appl. Catal. B Environ.*, 2018, **222**, 44–58.
11. T. Maunula, K. Kallinen, N. Kinnunen, M. Keenan and T. Wolff, *Top. Catal.*, 2019, **62**, 315–323.
12. S. A. Malamis, M. Li, W. S. Epling and M. P. Harold, *Appl. Catal. B Environ.*, 2018, **237**, 588–602.
13. T. Kobayashi, T. Yamada and K. Kayano, *Appl. Catal. B Environ.*, 2001, **30**, 287–292.
14. J. H. Holles, M. A. Switzer and R. J. Davis, *J. Catal.*, 2000, **190**, 247–260.
15. U. Bardi and S. Caporali, *Minerals*, 2014, **4**, 388–398.
16. H. Hao, Y. Geng, J. E. Tate, H. Hao, Y. Geng, J. E. Tate, F. Liu, X. Sun, Z. Mu, D. Xun and Z. Liu, *One Earth*, 2019, **1**, 117–125.
17. A. Beniya, Y. Ikuta, N. Isomura, H. Hirata and Y. Watanabe, *ACS Catal.*, 2017, **7**, 1369–1377.
18. S. Furukawa and T. Komatsu, *ACS Catal.*, 2017, **7**, 735–765.
19. Z. Hu, C. Z. Wan, Y. K. Lui, J. Dettling and J. J. Steger, *Catal. Today*, 1996, **30**, 83–89.
20. R. J. Farrauto, J. K. Lampert, M. C. Hobson and E. M. Waterman, *Appl. Catal. B, Environ.*, 1995, **6**, 263–270.
21. K. M. Adams and H. S. Gandhi, *Ind. Eng. Chem. Prod. Res. Dev.*, 1983, **22**, 207–212.

22. H. S. Gandhi, G. W. Graham and R. W. McCabe, *J. Catal.*, 2003, **216**, 433–442.
23. Y. Okamoto, H. Gotoh, H. Aritani, T. Tanaka and S. Yoshida, *J. Chem. Soc. - Faraday Trans.*, 1997, **93**, 3879–3885.
24. Y. Okamoto and H. Gotoh, *Catal. Today*, 1997, **36**, 71–79.
25. F. Amano, S. Suzuki, T. Yamamoto and T. Tanaka, *Appl. Catal. B Environ.*, 2006, **64**, 282–289.
26. T. Tanabe, T. Imai, T. Tokunaga, S. Arai, Y. Yamamoto, S. Ueda, G. V. Ramesh, S. Nagao, H. Hirata, S. I. Matsumoto, T. Fujita and H. Abe, *Chem. Sci.*, 2017, **8**, 3374–3378.
27. H. Asakura, T. Onuki, S. Hosokawa, N. Takagi, S. Sakaki, K. Teramura and T. Tanaka, *Phys. Chem. Chem. Phys.*, 2019, **21**, 18816–18822.
28. D. Lopes, F. Zotin and L. A. Palacio, *Appl. Catal. B Environ.*, 2018, **237**, 327–338.
29. Y. Okamoto, T. Kubota, Y. Ohto and S. Nasu, *J. Catal.*, 2000, **192**, 412–422.
30. L. Zhang, X. Yao, Y. Lu, C. Sun, C. Tang, F. Gao and L. Dong, *J. Colloid Interface Sci.*, 2018, **509**, 334–345.
31. H. Yoshida, Y. Okabe, N. Yamashita, S. Hinokuma and M. Machida, *Catal. Today*, 2017, **281**, 590–595.
32. J. Wu, Y. Li, Y. Yang, Q. Zhang, L. Yun, S. Wu, C. Zhou, Z. Jiang and X. Zhao, *J. Mater. Chem. A*, 2019, **7**, 7202–7212.
33. T. Fujita, H. Abe, T. Tanabe, Y. Ito, T. Tokunaga, S. Arai, Y. Yamamoto, A. Hirata and M. Chen, *Adv. Funct. Mater.*, 2016, **26**, 1609–1616.
34. W. A. Brown and D. A. King, *J. Phys. Chem. B*, 2000, **104**, 2578–2595.
35. D. M. M.J. Breitschafter, E. Umbach, *Surf. Sci.*, 1981, **109**, 493–511.
36. H. Murakl, H. Shinjoh, H. Sobukawa, K. Yokota and Y. Fujitanl, *Ind. Eng. Chem. Prod. Res. Dev.*, 1986, **25**, 202–208.

Chapter 2

Design of Pd-Based Pseudo-Binary Alloy Catalysts for Highly Active and Selective NO Reduction

2.1 Introduction

The reaction of nitric oxide (NO) has received an increasing amount of interest among researchers in human health,[1] bioinorganic,[2] industrial,[3] and environmental chemistry applications.[4] Specifically, NO removal has long been studied as an indispensable process for exhaust gas purification.[5] Platinum group metals (PGMs) such as Pt, Rh, and Pd are known as efficient catalysts for NO reduction with CO,[6, 7] H_2,[8] NH_3,[9] and hydrocarbons[10] as reductants. Attention has been increasingly focused on the use of Pd because of its prominent oxidation activity for hydrocarbons and CO,[11] and its excellent thermal stability.[12] However, controlling the selectivity of NO reduction to N_2 remains a significant challenge because a significant amount of undesired by-products, such as N_2O, which is a powerful greenhouse effect gas, are particularly evolved when CO is used as a reductant.[6] To the best of our knowledge, no metallic catalyst that shows high NO reduction ability without N_2O emission even at low temperatures (< 250°C) has been reported in the literature. In this context, a drastic improvement in the nature of metallic catalysts for this reaction is an important object that will address a number of global environmental issues and fundamental chemistry. The mechanism of NO reduction on the surface of PGMs has been extensively studied, and the following is generally accepted[5, 10, 13]: (1) $NO \rightarrow N + O$ (NO dissociation), (2) $N + N \rightarrow N_2$ (N_2 formation), (3) $N + NO \rightarrow N_2O$ (side reaction), (4) $N_2O \rightarrow N_2 + O$ (N_2O decomposition), and (5) $O + R \rightarrow RO$ (oxygen consumption, R = CO or H_2). Hence, the suppression of (3) and/or the promotion of (4) are required to develop a highly selective NO reduction system. Theoretical approaches have also been studied and have predicted that a stepped (211) surface of PGM was capable of suppressing (3).[14, 15] However, it is difficult to realize a high fraction of such a metastable surface. Therefore, the appropriate design and construction of an ideal reaction environment using metallic materials are necessary.

Intermetallic compounds, which are ordered alloys typically composed of certain metal elements that are separated from one another on the periodic table, can be attractive inorganic materials for sophisticated catalyst design.[16] An appropriate combination of two or three metal elements would provide significantly modified electronic and geometric structures of the active sites and a highly ordered reaction

environment for NO reduction.[16] Indeed, a recent theoretical prediction suggested that the Pd–Ti bimetallic surface was capable of NO reduction by CO without emission of N_2O even at room temperature and higher.[17] Although this is an attractive prediction, there remains another task to retain the metallic state of electropositive Ti at the surface, which is oxidized under a ppb-level oxygen atmosphere.[18] Therefore, in view of practical use, it is also important to choose the counterpart elements that have appropriate redox properties.

In this study, I prepared a series of Pd-based intermetallic compound catalysts by using alumina support (PdM/Al_2O_3, M = Cu, Fe, In, Pb, and Zn) and tested them for selective NO reduction with CO as a reductant. The effect of the second metal on improved selectivity was deeply investigated using characterization techniques, kinetic study, and DFT calculation. Furthermore, the selective bimetallic catalyst was further improved by constructing pseudo-binary alloy structures to develop an innovatively efficient catalytic system. I report a highly active and selective NO reduction system that is based on a novel concept of catalyst design and the fundamental aspects governing catalytic performance in such NO reduction systems.

2.2 Experimental section

2.2.1 Catalyst preparation.

Boehmite (γ-AlOOH) was supplied by SASOL chemicals. γ-Al_2O_3 was prepared by the calcination of boehmite at 900°C for 3 h. A series of Pd-based catalysts (PdM/Al_2O_3, M = Cu, In, Zn, Sn, and Pb) were prepared by the co-impregnation method using an excess amount of water (ca. 25 mL of ion-exchanged water/g of support). The γ-Al_2O_3 support was added to a vigorously stirred mixed aqueous solutions of $Pd(NH_3)_2(NO_2)_2$ and a second metal salt ($Cu(NO_3)_2{\cdot}3H_2O$ (Sigma-Aldrich, 99%, $In(NO_3)_3{\cdot}nH_2O$ (Kanto, 99%), $Zn(NO_3)_2{\cdot}6H_2O$ (Kanto, 99%), $SnCl_2$ (Wako, 99.9%), and $Pb(NO_3)_2$ (Wako, 99.5%)), followed by stirring for 2 h. The mixture was dried under reduced pressure at 50°C, followed by reduction under flowing H_2 (30 ml/min) at 400°C for 1 h. The metal loading and the atomic ratio of Pd/M were adjusted to 3 wt % and 1 (M = Cu, In, and Zn) or 3 (M = Pb and Sn), respectively. For trimetallic catalysts, the metal loading of Pd also was adjusted to 3wt% and the atomic ratio of Pd/(M+N) was one. The

as-impregnated catalysts were reduced under flowing H_2 at 400°C (M = Cu, In, and Zn) or 600°C (M = Pb and Sn) for 1 h.

2.2.2 Catalytic reactions.

The catalyst (0.015 g) diluted with quartz sand (1.985 g, Miyazaki Chemical 99.9%) was treated under flowing hydrogen (50 ml min^{-1}) at 400°C for 0.5 h prior to the catalytic reactions. NO reduction by CO was performed in a fixed-bed continuous flow system by feeding NO (0.5%), CO (0.5%), and He (balance) with the total flow rate of 96 ml min^{-1} (GHSV = 240,000 h^{-1}). The corresponding N_2O reduction was also performed in a similar fashion with an N_2O concentration of 0.5%. The gas-phase was analyzed by an online thermal conductivity detection gas chromatography (Shimazu GC-8A, column: SHINWA SHINCARBON ST) located downstream. A kinetic study was performed by changing the concentration of NO or CO between 0.3%~0.6% with that of the counterpart fixed at 0.5%. The reaction temperature was maintained at 150°C so that NO conversion did not exceed 30%, and the reaction rate ($mol \cdot s^{-1} \cdot molPd^{-1}$) was calculated on the basis of NO conversion.

2.2.3 Characterization.

The crystal structure of the prepared catalyst was examined by powder X-ray diffraction (XRD) by a Rigaku MiniFlex II/AP diffractometer with Cu Kα radiation. High angle annular dark field scanning TEM microscopy (HAADF-STEM) was carried out using a JEOL JEM-ARM200 M microscope equipped with an energy dispersive X-ray (EDX) analyzer (EX24221M1G5T). The STEM analysis was performed at an accelerating voltage of 200 kV. To prepare the TEM specimen, all samples were sonicated in ethanol and then dispersed on a Mo grid supported by an ultrathin carbon film.

CO pulse chemisorption was performed using BELCAT II (Microtrac BEL) to estimate the Pd dispersion of the prepared catalysts. Prior to chemisorption, the catalyst

was pretreated under a 5% H_2/Ar flow (40 ml min^{-1}) at 400°C for 0.5 h. After the reduction pretreatment, He was introduced at the same temperature for 10 min to remove the chemisorbed hydrogen, followed by cooling to room temperature. A 10% CO/He pulse was introduced into the reactor, and the supplied CO flow was quantified downstream by a thermal conductivity detector. For example, Pd dispersion for PdIn/Al_2O_3 (Pd: 3 wt%) was estimated as 11.0%.

The Fourier-transformed infrared (FT-IR) spectra of adsorbed CO were obtained with a JASCO FTIR-4200 spectrometer equipped with an MCT detector in transmission mode (resolution 4 cm^{-1}). The samples were prepared as self-supporting wafers (2.0 cm diameter. < 0.5 mm thickness) and were placed inside an IR cell with CaF_2 windows. A custom glass manifold was connected to the cell to control the gas for pretreatment and the amount of CO introduced. The cell was first purged with He, and the sample was reduced under flowing hydrogen (50 ml min^{-1}) at 400°C for 30 min. After reduction, the wafer was cooled to 40°C under He flowing. The wafer was exposed to CO (0.5%) and He (balance) with a total flow rate of 50 ml min^{-1} for 20 min. After the CO exposure, He was flowed for 5 min to remove the gas phase and weakly adsorbed CO, followed by IR spectra measurements.

X-ray absorption fine structure (XAFS) spectra were recorded on the BL14B2 and BL01B1 stations at SPring-8 of the Japan Synchrotron Radiation Research Institute. A Si(311) double-crystal monochromator was used. Energy calibration was performed using a Pd foil. The spectra were recorded at the edges of Pd K, In K, and Cu K in a transmission mode at room temperature. For static measurements, the pelletized sample was pre-reduced by H_2 at 400°C for 0.5 h and then sealed in a plastic pack under N_2 atmosphere together with an ISO A500-HS oxygen absorber (Fe powder). For operando analysis, the pelletized sample (600 mg of 1.0 wt% Pd/Al_2O_3 or PdIn/Al_2O_3: 200 mg 10 ϕ disk × 3) was introduced into a quartz cell equipped with Kapton film windows and

gas lines connecting a high sampling rate TCD GC (490 Micro GC, Agilent Technologies Inc.) downstream for the quantification of CO, N_2, CO_2, and N_2O. The catalyst in the cell was reduced by flowing 10% H_2/He at 400°C for 15 min, followed by cooling to 200°C under He purge. Thereafter, NO+CO, NO, and CO (0.5% for each with He balance for a total of 800 ml min^{-1}; GHSV = 200,000 h^{-1}) were fed into the cell for 20 min for each gas with 10 min intervals of He purge. The catalyst and products in the gas phase were monitored simultaneously by XAFS and GC, respectively. The obtained XAFS spectra were analyzed using Athena and Artemis software ver. 0.9.25 included in the Demeter package.[19] The obtained XANES spectra were fitted by a linear combination of those of the reduced catalysts and metal oxides (PdO or In_2O_3) within the range of −30 to +50 eV toward E_0. Each linear combination fitting was successfully accomplished with an R factor less than 0.01. The Fourier transformation of the k^2-weighted EXAFS from k space to R space was performed over a k range of 3.0–15 $Å^{-1}$. A part of the Fourier-transformed EXAFS in the R range of 1.2–3.0 Å were inversely Fourier transformed, followed by an analysis using a usual curve fitting method in a k range of 3–15 $Å^{-1}$. The back-scattering amplitude or phase shift parameters were simulated with FEFF 6L and used to perform the curve fitting procedure. The amplitude reduction factors (S_0^2) were determined by fitting the spectra of reference samples (Pd black: 0.761, PdO: 0.827, In_2O_3: 1.112, Cu foil: 0.899, CuO: 0.906) and then they were used for fitting of other EXAFS spectra.

2.2.4 Computational Details.

Periodic DFT calculations were performed using the CASTEP code[20] with Vanderbilt-type ultrasoft pseudopotentials[21] and the Perdew−Burke−Ernzerhof exchange−correlation functional based on the generalized gradient approximation.[22] The plane-wave basis set was truncated at a kinetic energy of 360 eV. A Fermi smearing of 0.1 eV was utilized. Dispersion correlations were considered using the

Tkatchenko–Scheffler method with a scaling coefficient of s_R = 0.94 and a damping parameter of d = 20.[23] The reciprocal space was sampled using a k-point mesh with a spacing of typically 0.04 $Å^{-1}$, as generated by the Monkhorst–Pack scheme.[24] Geometry optimizations and transition state (TS) searches were performed on supercell structures using periodic boundary conditions. The surfaces were modeled using metallic slabs with a thickness of six atomic layers with 13 Å of vacuum spacing. The unit cells were (2 × 2) for Pd(111) and PdIn(120), (2 × 3) for Pd(511), (3 × 2) for PdIn(110), and (3 × 3) for Pd(100). I chose PdIn(110) as the most stable and dominant surface as reported in some literatures.[25, 26] PdIn(120) was modeled as the stepped PdIn(110). Pd(511) was reported by Sautet et al.[27] as the most active stepped surface for NO dissociation. Geometry optimizations were performed using the Broyden–Fletcher–Goldfarb–Shanno (BFGS) algorithm.[28] The unit cell size of the bulk material was firstly optimized, followed by modeling the slab structure and surface relaxation with the size of the supercell fixed. The convergence criteria for structure optimization and energy calculation were set to (a) an SCF tolerance of 1.0×10^{-6} eV per atom, (b) an energy tolerance of 1.0×10^{-5} eV per atom, (c) a maximum force tolerance of 0.05 eV $Å^{-1}$, and (d) a maximum displacement tolerance of 1.0×10^{-3} Å.

The adsorption energy was defined as follows: $E_{ad} = E_{A\text{-}S} - (E_S + E_A)$, where $E_{A\text{-}S}$ is the energy of the slab together with the adsorbate, E_A is the total energy of the free adsorbate, and E_S is the total energy of the bare slab. The adsorption energy for an oxygen-preadsorbed slab was calculated using E_{SH}, which is the total energy of the oxygen-adsorbed slab, instead of using E_S.

The TS search was performed using the complete linear synchronous transit/quadratic synchronous transit (LST/QST) method.[29, 30] Linear synchronous transit maximization was performed, followed by energy minimization in the directions conjugating to the reaction pathway. The approximated TS was used to perform QST maximization with conjugate gradient minimization refinements. This cycle was

repeated until a stationary point was found. Convergence criteria for the TS calculations were set to root-mean-square forces on an atom tolerance of 0.10 eV $Å^{-1}$.

2.3. Results and discussions

2.3.1 Bimetallic system

A series of Pd-based intermetallic catalysts were prepared using the co-impregnation method with γ-Al_2O_3 as the support (PdM/Al_2O_3, M = Cu, In, Zn, Sn, and Pb). The crystallite phases of the prepared catalysts were analyzed using XRD (Figure 2.1).

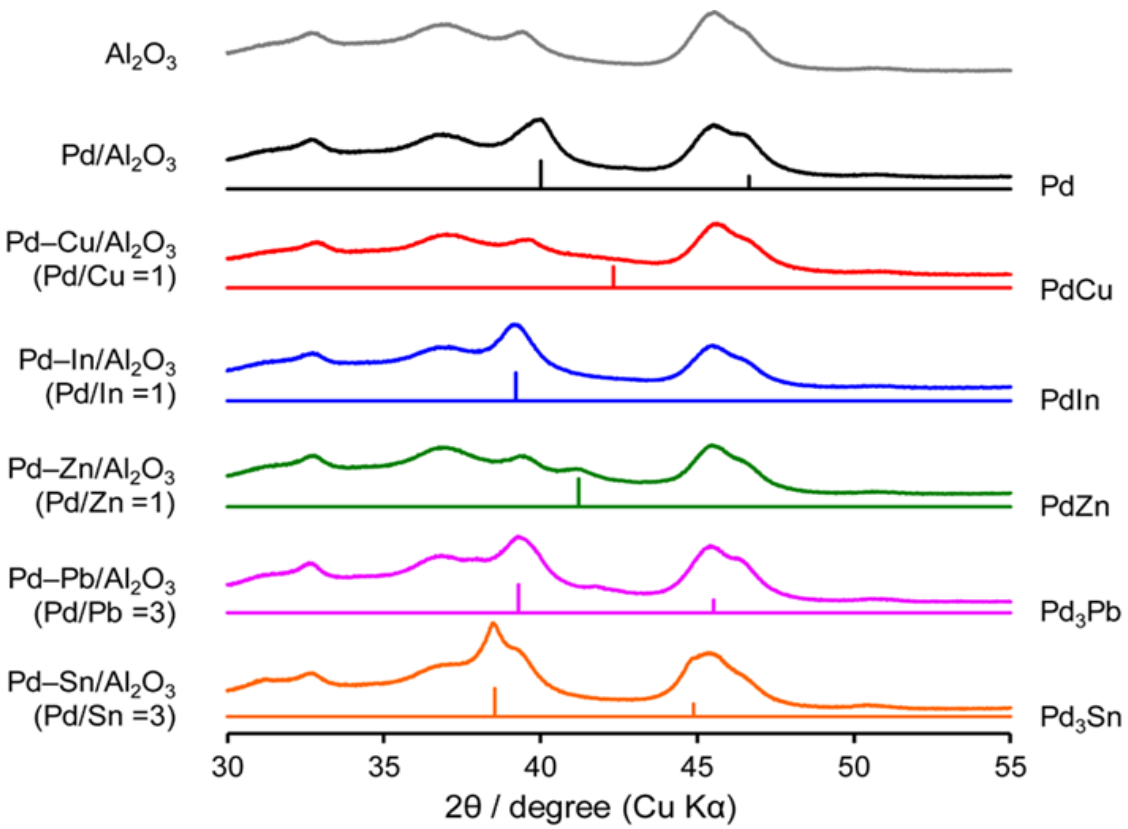

Figure 2.1. XRD patterns of alumina-supported Pd-based bimetallic catalysts. The standard diffraction pattern is shown below each pattern.

For each catalyst, the diffraction peak assigned to the desired intermetallic phase was observed in addition to the peaks from the γ-Al_2O_3 support. Figure 2.2a and Figure 2.2b show the HAADF-STEM image of PdIn/Al_2O_3 and the size distribution of the nanoparticles, respectively.

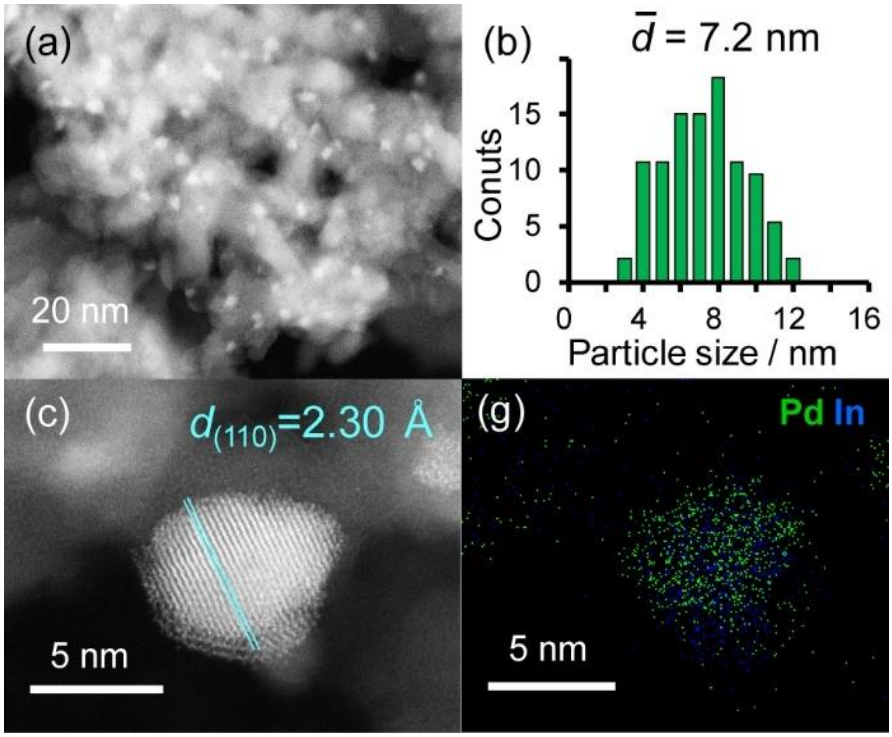

Figure 2.2. (a) HAADE-STEM image of PdIn/Al_2O_3 and (b) size distribution of the nanoparticles. (c) High-resolution STEM image of a single nanoparticle and (d) elemental maps of Pd and In for the nanoparticle acquired using EDX.

Particle sizes ranged from 3 to 12 nm with a volume-weighted average of 7.2 nm, which is consistent with the crystallite size estimated by the Scherrer equation (6.6 nm). Figure 2.2c shows the high-resolution image of a single nanoparticle. Lattice fringes with 2.30 Å spacing were clearly observed, and this finding is consistent finely with the interplanar distance of the PdIn(110) plane (2.30 Å).[31] The elemental maps of Pd and In that were acquired using the EDX analysis of this field revealed that the Pd and In

atoms comprising the nanoparticles were homogeneously dispersed (Figure 2.2d).

I then tested the catalytic performance of Pd-based catalysts (PdM/Al_2O_3; M = Cu, In, Zn, Pb, and Sn, Pd: 3 wt%) in NO reduction by CO. Figure 2.3 shows the temperature dependences of (a) NO conversion and (b) N_2 selectivity obtained using these catalysts.

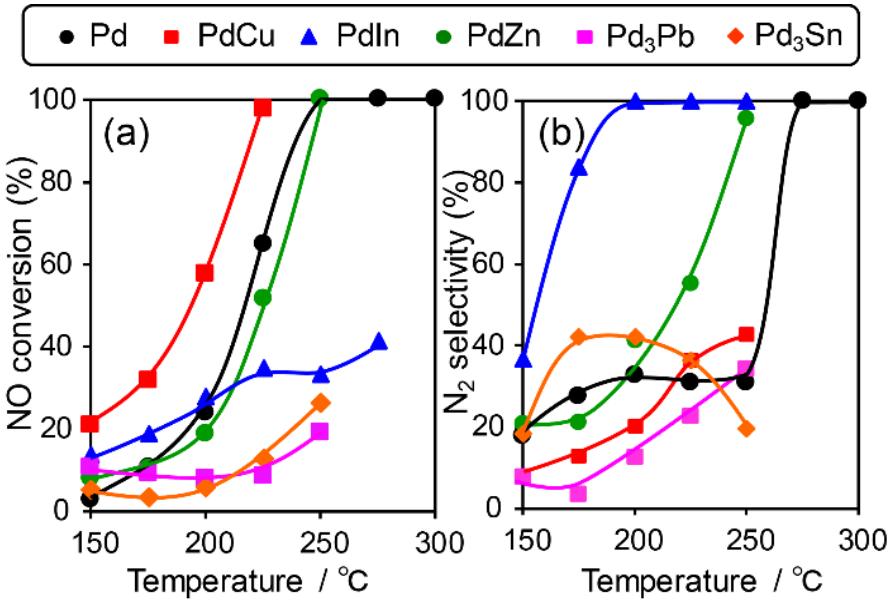

Figure 2.3. (a) NO conversion and (b) N_2 selectivity in NO reduction by CO using Pd based catalysts.

Note that a harsh condition (NO, CO = 5,000 ppm, GHSV = 240,000 h^{-1}) was employed so that the difference in catalytic performances became obvious. Pd/Al_2O_3 showed a light-off temperature of ca. 220°C, and full NO conversion was obtained at 250°C. N_2 selectivity was approximately 30% below 250°C, which was indicative of the significant formation of N_2O (~70%) and the intrinsic low N_2 selectivity of Pd for NO reduction to N_2 at low temperatures. PdCu and PdZn showed similar light-off behavior. For Pd-based bimetallic catalysts, N_2 selectivity monotonically increased up to 100% as the reaction temperature increased. On the contrary, N_2 selectivity in the low-temperature region (250°C) was quite different depending on the second metal

(PdIn >> PdZn > PdCu > Pd > Pd_3Pb). PdIn exhibited very high selectivities over a wide range of temperatures (100% even at 200°C and higher); to the best of our knowledge, this finding has never been reported for this reaction when using metal catalysts. Therefore, the formation of intermetallic phases drastically modified the N_2 selectivity in NO reduction by CO and allowed the highly selective conversion.

However, the catalytic activity of PdIn was not sufficient, particularly in the high-temperature region (Figure 2.3a). For better NO_x removal performance, both N_2 selectivity and NO conversion should also be enhanced. I then focused on improving the catalytic activity of the PdIn catalyst. I first tried to use a series of Pd-rich Pd–In catalysts (Pd/In = 1, 2, 3, and 5.67) to increase the reaction rate. However, NO conversion did not increase and N_2 selectivity was significantly decreased as the Pd/In ratio increased (Figure 2.4). Therefore, a conventional method for changing the Pd/In ratio did not effectively improve catalytic performance. In general, because the structure and electronic state of the intermetallic compound are determined depending on the element and composition ratio, these factors cannot be tuned flexibly and independently. Therefore, an appropriate methodology that finely tunes the nature of intermetallic catalyst must be developed.

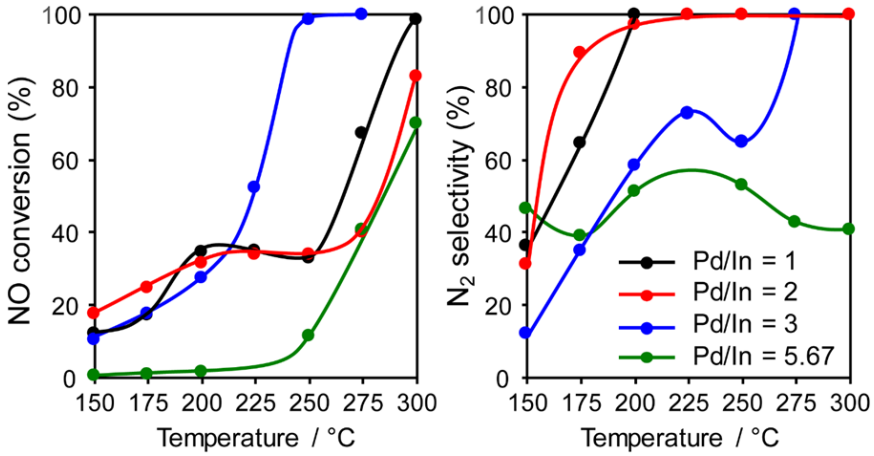

Figure 2.4. (a) NO conversion and N_2 selectivity in NO reduction by CO using Pd–In/Al_2O_3 catalyst with various Pd/In ratios.

2.3.2 Trimetallic system

For the catalyst design of such an ideal concept, I have focused on a pseudo-binary alloy structure[32-34] of Pd($In_{1-x}M_x$) using a third metal element M (Scheme 2.1).

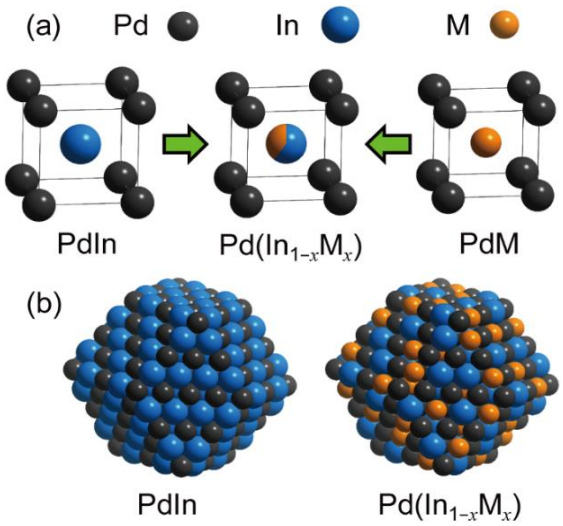

Scheme 2.1. Concept of PdIn-based pseudo-binary alloy having a CsCl-type structure with the substitution of In by M. (b) Models of nanoparticulate PdIn and Pd($In_{1-x}M_x$) with a rhombohedral structure surrounded by {110} surfaces. A part of In is replaced by M without modification of Pd.

This compound retains the CsCl-type structure of intermetallic PdIn with a part of In replaced by M, thus enabling the gradual modification of the In/M ratio and catalytic property. This structure can also be regarded as a solid solution alloy of CsCl-type PdIn and PdM, namely, $(PdIn)_{1-x}(PdM)_x$.[32] Several metal elements such as Ti,[35] Mn[36], Fe,[37] Cu,[38] Zn,[39] and Ga,[40] which form intermetallic phases with bcc structures, are potential candidates for the third metal M. Here, I first chose Cu as the third metal M because PdCu exhibited a high catalytic activity (Figure 2.3a). Several Pd–In–Cu/Al_2O_3 catalysts with various In/Cu ratios were prepared using the co-impregnation method as used for bimetallic materials. Figure 2.5a shows the HAADF-STEM images of a Pd–In–Cu/Al_2O_3 (Pd:In:Cu = 3:1:2) catalyst.

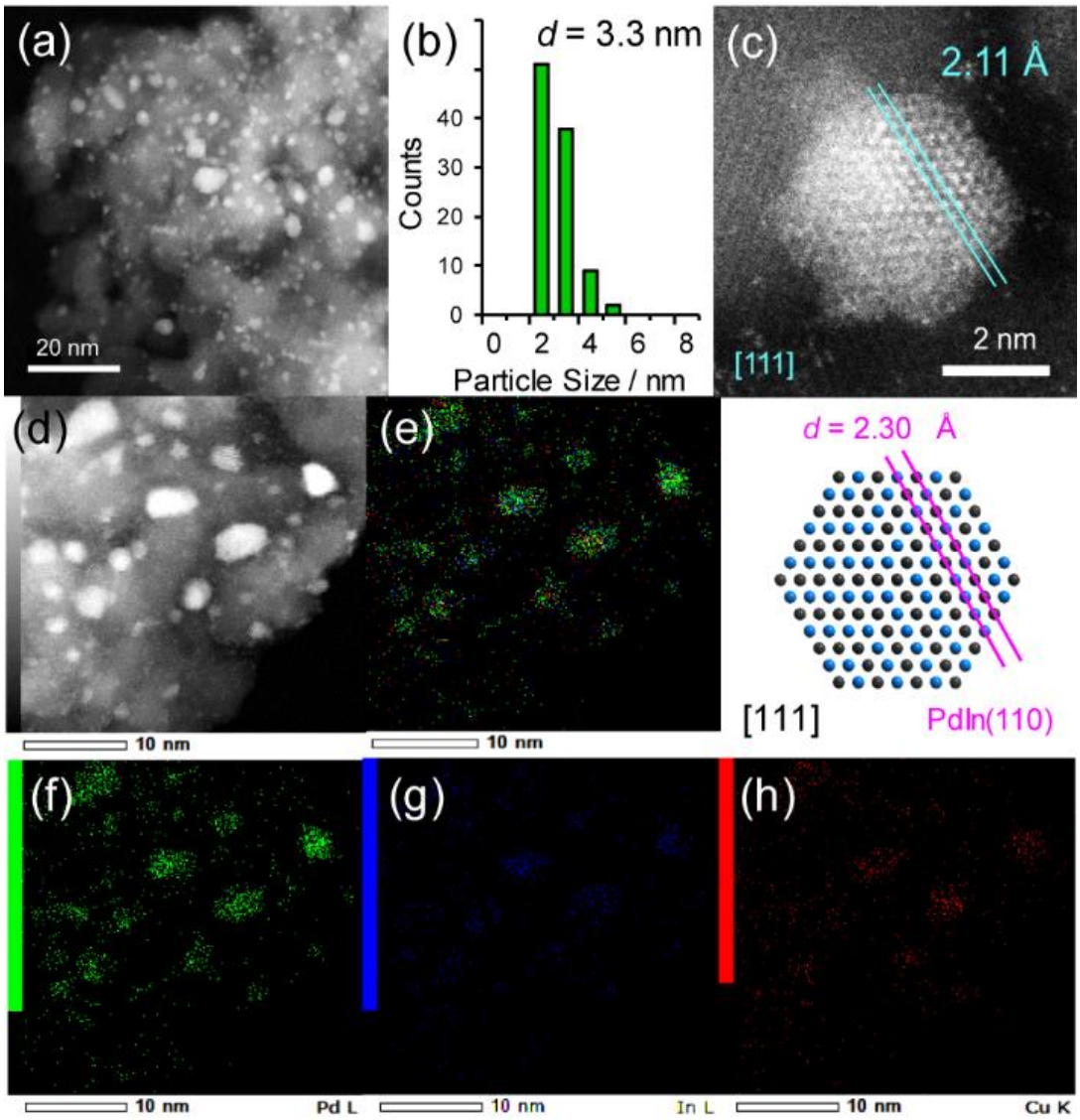

Figure 2.5. (a) HAADF-STEM image of Pd–In–Cu/Al_2O_3 (Pd:In:Cu = 3:1:2) and (b) size distribution of the nanoparticle. (c) High-resolution STEM image of a single nanoparticle (top) and rhombohedral crystal of PdIn viewed along the [111] direction (bottom). (d) HAADF-STEM image of Pd–In–Cu/Al_2O_3 and elemental maps of (e) Pd + In + Cu over-layer, (f) Pd, (g) In, and (h) Cu acquired using EDX.

The size distribution of the nanoparticles was shifted into a smaller region (2~5 nm, Figure 2.5b) than that of PdIn/Al_2O_3. Similar to the observation for the Pd-Cu catalyst (Figure 2.1), the presence of Cu might inhibit the aggregation of the metal nanoparticles during catalyst preparation. The EDX mapping for some nanoparticles showed that Pd,

In, and Cu were homogeneously dispersed and constituted the nanoparticles (Figure 2.5d~h). A high-resolution image of a single nanoparticle displayed the atomic arrangement of a CsCl-type crystal viewed along the [111] direction with 2.11 Å of the interplanar distance of {110} planes (Figure 2.5c). Note that this structure cannot be assigned to any fcc structure because the corresponding atomic arrangement with six-fold symmetry for an fcc crystal appears with significantly shorter interplanar distances (e.g., 1.38 Å for Pd(220)). The observed interplanar distance is close to but slightly shorter than that of PdIn(110), namely 2.30 Å,[31] suggesting the shrinkage of the PdIn crystal lattice by the substitution of In with Cu. By applying Vegard's law on the basis of their atomic radii[41] and ratio (Pd: 1.373 Å, In: 1.660 Å, Cu: 1.276 Å, 3:1:2), it is possible to estimate the theoretical shrinkage of the crystal lattice to be 8.4% (Figure 2.6). This value agrees with the experimental shrinkage observed in Figure 2.5c (8.2%) and supports the formation of a Pd($In_{0.33}Cu_{0.67}$) pseudo-binary alloy structure.

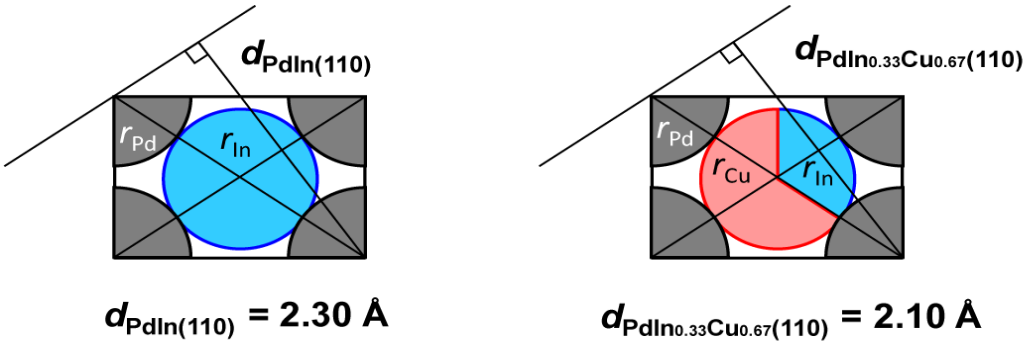

Figure 2.6. Theoretical shrinkage of PdIn lattice applying Vegard's law with each atomic size and ratio (Pd: 1.373 Å, In: 1.660 Å, Cu: 1.276 Å, 3:1:2) at (110) plane.

I also performed EXAFS analysis for PdIn and Pd–In–Cu catalysts to obtain structural information for the entire catalyst. Table 2.1 summarizes the curve fitting results.

Table 2.1. Summary of EXAFS curve fitting for Pd-based catalysts.

sample	edge	shell	*N*	*R*(Å)	Δ*E* (eV)	σ^2(Å^2)	R-factor
Pd black	Pd K	Pd–Pd	12 (fix)	2.74 ± 0.00	0.0 ± 0.3	0.006	0.002
Pd/Al_2O_3	Pd K	Pd–O	0.7 ± 0.2	2.02 ± 0.02	6.4 ± 3.2	0.004	0.002
		Pd–Pd	7.1 ± 0.3	2.73 ± 0.00	0.0 ± 0.4	0.009	
$PdIn/Al_2O_3$	Pd K	Pd–In	6.6 ± 0.3	2.73 ± 0.00	0.0 ± 0.3	0.012	0.012
	In K	In–O	2.5 ± 0.3	2.14 ± 0.01	2.3 ± 1.5	0.010	0.014
		In–Pd	5.7 ± 0.6	2.74 ± 0.01	0.0 ± 0.7	0.014	
$Pd–In–Cu/Al_2O_3$	Pd K	Pd–Cu	3.0 ± 0.3	2.60 ± 0.01	1.8 ± 1.6	0.006	0.002
(Pd:In:Cu = 3:1:2)		Pd–In	5.8 ± 0.5	2.70 ± 0.01	-1.3 ± 0.7	0.013	
	In K	In–O	2.6 ± 0.3	2.13 ± 0.01	4.1 ± 1.5	0.010	0.010
		In–Pd	5.8 ± 0.5	2.70+0.00	0.0 ± 0.6	0.010	
	Cu K	Cu–O	1.0 ± 0.2	1.93 ± 0.02	5.8 ± 2.3	0.006	0.006
		Cu–Cu	2.2 ± 1.6	2.58 ± 0.08	-1.0 ± 9.5	0.013	
		Cu–Pd	3.1 ± 0.9	2.59 ± 0.02	-3.2 ± 0.7	0.009	

For the PdIn catalyst, the Pd–In bond lengths observed from the edges of Pd K and In K agreed with each other within the error bar. For the Pd–In–Cu catalyst, two different scatterings assigned to Pd–Cu and Pd–In were observed in the Pd K-edge EXAFS. The corresponding Cu–Pd and In–Pd shells were also confirmed in the In K- and Cu K-edge EXAFS, respectively, with good agreements in the coordination numbers and bond lengths. Assuming In–Cu scattering in the In K edge instead of and in addition to the In–Pd scattering did not result in good fittings (R > 0.1 and negative *N* for In–Cu, respectively, data not shown). This suggests that (1) In atoms in the alloy phase are surrounded by Pd; hence (2) Pd is not substituted by Cu. These results strongly suggest the formation of a $Pd(In_{1-x}Cu_x)$ pseudo-binary alloy structure. Moreover, the Pd–In interatomic distance of the Pd–In–Cu catalyst (2.70 Å) was slightly shorter than that of PdIn (2.73 Å). This is consistent with the shrinkage of PdIn lattice by the incorporation of Cu (Figure 2.5c) and excludes the possibility that the catalyst is a physical mixture of PdIn and PdCu phases. For Cu K-edge EXAFS, the small contributions of Cu–Cu scattering was also observed in addition to Cu–Pd

scattering. Considering (2), it is likely that there remains a small amount of monometallic Cu that did not participate in the formation of alloy species, which cannot be detected in Pd K and In K edges. The coordination number of the Pd–Cu shell in Pd–In–Cu was smaller than that of the Pd–In shell despite the higher feeding ratio of Cu than In probably because of the presence of monometallic Cu and/or the inhomogeneous distribution of Cu in Pd($In_{1-x}Cu_x$) (e.g., Cu-rich shell and In-rich core). Small contributions of M–O scatterings were also observed for all samples probably because of the interaction between the metal nanoparticles and Al_2O_3 support and/or the aerobic oxidation of the surface region by trace amounts of oxygen impurities.

FT-IR analysis was also performed for the Pd-based catalysts by using CO adsorption to obtain information about the electronic and geometric environment at the surface (Figure 2.7). Pd/Al_2O_3 showed three different features assigned to the stretching vibration of CO adsorbed on top (2,086 cm^{-1}), bridge (~1,950 cm^{-1}), and threefold hollow (~1,860 cm^{-1}) sites of Pd.[42] For PdIn/Al_2O_3, the peak position of linear CO was red-shifted (2,068 cm^{-1}) and the peak corresponding to the bridge CO almost vanished. This indicates that the (1) Pd in PdIn is electron enriched by In, the (2) Pd–Pd ensembles are completely diluted by In, and (3) the catalyst surface is also of intermetallic PdIn. A different trend was observed for PdCu/Al_2O_3, wherein the peak of the on-top CO was blue-shifted (2,099 and 2,118 cm^{-1}) from that of Pd and a part of bridge CO remained. The observed two on-top CO could be assigned to those on Pd (2,099 cm^{-1}) and Cu (2,118 cm^{-1}) sites.

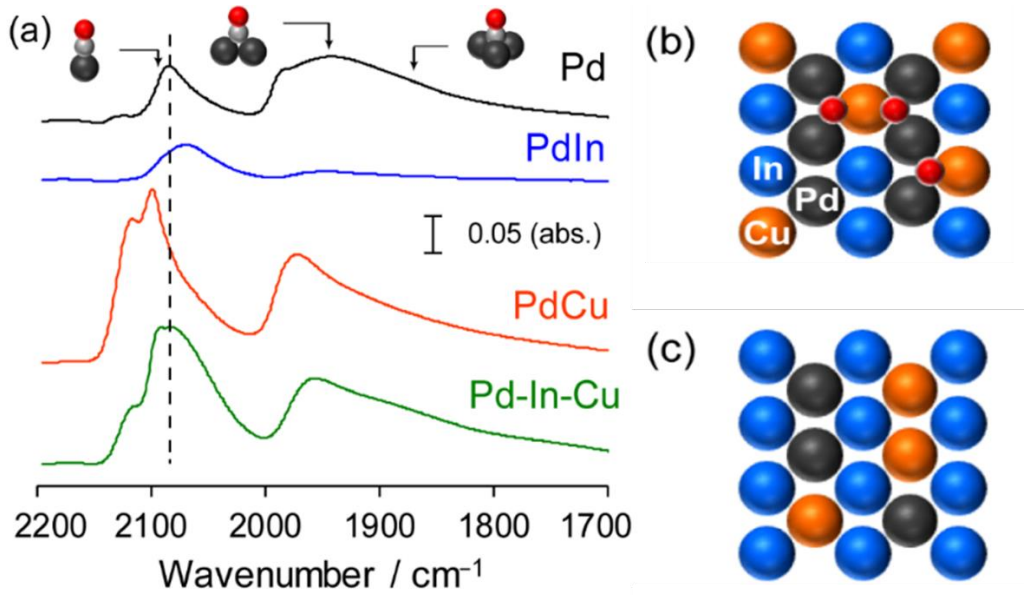

Figure 2.7. (a) FT-IR spectra of CO adsorbed on Pd/Al_2O_3, $PdIn/Al_2O_3$, $PdCu/Al_2O_3$ and $Pd–In–Cu/Al_2O_3$ (Pd:In:Cu = 3:1:2) catalysts. The atomic arrangement of the most stable (110) surface of $Pd(In_{1-x}Cu_x)$ assuming (b) In–Cu and (c) Pd–Cu replacement. Pd_2Cu hollow sites are formed in (b).

Although CO adsorption on metallic Cu is generally accepted to be very weak, our recent report revealed that CO can be adsorbed on the metallic Cu sites of intermetallic PtCu, where linear CO on Pt and Cu appeared at 2,050 and 2,120 cm^{-1}, respectively.[43] Considering that Pd–Pd ensembles are sufficiently diluted by Cu, the appearance of the threefold CO suggests that Pd_2Cu hollows work as adsorption sites of CO. Recent experimental and theoretical works suggested that CO adsorption on the Pd_2Cu hollow site were reasonable.[44, 45] $Pd–In–Cu/Al_2O_3$ showed an intermediate feature between PdIn and PdCu, that is, linear CO of which peak position was close to that of Pd and small amounts of bridge and threefold CO remained. This indicates that the electronic effects of In and Cu on Pd canceled each other out and that Pd, In, and Cu are all present at the surface. on. If Cu is substituted exclusively with Pd, Pd-less ensembles such as PdInCu or Cu_2In hollow sites are only allowed at (110) surface (Figure 2.7c), resulting in no bridge or threefold CO. Thus, the FT-IR study supported the proposition

that the intermetallic and the pseudo-binary alloy structures were also formed at the catalyst surface.

The prepared trimetallic catalysts with various Cu contents (Pd–In–Cu/Al_2O_3, Pd:In:Cu = 1 : 1−*x* : *x*, *x* = 0.33, 0.5, 0.67, and 0.9) were tested in NO reduction by CO to evaluate the effect of Cu substitution. Figure 2.8 shows the temperature dependences of the NO conversion and N_2 selectivity obtained with these catalysts. In most cases, NO conversion was drastically increased without lowering the N_2 selectivity by Cu substitution. The In-rich catalyst (*x* =0.33) showed a temperature-dependence similar to that of PdIn (*x* = 0, without light-off behavior), thus resulting in NO conversions plateauing in the high-temperature region (> 225°C).

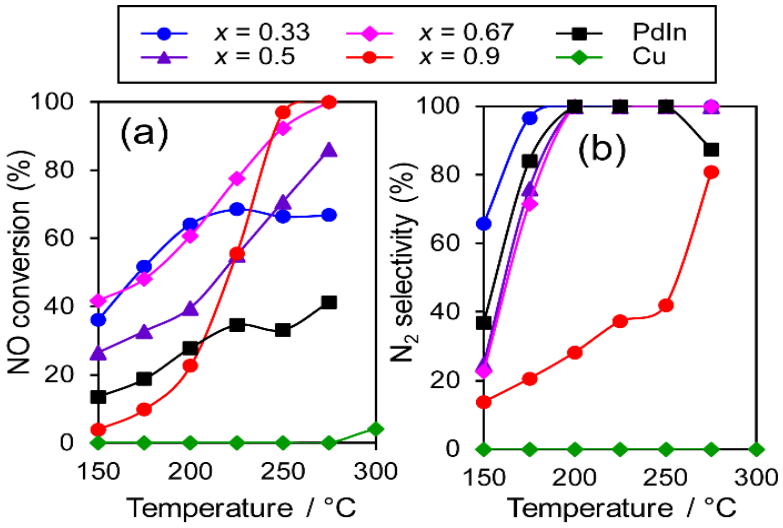

Figure 2.8. Temperature dependences of NO conversion and N_2 selectivity in NO reduction by CO over various Pd–In–Cu/Al_2O_3 (Pd:In:Cu = 1 : 1−*x* : *x*) catalysts.

On the contrary, Cu-dominant catalyst (*x* = 0.9) showed a typical light off behavior and low N_2 selectivity as observed for PdCu. Therefore, the characteristics of the parent bimetallic materials were strongly reflected in the catalysts with biased In/Cu ratios. The best performance was obtained when *x* = 0.67 with a monotonous increase in NO conversion and excellent N_2 selectivity as observed for PdIn. It should be noted that the

$Pd(In_{0.33}Cu_{0.67})/Al_2O_3$ catalyst showed very high catalytic activities at low-temperature regions (e.g., for NO conversion at 150°C, $Pd(In_{0.33}Cu_{0.67})$ 42%, PdIn, 14%, Pd 3%). Thus, the substitution of In with Cu remarkably enhanced the catalytic activity of PdIn without changing N_2 selectivity. A control experiment using Cu/Al_2O_3 (Cu: 1.2 wt%) with Cu content identical to that included in $Pd(In_{0.33}Cu_{0.67})/Al_2O_3$ was also performed because metallic Cu is known to be active for NO reduction by CO.[46] However, in our condition, Cu alone did not work at all below 275°C, suggesting that the catalysis of Cu itself did not contribute to the significant enhancement in catalytic activity. I also tested the performance of $Pd(In_{0.33}Cu_{0.67})/Al_2O_3$ catalyst in various conditions. Figure 2.9 shows the gas-phase distribution (mol-%) of NO, N_2O and N_2 during catalytic NO reduction with CO using $Pd(In_{0.33}Cu_{0.67})/Al_2O_3$ under standard conditions.

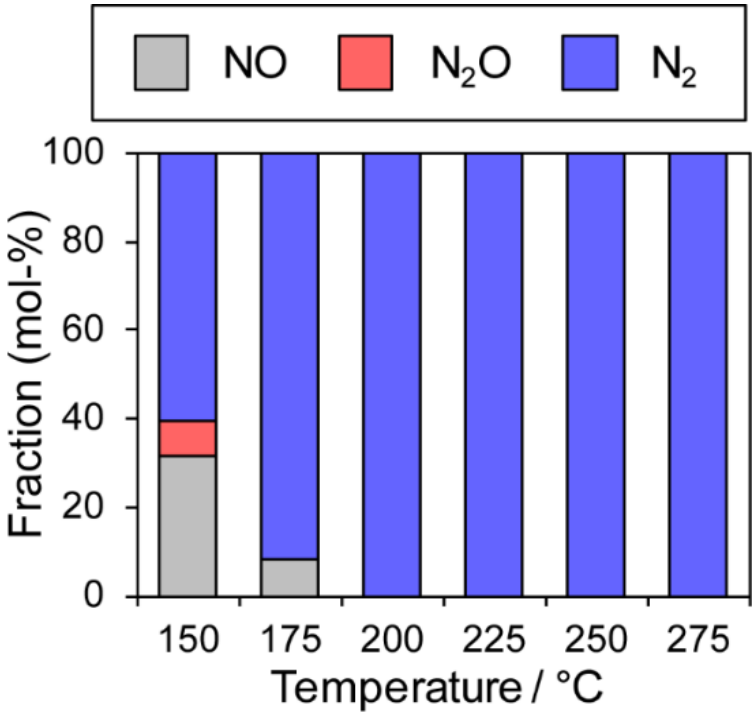

Figure 2.9. The fraction of NO, N_2O and N_2 in effluent gas (mol-%) during catalytic NO reduction with CO using $Pd(In_{0.33}Cu_{0.67})/Al_2O_3$ catalyst (NO and CO: 0.5% balanced with He; catalyst: 0.060 g; total flow: 48 ml min^{-1}).

Emphasis should be placed on the complete conversion of NO into N_2 at 200°C and higher. To the best of our knowledge, this is the first report of complete deNO_x by CO at such a low temperature. N_2O emission was not observed even at 175°C, thus highlighting the remarkably high N_2 selectivity. I also tested the long-term stability of the best catalytic performance at 200°C. Although NO conversion was slightly decreased during the first several hours (100% to 72%), no further deactivation was observed up to 24 h (Figure 2.10). N_2 selectivity was always 100%, showing that no N_2O was emitted during the daylong operation. The catalytic performance was completely recovered (100% N_2 yield, Figure 2.10) after the catalyst was placed in a reductive atmosphere (H_2 flow, 400°C for 0.5 h). Therefore, the initial deactivation occurs probably due to the accumulation of oxygen species on the catalyst surface, reaching a steady-state at the early stage of the reaction.

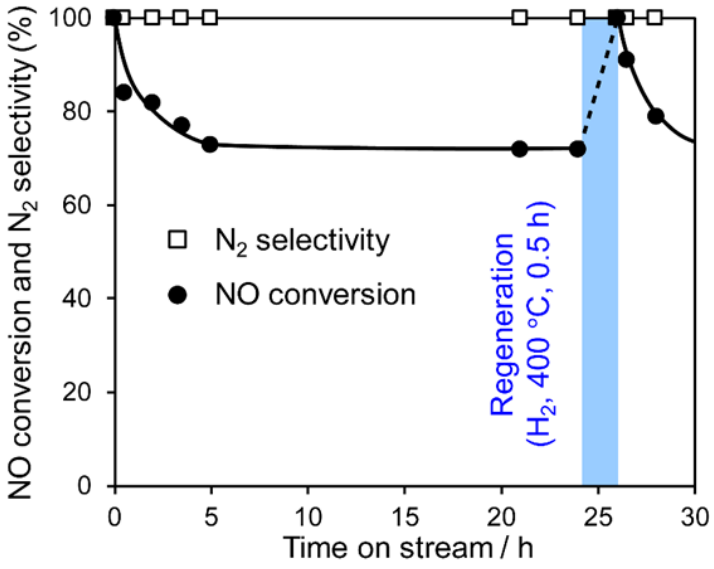

Figure 2.10. Change in NO conversion and N_2 selectivity during a long time NO−CO reaction over $Pd(In_{0.33}Cu_{0.67})/Al_2O_3$ (NO and CO: 0.5% balanced with He; catalyst: 0.060 g; total flow: 48 ml min^{-1}).

Besides, the $Pd(In_{0.33}Cu_{0.67})/Al_2O_3$ catalyst exhibited excellent N_2 selectivities (75~100%) even under a wide range of nonstoichiometric conditions (NO/CO ratio: 0.4~2.5; see Figure 2.11 for details).

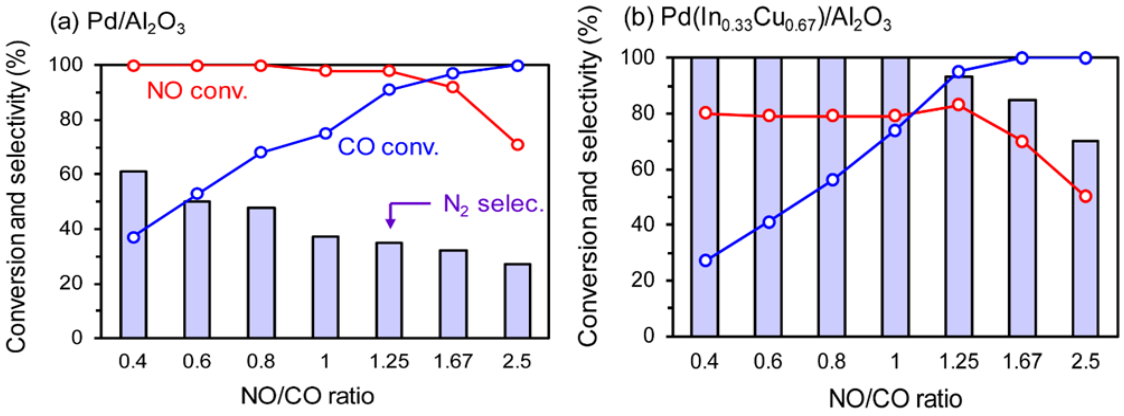

Figure 2.11. Catalytic performances of (a) Pd/Al_2O_3 and (b) $Pd(In_{0.33}Cu_{0.67})/Al_2O_3$ catalysts in NO reduction by CO with various NO/CO ratio.

Note that high N_2 selectivity was maintained under NO-rich (lean) conditions. The corresponding Pd/Al_2O_3 catalyst showed low N_2 selectivities (27~61%) in these conditions, reflecting the difficulty of selective NO reduction using monometallic Pd catalysts. Thus, I developed a highly active and selective deNO_x catalyst using a $Pd(In_{0.33}Cu_{0.67})$ pseudo-binary alloy. CO adsorption experiment confirmed that $Pd(In_{0.33}Cu_{0.67})$ had a higher Pd dispersion than PdIn (19 and 11%, respectively), as expected from the smaller particle size. This may be one of the reasons for the increased catalytic activity for $Pd(In_{0.33}Cu_{0.67})$. However, the great enhancement in NO conversion in the high-temperature region cannot be explained only by the improvement in metal dispersion. This point will be discussed later in greater detail. I also tested other trimetallic catalysts using various third metals ($Pd(In_{1-x}M_x)/Al_2O_3$, M = Fe, Co, Ni, and Ga). However, no catalytic performance superior to that of $Pd(In_{0.33}Cu_{0.67})$ was obtained (Figure 2.12).

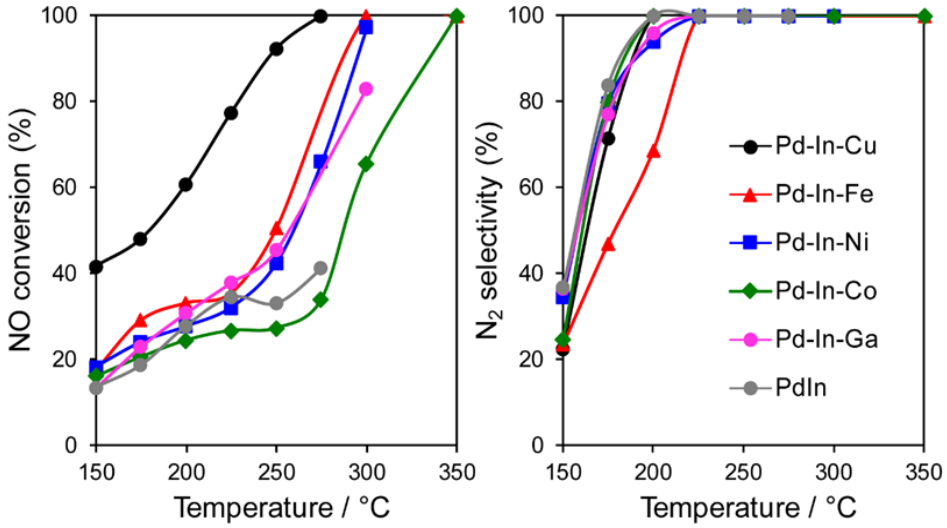

Figure 2.12. Catalytic performance of $Pd(In_{0.33}M_{0.67})/Al_2O_3$ catalysts in NO reduction by CO.

2.3.3 Mechanistic study

I then investigated the role of In and Cu in the great enhancement in N_2 selectivity and NO conversion, respectively. As mentioned in the introduction paragraph, N_2 selectivity should be improved by inhibiting N_2O formation and/or accelerating N_2O decomposition. The latter can be easily evaluated using N_2O as a reactant molecule. Therefore, I tested the catalytic activity of the Pd-based catalysts in N_2O reduction to N_2 with and without CO (Figure 2.13).

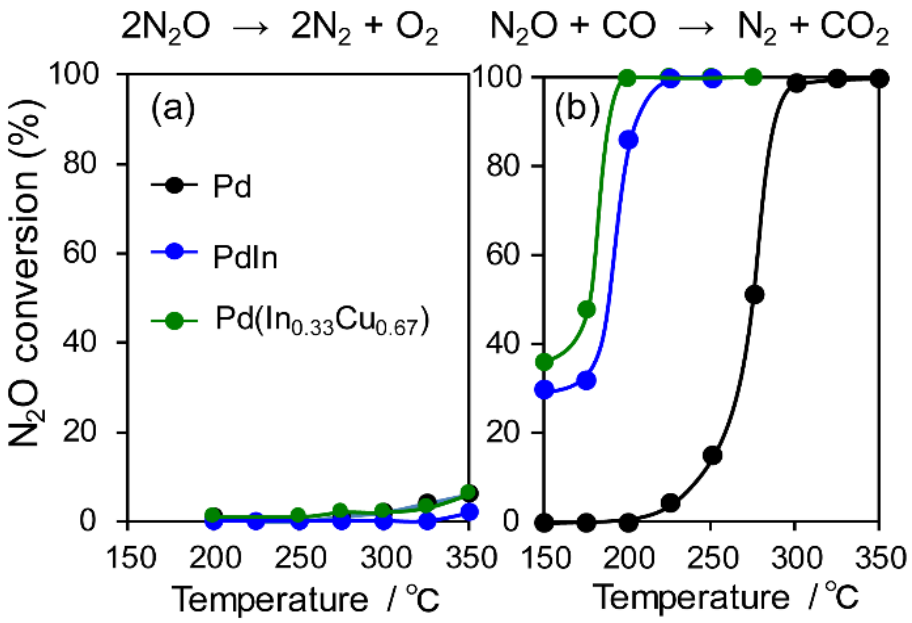

Figure 2.13. N_2O (a) decomposition and (b) reduction by CO using Pd, PdIn, and $Pd(In_{0.33}Cu_{0.67})$ catalysts.

The results show that N_2O conversion was very low (< 5%) even at 350°C in the absence of CO, whereas high N_2 selectivity was obtained in NO reduction by CO. It has been known that N_2O itself is easily decomposed to N_2 and O on the clean surface of transition metals even at very low temperatures.[47] However, a reaction no longer occurs after the saturation coverage of O on the surface. Therefore, this result indicates that (1) the catalyst surface is immediately covered with a small amount of O and (2) the formed surface oxide layers are hardly reduced without any reductant. On the contrary, the N_2O conversion trend was completely changed in the presence of CO. For Pd/Al_2O_3, N_2O conversion was drastically increased as temperature increased with a light-off temperature of 275°C. $PdIn/Al_2O_3$ showed a similar trend but with a lower light-off temperature (175°C). The light-off temperatures of N_2O conversion were in good agreement with those of N_2 selectivity in NO reduction by CO (Figure 2.13b and 2.3b). These results strongly indicate that the remarkably enhanced N_2O reduction ability contributes to the excellent N_2 selectivity in NO reduction by CO.

I then evaluated the apparent activation energies of N_2O reduction by CO from

Arrhenius-type plots (Figure 2.14, Table 2.2 summarizes the results). Pd/Al_2O_3 and $PdIn/Al_2O_3$ showed the activation energies of 113.4 and 28.9 kJ mol^{-1}, respectively, indicating that the activation barrier was remarkably decreased by the formation of intermetallic PdIn phase. A similar trend and E_A values were also observed in NO reduction by CO (86.5 and 23.1 kJ mol^{-1} for Pd/Al_2O_3 and $PdIn/Al_2O_3$, respectively). This implies that a common elementary step (e.g., CO oxidation by surface O) limits the overall reaction rates in both N_2O and NO reduction and is remarkably enhanced by PdIn. I also obtained the E_a from the Arrhenius plot based on the rate constant k (24.0 kJ mol^{-1} for $PdIn/Al_2O_3$, see Figure 2.15 for details), which was almost identical to that obtained based on the reaction rate r. Considering the significant low activation energy, one might suspect that the reaction is diffusion-limited. However, I can exclude the possibility of diffusion-limited kinetics because PdIn shows catalytic activity similar to that of Pd (< 30%) in this condition, where the reaction rate is limited obviously by some chemical reaction as represented by the high activation energy (86.5 kJ mol^{-1}).

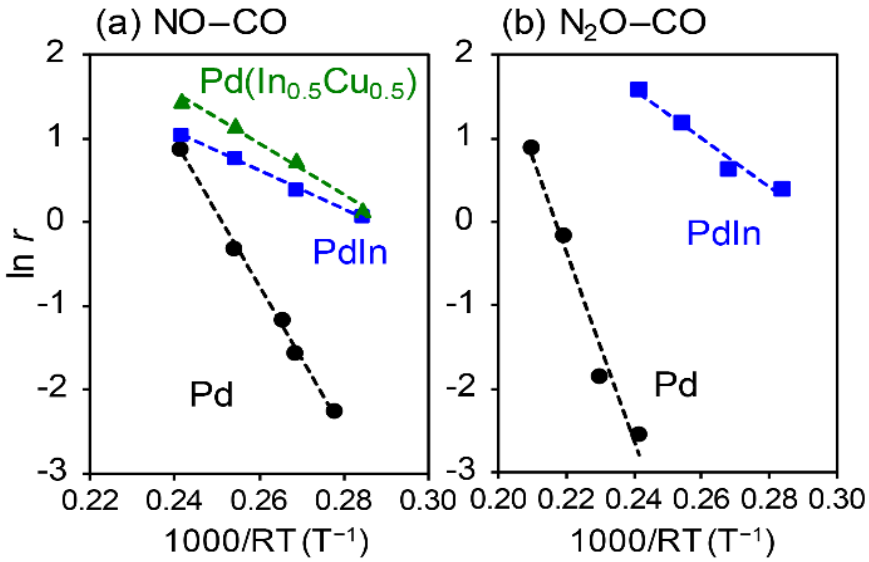

Figure 2.14. Arrhenius-type plots for (a) NO and (b) N_2O reduction by CO using Pd/Al_2O_3, $PdIn/Al_2O_3$, and $Pd(In_{0.5}Cu_{0.5})/Al_2O_3$ catalysts. Reaction rates ($mol \cdot s^{-1} \cdot mol_{Pd}^{-1}$) are evaluated based on CO_2 formation rate.

Table 2.2. Summary of Arrhenius-type plots and kinetic analysis.

	N_2O–CO		NO–CO		
	Pd	PdIn	Pd	PdIn	PdInCu[a]
E_A / kJ mol^{-1}	113.4	28.9	86.5	23.1 (24.0)[b]	30.8
intercept	24.6	8.5	21.7	6.6 (7.6)[b]	8.9
order for P_{NO}	–	–	0.62	1.28	–
order for P_{CO}	–	–	0.55	0.08	–

RDS in NO–CO	$r = kP_{NO}^{x}P_{CO}^{y}$	
(1)	$x = 1$	$-1 < y < 0$
(2)	$-1 < x < 1$	$y = 1$
(3)	$-1 < x < 3$	$-2 < y < 0$
(4)	$-6 < x < 0$	$-2 < y < 0$
(5)	$-4 < x < 2$	$-1 < y < 1$
(6)	$-2 < x < 0$	$-1 < y < 0$
(7)	$-2 < x < 0$	$-1 < y < 0$
(8)	$-1 < x < 1$	$-1 < y < 0$

[a] $Pd–In–Cu/Al_2O_3$ (Pd:In:Cu =2:1:1) was used as a catalyst. [b] Estimated by Arrhenius plot based on rate constant *k*.

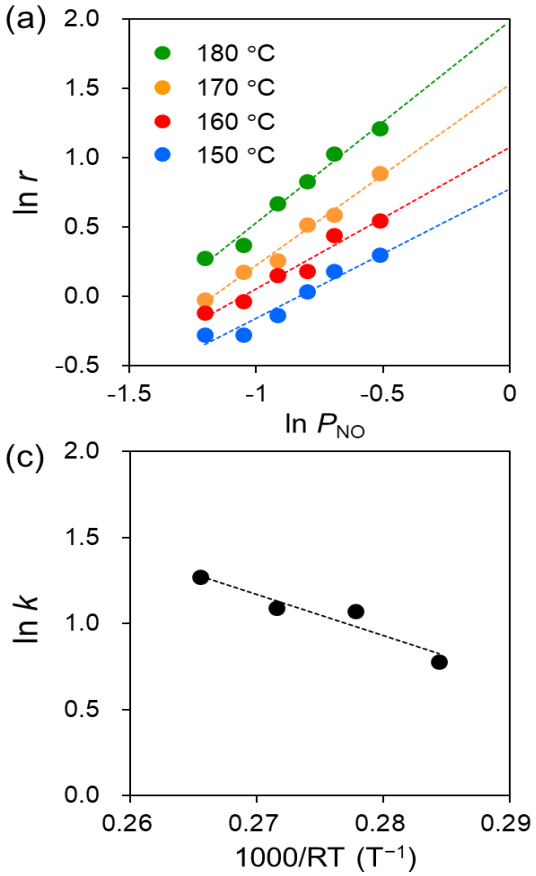

(b)

$$r = kP_{NO}{}^{\alpha}P_{CO}{}^{\beta}$$

$$\ln r = \ln k + \alpha \ln P_{NO} + \beta \ln P_{CO}$$

$$\ln r = \ln k + \alpha \ln P_{NO} \quad (\beta \approx 0)$$

$$\ln k = \ln A - \frac{E_a}{RT}$$

(d) summary of (a)

temp. / °C	slope (α)	intercept ($\ln k$)
150	0.93	0.78
160	1.02	1.07
170	1.30	1.09
180	1.45	1.27

summary of (c)

slope ($-E_a$)	intercept ($\ln A$)
−24.0	7.6

Figure 2.15. (a) Dependence of reaction rate on NO partial pressures (P_{NO}) in NO reduction by CO over $PdIn/Al_2O_3$. (b) Rate equations for NO reduction by CO. β can be regarded as zero from the result of Figure 2.16. This approximation allows to obtain ln k as the intercept of the linear line in (a). (c) Arrhenius plot for NO reduction by CO over $PdIn/Al_2O_3$. (d) Summary of the data from (a) and (c). Note that the slope α ranges from 0.9 to 1.5, which is consistent with the reaction order suggested from the kinetic analysis in Table 2.

A similar low activation energy was also observed for Pd–In–Cu (30.8 kJ mol^{-1}), suggesting that Cu-substitution did not strongly affect the kinetics in this temperature region. To understand the rate-determining step (RDS), a kinetic analysis was performed on the basis of the reaction orders for NO and CO pressures (P_{NO} and P_{CO}) in NO reduction by CO (Figure 2.16).

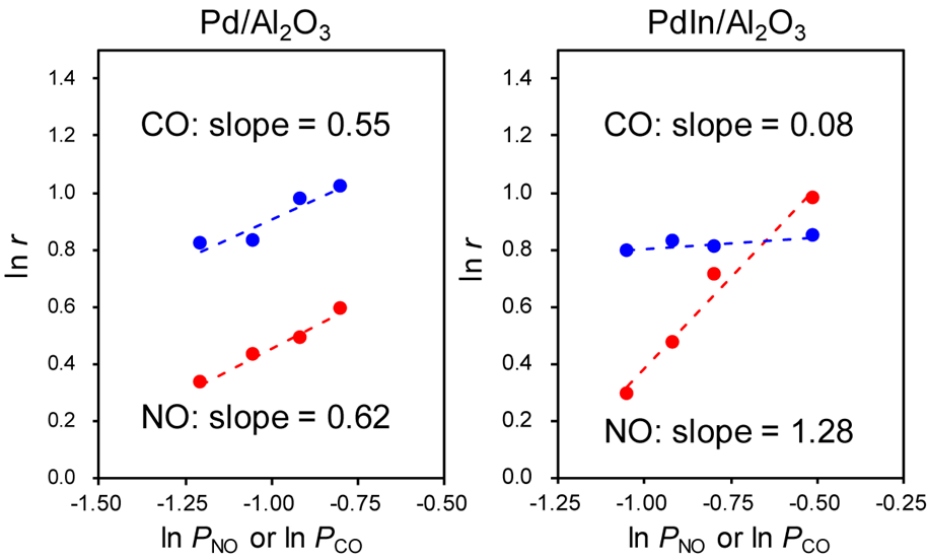

Figure 2.16. Dependence of reaction rate on NO and CO partial pressures (P_{NO} and P_{CO}, respectively) in NO reduction by CO over Pd/Al_2O_3 and $PdIn/Al_2O_3$

Table 2.2 summarizes the experimental reaction orders for P_{NO} and P_{CO}, which were positive for both Pd and PdIn catalysts. The observed reaction orders (not equal to unity) also suggest that the reaction rate is not limited by gas-diffusion. In this study, I considered an extended Langmuir–Hinshelwood mechanism with N_2O decomposition/sorption processes as follows:

$NO + \sigma \rightleftharpoons NO{\cdot}\sigma$	(1): NO adsorption
$CO + \sigma \rightleftharpoons CO{\cdot}\sigma$	(2): CO adsorption
$NO{\cdot}\sigma + \sigma \rightleftharpoons N{\cdot}\sigma + O{\cdot}\sigma$	(3): NO dissociation
$2N{\cdot}\sigma \rightarrow N_2 + 2\sigma$	(4): N_2 formation
$CO{\cdot}\sigma + O{\cdot}\sigma \rightarrow CO_2 + 2\sigma$	(5): CO oxidation (CO_2 formation)
$N{\cdot}\sigma + NO{\cdot}\sigma \rightleftharpoons N_2O{\cdot}\sigma + \sigma$	(6): N_2O formation
$N_2O{\cdot}\sigma \rightleftharpoons N_2 + O{\cdot}\sigma$	(7): N_2O decomposition
$N_2O{\cdot}\sigma \rightleftharpoons N_2O + \sigma$	(8): N_2O desorption/readsorption

where, σ indicates a vacant site. Steps (1)~(5) are identical to those considered in the conventional kinetic models for NO–CO reaction over Pd[13, 48, 49] and Rh[13, 50, 51] catalysts.

The modified points are that N_2O is once formed as an adsorbate (6) and that N_2O decomposition and sorption are taken into account (7, 8), which are the crucial factors for determining N_2 selectivity in the present system. I solved the rate equation of each step regarded as the RDS using the overall site balance and equilibrium constants for other steps except (4) and (5), where reverse reactions can be ignored under the atmospheric pressure conditions (see Supporting Information "Kinetic Analysis" for details). Table 2.2 shows the reaction orders for P_{NO} and P_{CO} derived from the equations. In most cases, the reaction order for P_{CO} is negative, which is inconsistent with the observed experimental result. Conversely, when (5) is considered rate-determining, the orders for P_{NO} and P_{CO} ranges from −4 to +2 and from −1 to +1, respectively, which agree with the experimental values. Thus, our kinetic study demonstrated that the oxidation of CO by surface oxygen was the RDS in NO reduction by CO. The order for P_{NO} was increased, whereas that for P_{CO} was decreased by the formation of the PdIn phase. This implies that NO adsorption becomes much less favorable than CO adsorption on PdIn. The observed features are quite different from those reported for conventional monometallic Pd catalysts, where the order for P_{CO} was typically negative[13, 48] and NO dissociation (3)[52, 53] or N_2 formation (4)[49] have been considered as the RDS. This discrepancy may stem from the difference in reaction temperature: our kinetic study was performed at a temperature (150°C) that is much lower than that used in the literature (~280°C).[13, 48] CO oxidation can easily proceed at such high temperatures, where the RDS may be shifted to other steps. However, as clearly shown in the light-off temperature of CO conversion in the NO–CO reaction over Pd (Figure 2.17), CO oxidation seems to be very slow at temperatures lower than 200°C. The enhancement in CO oxidation will provide a larger amount of vacant active Pd sites, thus allowing the promotion of NO and N_2O adsorption and low-temperature activity and N_2 selectivity, respectively. This effect will be discussed in detail later.

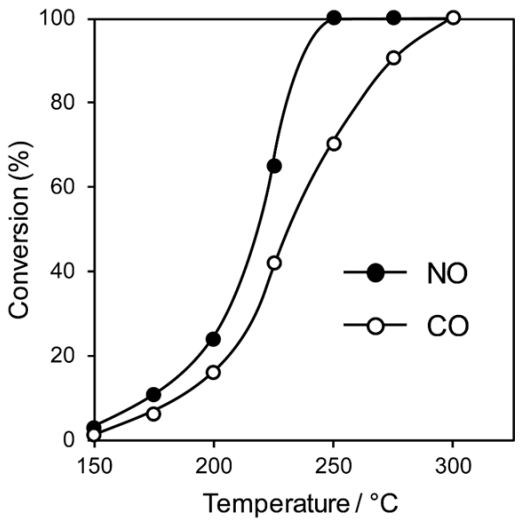

Figure 2.17. Conversion of NO and CO in NO reduction by CO over Pd/Al_2O_3 catalyst.

2.3.4 Operando XAFS

To clarify the role of PdIn phase on the catalysis of NO reduction, I performed an operando XAFS study during reactions with NO and/or CO. The changes in the oxidation states of Pd and In were monitored on the basis of the features of XANES. I here used 1 wt% Pd/Al_2O_3 and $PdIn/Al_2O_3$ catalysts, of which Pd dispersions are higher than those of 3 wt% catalysts (for PdIn, 18% and 11% for 1 wt% and 3 wt% catalysts, respectively), so that the information about surface was included as much as possible in the overall information. After in-situ H_2 pretreatment at 400°C, these catalysts showed Pd K (for Pd and PdIn) and In K (for PdIn) edge XANES spectra that are similar to those of zero-valent references (Pd black and In foil, respectively, Figure 2.18a and b), supporting the complete reduction of Pd and PdIn phases. For Pd K, the adsorption edge of PdIn was slightly lower in energy than Pd, suggesting that Pd atoms in PdIn are electron-enriched compared with those in pure Pd (Figure 2.18a); these findings are consistent with the result of CO-FT-IR. For In K edge XANES, the white line ($1s \rightarrow 5p$ transition) area of PdIn was larger than that of In foil (Figure 2.18b), indicating that the electron occupancy in 5p orbital (In: [Kr] $5s^2$ $4d^{10}$ $5p^1$) decreased probably due to charge transfer from In to Pd. After the H_2 pretreatment and a 10 min He purge, reactant

gases (NO+CO mixture, NO, and CO) were flowed for 20 min with 10 min intervals of He purge (the changes in XANES spectra are shown in Figure 2.18c and d). Figure 2.19a shows the change in the fraction of Pd^{2+} or In^{3+} species in the catalyst estimated by the linear combination fitting of the XANES spectra (see Figure 2.20 for an example of the fitting).

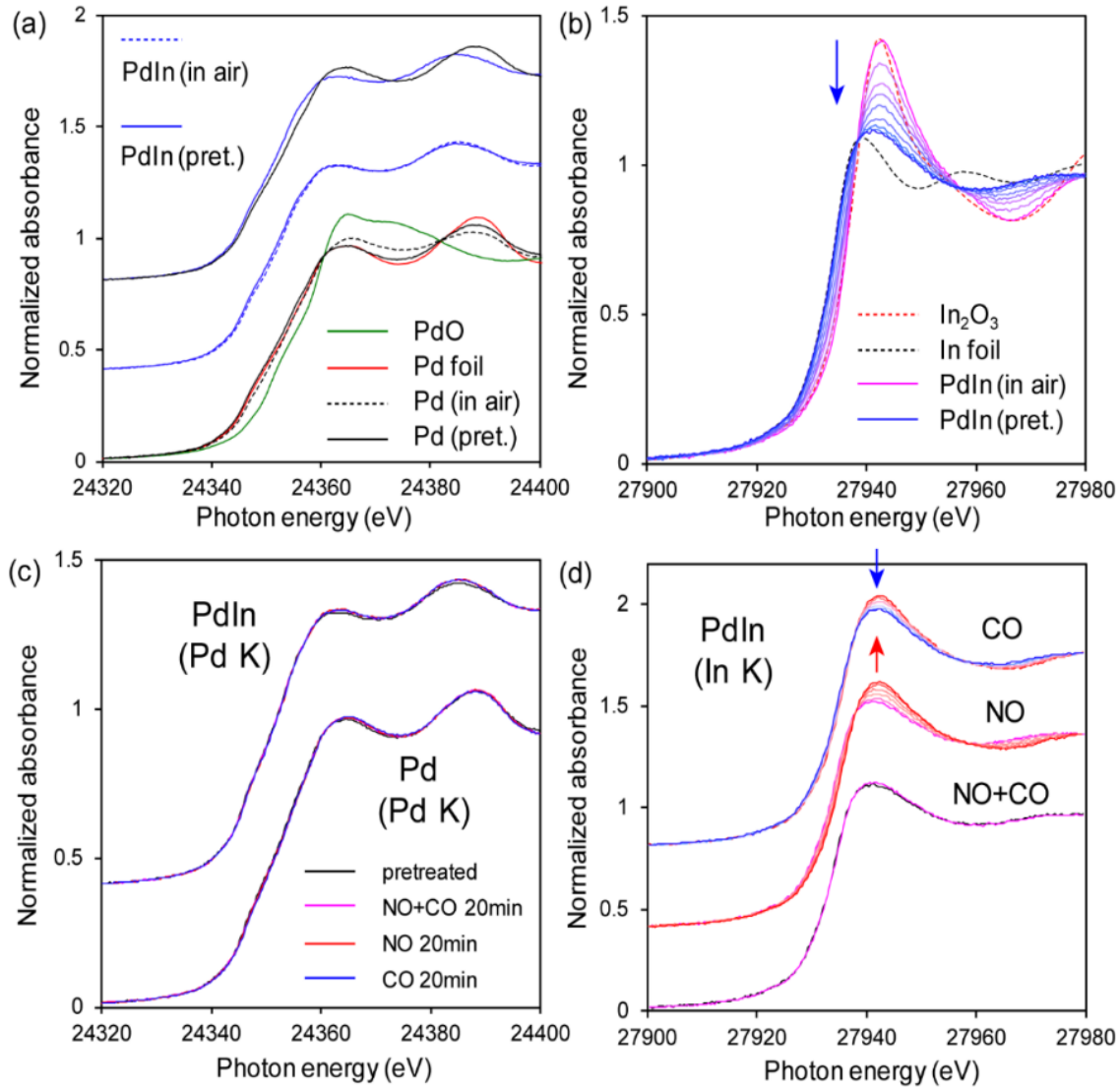

Figure 2.18. (a) Pd K and (b) In K-edge XANES spectra of Pd/Al_2O_3 and $PdIn/Al_2O_3$ catalyst before (in the air) and after (pret.) H_2 pretreatment at 400°C for 20 min. Changes in the XANES spectra (c) after and (d) during 20 min contact with flowing NO + CO, NO, and then CO at 200°C.

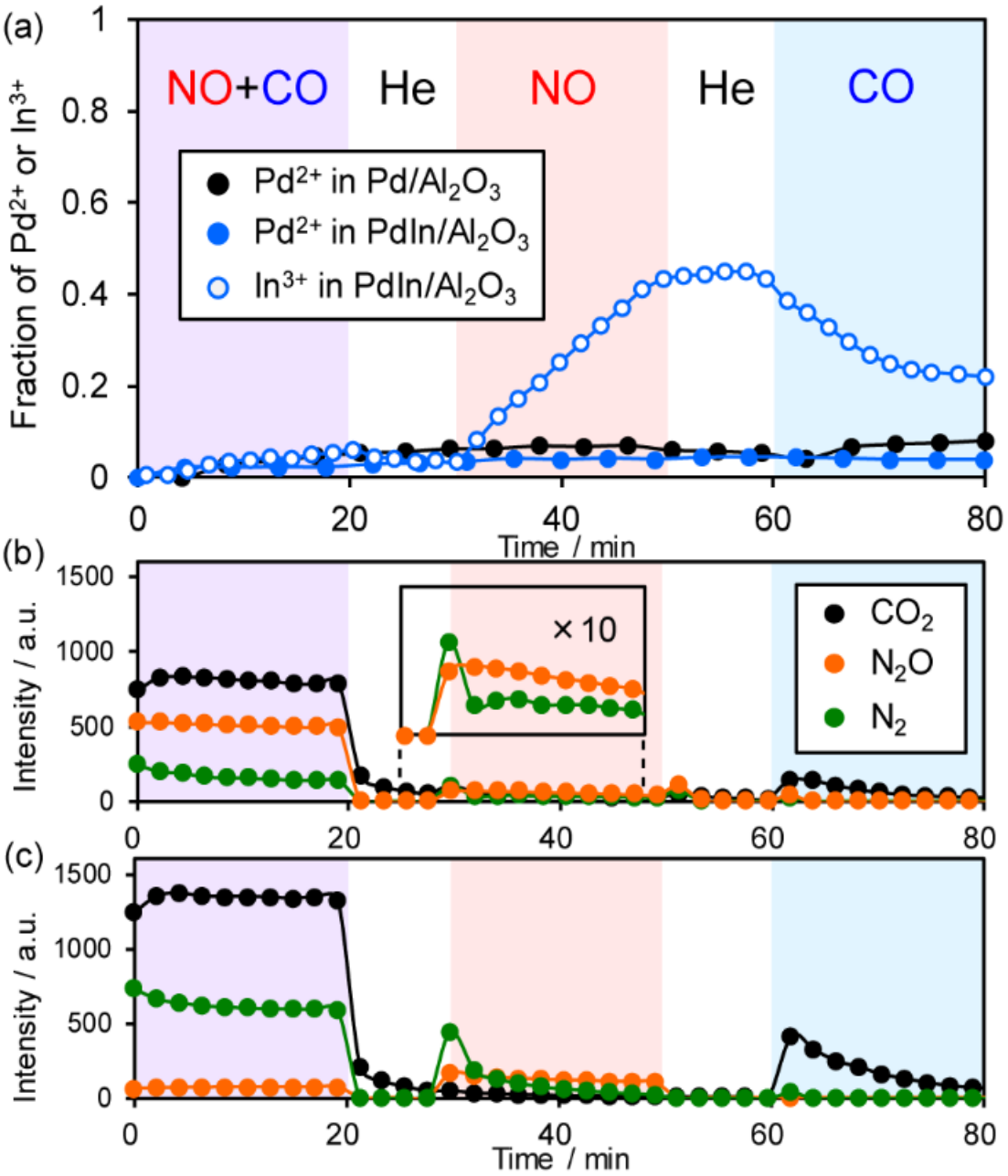

Figure 2.19. (a) Changes in the fraction of Pd^{2+} and In^{3+} species in Pd and PdIn catalysts during contact with NO + CO, NO, and CO at 200°C. The corresponding changes in the product distribution in the gas phase for (b) Pd and (c) PdIn are also shown.

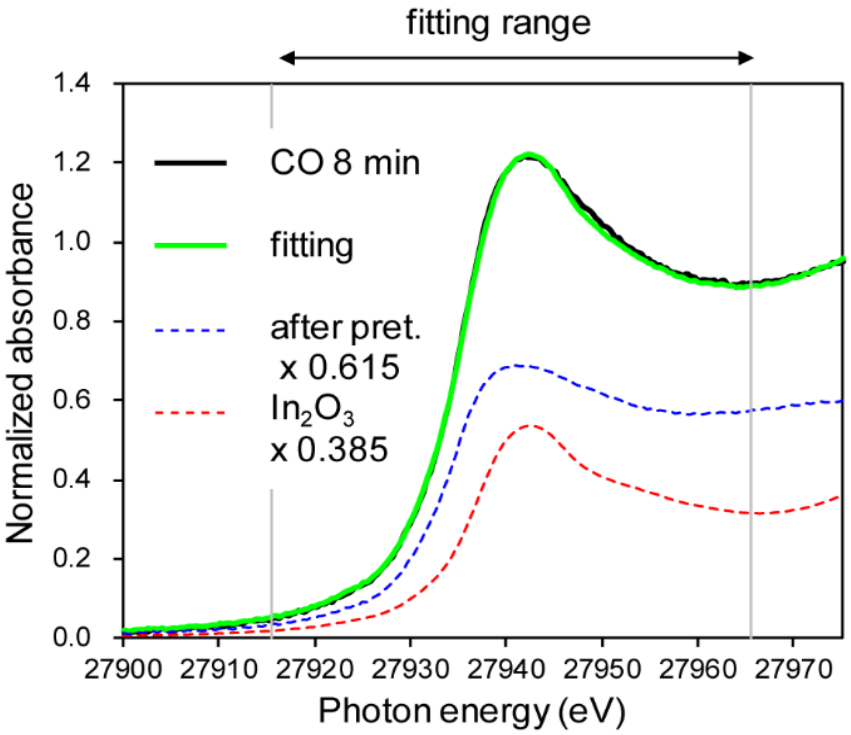

Figure 2.20. Linear combination fitting for a XANES spectrum during NO reduction by CO.

The corresponding changes in the product distribution in the gas phase were shown in Figure 2.19b and c. During contact with NO and CO, the fractions of the oxidized species were quite low (< 0.05) for both Pd and PdIn catalysts (Figure 2.19a). In the gas phase, N_2, N_2O, and CO_2 were detected (Figure 2.19b and c), showing that NO reduction by CO proceeded. The N_2 selectivity was 22~32% and 89~92% for Pd and PdIn, respectively; these values are close to those observed in Figure 2.3b. Thus, it was confirmed that the PdIn catalyst retained the metallic states of Pd and In during the catalytic NO reduction by CO. The presence of only a small amount of oxidized species indicates that oxygen atoms derived from NO dissociation are present at the catalyst surface but do not form any oxide phases. Note that their fractions are lower than the Pd dispersion, suggesting that the oxygen coverage does not reach saturation. In the case of PdIn, the fraction of In^{3+} was slightly higher than that of Pd^{2+}. This implies that the

surface oxygen atoms bind preferentially to In probably because of its intrinsic greater oxophilicity than Pd, i.e., higher oxidation potential ($In^{(0)} = In^{3+} + 3e^-$: 0.338 V; $Pd^{(0)} = Pd^{2+} + 2e^-$: −0.915 V; vs. NHE).[54]

When only NO was introduced to Pd and PdIn catalysts, the fraction of In^{3+} in PdIn increased gradually with time up to ca. 0.4, whereas those of Pd^{2+} in Pd and PdIn did not change. Furthermore, small amounts of N_2 and N_2O were evolved in the gas phase at the initial stage of NO flowing, suggesting that NO dissociation and the subsequent N+N and N+NO reactions occur, but are inhibited rapidly by the accumulation of oxygen at the catalyst surface. For PdIn, considering the difference in In^{3+} and Pd^{2+} fractions, the oxygen atoms could also be captured by subsurface In to generate Pd–In_2O_3 composite at the shell part of the PdIn nanoparticles. N_2 was mainly evolved only at the earliest stage; thereafter, N_2O formation dominated. This is probably because the association probability of two N atoms is decreased with increasing O coverage, thus making N+NO reaction in an Eley–Rideal fashion favorable instead. Note that no significant difference in this trend was observed between Pd and PdIn, implying that In does not strongly inhibit the pathway of N_2O formation.

Finally, when CO was introduced, the fraction of In^{3+} in the PdIn catalyst decreased with a small evolution of CO_2. This clearly demonstrates that In_2O_3 was reduced by CO to form metallic In and CO_2. However, the reduction of In_2O_3 was not completed at this condition, suggesting the difficulty of removing oxygen in the bulk using CO as a reductant at 200°C. On the contrary, the fraction of Pd^{2+} in Pd and PdIn did not decrease during the contact with CO despite the formation of CO_2 even on Pd. A possible interpretation is that the saturation coverage of CO on Pd sites and the resulting strong back donation make Pd slightly electron deficient.

Thus, operando XAFS analysis revealed that (a) In undergoes the redox cycle of In^{3+}–$In^{(0)}$ via the reaction with NO and CO, (b) the parent PdIn phase is retained in the steady-state of NO reduction by CO, and (c) In acts as an oxygen acceptor (in other

words, an oxygen storage/release material). This redox property of PdIn can also be observed in our recent study on the oxidative dehydrogenation of 1-butene to 1,4-butadiene using O_2 at 400°C.[55] In this case, intermetallic PdIn nanoparticles were oxidized by O_2 to form a Pd–In_2O_3 composite, followed by the reconstruction of the parent PdIn nanoparticles by contact with 1-butene. The PdIn phase was retained in the copresence of O_2 and 1-butene even at 400°C. This self-reconstruction capability of PdIn would work even under three-way catalysis conditions, where reducing agents stronger than CO, such as hydrocarbon and hydrogen, are also present.

2.3.5 DFT calculations

Finally, DFT calculations for the relevant elementary steps were performed to obtain further information in an atomic scale. To understand the selectivity trend, we focused on N_2O decomposition ($N_2O \rightarrow N_2 + O$), CO oxidation ($O + CO \rightarrow CO_2$), and N_2 formation ($N + N \rightarrow N_2$) steps over the terrace and/or stepped surfaces of Pd and PdIn. The dissociation of NO ($NO \rightarrow N + O$) was also studied in a similar fashion to follow the activity trend. Figure 2.21 illustrates the views of representative adsorbates and Table 2.3 summarizes the adsorption energy (E_{ad}), reaction energy (ΔE), and activation energy (E_A) for each molecule and step. For N_2O decomposition, conversions from on-top linear N_2O to bidentate bended N_2O to dissociated N_2 and O were considered.[56] The second bond dissociation step typically gave higher E_A than the first molecular bending step except for Pd(111), where the bending step showed a relatively high E_A (29.3 kJ mol^{-1}).

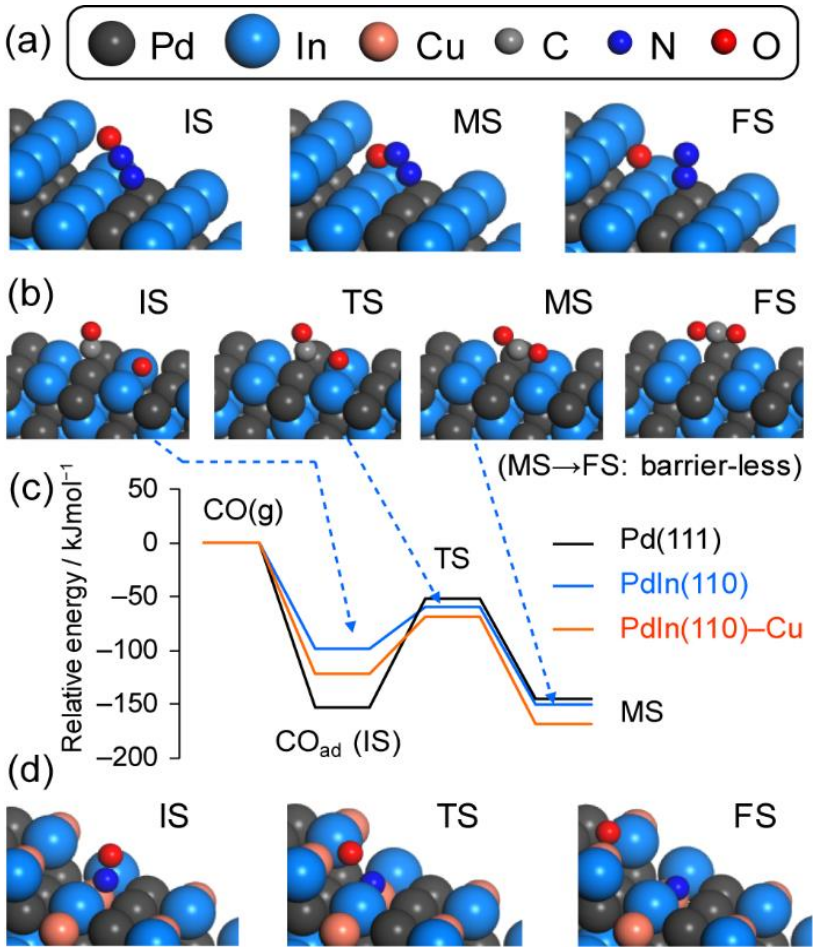

Figure 2.21. Molecular transformation calculated by DFT: (a) N_2O decomposition over In-edged PdIn(120), (b) CO oxidation over PdIn(110), (c) energy diagram of CO oxidation, and (d) NO dissociation over Cu-substituted PdIn(120). IS, TS, MS, and FS indicate the initial, transition, intermediate, and final states, respectively. For (c), the total energy of gas-phase CO and O-preadsorbed slab was set to zero for each surface.

PdIn(110) terrace gave an E_A that is significantly lower than those of all Pd surfaces calculated. It is surprising that N_2O decomposition on In-edged PdIn(120), which is stepped (110), was almost barrierless (E_A < 0.1 kJ mol^{-1}). Therefore, PdIn surfaces are much more active for N_2O decomposition than Pd. This may be due to the oxophilic character of metallic In, which is likely to provide significantly stabilized TSs for bond dissociation. On the contrary, the E_{ad} of N_2O was close to each other between the PdIn and Pd surfaces.

Table 2.3. Adsorption (E_{ad}), reaction (ΔE), and activation (E_A) energies in various elementary steps over Pd and PdIn surfaces calculated by DFT.

surface	E_{ad} / kJ mol^{-1}	ΔE / kJ mol^{-1}	E_A / kJ mol^{-1}	E_A reported	ref.
$N_2O \rightarrow N_2 + O$ [a]					
Pd(111)	−38.8	−110.2	9.3 (29.3)	(56.9)	52
Pd(100)	−53.8	−104.9	61.8 (13.5)		
Pd(511)	−54.6	−123.2	46.3		
PdIn(110)	−32.2	−107.7	18.6 (3.7)		
PdIn(120)	−60.0	−105.0	<0.1 (0)		
$O + CO \rightarrow CO_2$ [b]					
Pd(111)	−153.0	−33.2	100.1	98.4	56
PdIn(110)	−98.9	−134.3	39.4		
PdIn(110)-Cu	−122.0	−44.6	53.4		
$N + N \rightarrow N_2$					
Pd(111)		−190.2	77.9		
PdIn(110)		−353.4	86.1		
$NO \rightarrow N + O$					
Pd(100)	−276.0	158.1	158.1	157.3	58
Pd(511)	−257.0	41.5	100.2	115.8	58
PdIn(110)	−110.3	46.8	167.3		
PdIn(120)	−120.9	27.2	111.8		
PdIn(120)-Cu	−191.6	−7.0	100.2		

[a] Energies for bidentate N_2O are shown. EA for the bending step (from linear to bidentate N_2O) is shown in parenthesis. [b] E_{ad} for CO adsorption on O-preadsorbed (not clean) surface was shown.

CO oxidation over PGM surface has been extensively studied using surface science techniques[57-59] and theoretical calculations.[60, 61] For example, the calculated activation energies for Pd(111) range from 90 to 144 kJ mol^{-1} depending on the coverage.[60, 61] Our calculation for 1/4 the coverage of CO on Pd(111) (100.1 kJ mol^{-1}) well reproduced the corresponding reported value (98.4 kJ mol^{-1})[60] and it was close to the experimental value obtained in the present study (113 kJ mol^{-1}). On the contrary, CO oxidation over PdIn(110) gave a much lower E_A (39.4 kJ mol^{-1}) than Pd(111) and was close to that obtained from the Arrhenius-type plot (29 kJ mol^{-1}). Thus, the calculation showed good agreements with the reported theoretical and the present experimental values. The remarkable decrease in E_A for PdIn could be explained by the weaker adsorption of CO

(less negative E_{ad}: −98.9 > −153.0 kJ mol^{-1}). This is clearly represented in the energy diagram for CO adsorption and the subsequent oxidation (Figure 2.21c): the relative total energies are similar, except for the adsorbed state of CO (initial state of CO oxidation). The weaker adsorption of CO makes the initial state unstable, resulting in a lower energy barrier. I also considered the effect of Cu substitution for PdIn on the CO oxidation ability. The substitution of some In atoms to Cu atoms at the PdIn(110) surface resulted in a more negative E_{ad} and a slightly higher E_A, indicating that Cu substitution does not enhance the CO oxidation ability of PdIn.

Considering the large difference between the E_A of N_2O decomposition and CO oxidation, CO oxidation should be the RDS for N_2O–CO reaction. Therefore, the remarkable decrease in the activation energy of CO oxidation can be the reason why the N_2O–CO activity and N_2 selectivity in NO–CO reaction were drastically improved. The calculation also revealed that N_2O decomposition itself was also greatly promoted over PdIn surface. This promotion effect may also contribute to the overall N_2 selectivity in NO–CO reaction. I also focused on the N_2 formation step because the acceleration of this step can contribute to enhanced N_2 selectivity in NO–CO reaction. However, no significant difference in E_A was observed between Pd(111) and PdIn(110) surfaces.

NO dissociation over transition metal surface has also been long studied as for CO oxidation.[27, 62-65] Sautet et al.[27] reported that E_A of NO dissociation at the step of Pd(511) was 115.8 kJ mol^{-1}, which was much lower than that on Pd(111) and (100) terraces (216 and 160 kJ mol^{-1}, respectively). The DFT calculation for monometallic Pd surfaces reproduced the reported E_A (100.2 and 158.1 kJ mol^{-1} for (511) and (100) surfaces, respectively). A similar trend in E_A was observed for PdIn, where the (120) surface (stepped (110)) showed a much lower E_A than the flat (110) surface (111.8 and 167.3 kJ mol^{-1}, respectively). The decrease in E_A at the step sites can be rationalized by a geometric effect. Given that the O atom of NO in the on-top conformation is distant from the surface, NO dissociation at the terrace sites requires large atomic displacement

without stabilization. Conversely, the step sites allow less atomic displacements and stabilization of TS owing to the spatial adjacency of the metal atoms and O (Figure 2.22). These suggest that NO dissociation over PdIn, as well as that over pure Pd and Rh frequently advocated in the literature, is structure sensitive.[27, 49, 62, 66] However, the E_A of PdIn surfaces were slightly higher than those of Pd surfaces. Moreover, E_{ad} on PdIn were much less negative than those of Pd as observed for CO. The weakening of NO adsorption on PdIn was more prominent than that of CO adsorption (E_{ad} of NO: −276.0 → −110.3 kJ mol^{-1}, E_{ad} of CO: −153.0 → −98.9 kJ mol^{-1}). This result indicates that CO adsorption on PdIn is relatively favored compared with that on Pd, consistent with the experimental change in the reaction orders of P_{NO} and P_{CO} mentioned in the kinetic study. Therefore, the PdIn surface has no promotion effect on NO adsorption and dissociation compared with pure Pd. By contrast, the Cu-substituted PdIn(120) surface, which is a model of a Pd($In_{1-x}Cu_x$) pseudo-binary alloy surface (Figure 2.21d), showed a different trend. The E_{ad} of NO becomes more negative (−120.9 → −191.6 kJ mol^{-1}) by Cu substitution. E_A was also decreased to the level of Pd(511). Thus, Cu substitution enhanced both NO adsorption and dissociation, consistent with the improved catalytic activity in NO–CO reaction. The decrease in E_A by Cu-substitution should be attributed to the drastically lowered ΔE from positive to negative (+27.2 → −7.0 kJ mol^{-1}). This result could be attributed to the fact that the final dissociated state is significantly stabilized by the incorporation of Cu, which has greater azophilicity (affinity to N) than typical metal elements.[67] Thus, Cu substitution from In drastically modified the electronic feature of the catalyst and the catalytic performance.

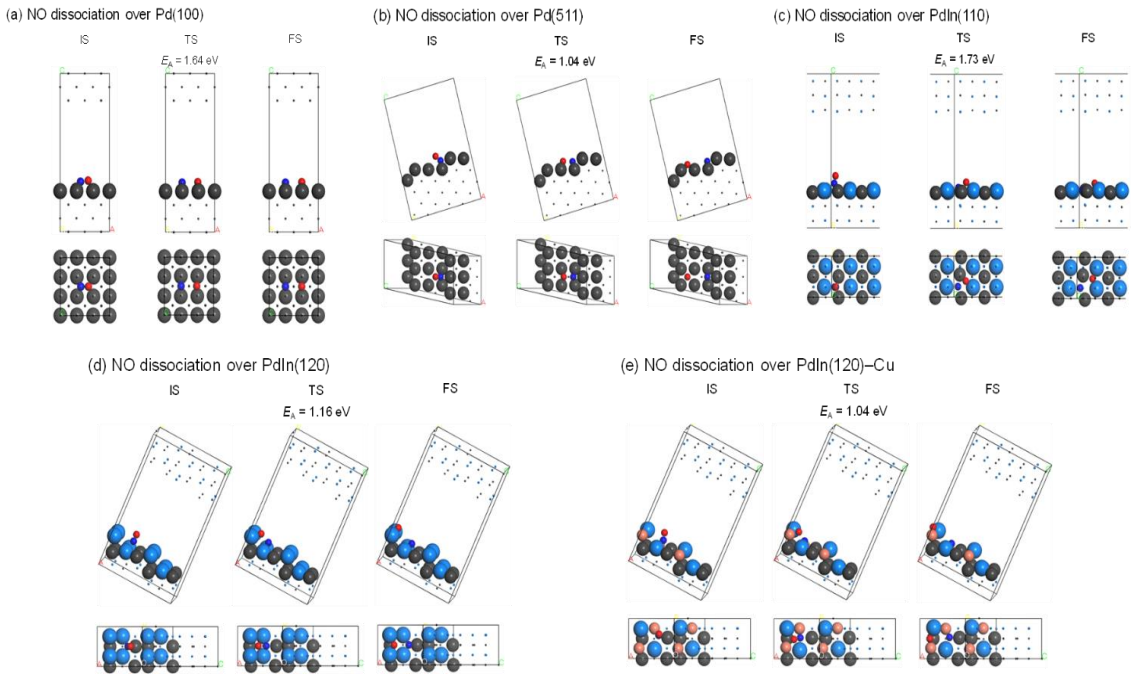

Figure 2.22. Structures of adsorbates and the corresponding transition states during NO dissociation over (a) Pd(100) and (b) Pd(511), (c) PdIn(110), (d) PdIn(120), and (e) Cu-substituted PdIn(120). For clarity, metal atoms in the sub-surface region are shown as small dots.

Finally, I investigated the effect of the electronic state on the observed catalysis. I focused on the character of valence electrons, which strongly affects the adsorptivity and reactivity. It is known that d-band center can be a good descriptor for these surface chemical behaviors.[68-71] Generally, the lower the center is, the weaker the adsorption is. I calculated the density of state (DOS) diagrams projected onto the d orbitals of the relevant catalyst surfaces: Pd(111), PdIn(110), PdCu(110), and Pd($In_{0.33}Cu_{0.67}$)(110) (Figure 2.23). The order of the d-band center position was PdCu (−2.07 eV) > Pd (−2.32 eV) > Pd($In_{0.33}Cu_{0.67}$) (−2.64 eV) > PdIn (−3.05 eV). The d-band of PdIn was significantly down-shifted below −2.0 eV, because of the hybridization with low energy 4d electrons of In (< −10 eV).[72] On the other hand, PdCu has an intense DOS peak near −1.1 eV derived from Cu,[73] which uplifted the d-band center. Pd($In_{0.33}Cu_{0.67}$) displayed

an intermediate DOS diagram due to the contribution of both In and Cu, thus showing the moderate d-band center. The order of d-band center agreed finely with those of E_{ad} of NO and CO and E_A of CO oxidation (Figure 2.23): strong positive correlations were observed between the d-band center and the adsorption strength or the energy barrier. Therefore, the observed trend in the electronic states and chemical behaviors could be understood based on the d-band theory.

2.3.6 Effect on N_2 selectivity

CO oxidation is very slow at the low-temperature region (< 225°C), thus limiting the overall reaction rate of NO and N_2O reduction. The coverages of CO and O are likely to be high, which strongly inhibits re-adsorption of N_2O and the subsequent decomposition to N_2 and O. Considering the sufficiently low E_A of N_2O decomposition over Pd and PdIn, the decomposition should smoothly proceed once after N_2O is adsorbed with the bidentate conformation. Therefore, providing the vacant active Pd sites is an important factor for N_2O decomposition, particularly at low temperatures. PdIn promotes CO oxidation, thus providing more active sites.

The other key factor for N_2 selectivity can be the difference in N_2O capturing and decomposing abilities. Considering the large difference in the E_{ad} of N_2O and NO or CO (ca. 220 kJ mol^{-1} for Pd(100)), N_2O adsorption to Pd is extremely inhibited by the strong competitive adsorption of NO and CO. Therefore, N_2O adsorption and decomposition may not be sufficiently enhanced only by releasing active sites. On the contrary, the adsorption of NO and CO for PdIn is drastically weakened as demonstrated by the kinetic and DFT studies, whereas the E_{ad} of N_2O were almost the same between Pd and PdIn. It should be noted that the difference in the E_{ad} of N_2O and NO is decreased to ca. 60 kJ mol^{-1} on PdIn(120). This result indicates that N_2O adsorption on PdIn in the presence of NO and CO is more favorable than that on Pd. This is probably because oxophilic In captures the oxygen atom of N_2O in the bidentate conformation.

Besides, PdIn possesses a greater ability to decompose N_2O than Pd, as highlighted in the barrierless conversion at the stepped surface. Considering that N_2O desorption competes with N_2O decomposition, the faster N_2O decomposition should play an important role in the overall N_2 selectivity. Thus, the PdIn surface provides more vacant active sites, captures N_2O more favorably, and decomposes it very smoothly. I concluded that the triple combination of these effects for N_2O decomposition allows the excellent N_2 selectivity in NO reduction by CO even at low temperatures.

2.3.7 Effect on low-temperature activity

CO oxidation is the RDS of NO reduction by CO in low-temperature region (< 225°C). The PdIn phase significantly accelerates this step owing to the lowered activation barrier, resulting in the enhancement in the overall reaction rate. In other words, NO conversion is increased by releasing a larger amount of vacant active sites. In this context, it is interesting that the promotion of CO oxidation contributes to the enhancements in both selectivity and activity. I also propose another effect of PdIn on the low-temperature activity. As revealed by the DFT calculation and kinetic study, CO adsorption on PdIn is relatively favored compared with NO adsorption. Indeed, considering that the reaction order of P_{CO} is close to zero, the CO coverage seems to reach near saturation. Therefore, the higher concentration of adsorbed CO should increase the reaction rate of CO oxidation. Thus, CO oxidation over PdIn is accelerated by decreased E_A and increased CO coverage. By contrast, as mentioned in the paragraph of DFT calculation, the substitution of In by Cu does not enhance CO oxidation, thus causing low-temperature activity in NO reduction. Therefore, the observed increase in NO conversion by Cu-substitution in the low-temperature region may be attributed to the improved metal dispersion.

Here, one may wonder why CO oxidation on PdIn becomes the RDS even though the corresponding E_A (~30 kJ mol^{-1}) is much lower than that of other steps such as NO

dissociation (E_A: ~100 kJ mol^{-1}). Considering the large difference in E_A between Pd and PdIn (~70 kJ mol^{-1}), the rate constants are expected to differ in an order of 10^7 at 200°C, which is much higher than the actual increase in the reaction rate in an order of 10^1. This discrepancy can be explained by the difference in the pre-exponential factors. As suggested in the Arrhenius-type plots (Figure 2.14), the intercepts of the linear lines significantly differ (Pd: 23.2, PdIn: 8.6, Table 2.2), which roughly reflects that the pre-exponential factors differ in several orders of magnitude. In the literature of CO oxidation, such small pre-exponential factors have been observed[74] and are accompanied typically by low apparent activation energies and high coverages. This is probably because of the rarity of CO oxidation on PdIn, in which the reaction pathway is geometrically limited by highly ordered atomic arrangement and the specific location of CO and O (Pd top and $PdIn_2$ hollow sites, Figure 2.21b).

2.3.8 Effect on high-temperature activity

In contrast to the low-temperature region, the kinetics of NO reduction by CO changes drastically at a high-temperature region (> 225°C). CO oxidation smoothly proceeds (Figure 2.17), hence it is no longer the RDS. NO dissociation, which has significantly high E_A, is more likely to be rate-determining. For PdIn, the lower NO adsorption and dissociation abilities decrease the overall reaction rate, which is reflected in the low NO conversion at the high-temperature region (Figure 2.3a). This drawback of PdIn can be improved by the partial substitution of In with Cu as mentioned in Figure 2.8. The high-temperature activity (NO conversions at 250 and 275°C) increased as the Cu content in $Pd(In_{1-x}Cu_x)$ increased. This is because NO adsorption and dissociation is facilitated by the incorporation of Cu, as demonstrated by DFT calculation. However, the excess amount of Cu (x = 0.9) results in a sharp drop in the low-temperature activity (NO conversions at 150~200°C), which is probably due to excessively strengthened CO adsorption. The low- and high-temperature activities derived from In and Cu,

respectively, are compatible at the optimum Cu content (x = 0.67), thus affording remarkably high catalytic activity and selectivity in a wide range of reaction temperatures.

2.3.9 Effect of Electronic factor

As summarized in Figure 2.23, In significantly lowers the d-band center, while Cu recovers the drop close to the level of Pd. The lowered d-band center makes NO and CO adsorption weaker. The weaker CO adsorption decreases E_A for CO oxidation because the TS energies are almost identical regardless of the surface (Figure 2.10c). This effect contributes to the enhanced catalytic activity in the low-temperature region. On the other hand, the weaker NO adsorption inhibits NO dissociation, which suppresses the catalytic activity in the high-temperature region. NO adsorption is promoted with the aid of Cu substitution, which contributes to the greater catalytic activity in the high-temperature region. However, the trend in NO dissociation ability is not straightforward, since other factors such as the intrinsic azophilicity of Cu, ΔE, and/or the adsorption configuration are also involved.

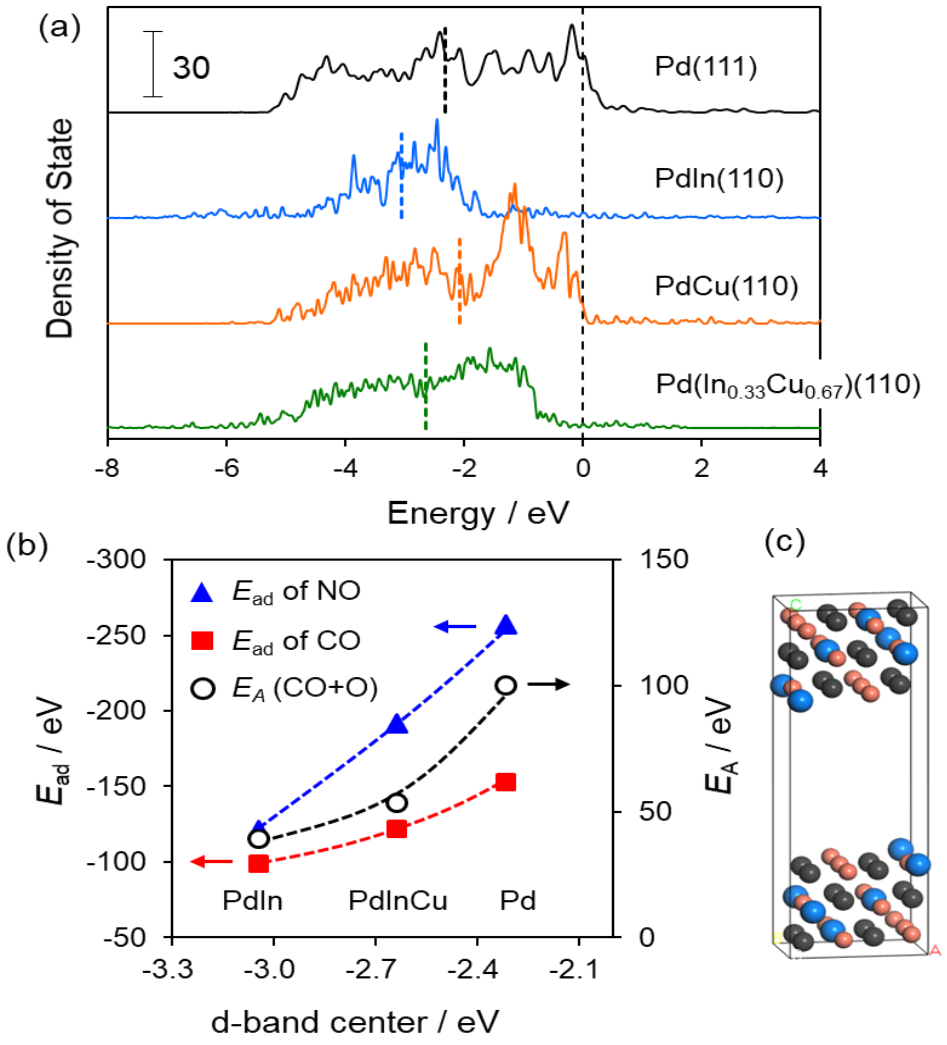

Figure 2.23. (a) Projected density of states (DOS) of 4d orbitals on Pd(111), PdIn(110), PdCu(110), and Pd($In_{0.33}Cu_{0.67}$)(110) surfaces. The vertical dashed and the bold dotted lines indicate the Fermi level and the position of the d-band center, respectively. (b) Correlations between the position of d-band center and E_{ad} of NO or CO and E_A of CO oxidation. (c) Slab model of Pd($In_{0.33}Cu_{0.67}$)(110) used for DOS calculation.

2.4 Conclusion

In the present study, I prepared a series of Pd-based intermetallic compounds supported on alumina (PdM/Al_2O_3, M = Cu, In, Pb, Sn, and Zn) and tested them in NO reduction by CO. PdIn exhibited a remarkably high N_2 selectivity in a wide range of temperatures (> 200°C) and NO conversion than pure Pd at a low-temperature region (<

200°C), whereas low conversion was displayed in the high-temperature region (> 200°C). The catalytic performance of PdIn was remarkably improved by the substitution of a part of In by Cu to form Pd($In_{1-x}Cu_x$) pseudo-binary alloys, where high NO conversion and N_2 selectivity were achieved at various temperature regions (> 175°C). The optimized catalyst, namely, Pd($In_{0.33}Cu_{0.67}$)/Al_2O_3, allows the complete conversion of NO to N_2 even at 200°C, which has never been achieved using metallic catalysts to the best of our knowledge. The formation of the pseudo-binary alloy structure with In–Cu substitution was supported by HAADF-STEM and EXAFS analyses, where the lattice constant was decreased by the incorporation of Cu atoms smaller than In atoms and no In–Cu bond was observed in the first coordination shell. The mechanistic study based on kinetic analysis and DFT calculation revealed the role of In and Cu as follows: (1) In accelerates CO oxidation, which is the RDS at the low-temperature region, thus providing a higher number of vacant active sites for NO dissociation (low-temperature activity) and N_2O decomposition (N_2 selectivity); (2) N_2O decomposition ability itself is also enhanced by the formation of the PdIn phase; and (3) the incorporation of Cu improves NO adsorption and dissociation, which may be the RDS at the high-temperature region. Thus, the combination of the positive effects of In and Cu enables the development of a highly active and selective NO reduction by CO at various temperature regions. Note that this combination is allowed only when In atoms in the PdIn phase is replaced by Cu with an appropriate ratio. The present study provides not only a highly efficient catalytic system for deNO_x, but also deep insights in NO reduction and CO oxidation and a novel concept for flexible catalyst design based on the pseudo-binary alloy structure.

References

1. P. Pacher, J. S. Beckman and L. Liaudet, *Physiol. Rev.*, 2007, **87**, 315-424.
2. B. C. Berks, S. J. Ferguson, J. W. B. Moir and D. J. Richardson, *BBA Bionerg.*, 1995, **1232**, 97-173.
3. F. Rezaei, A. A. Rownaghi, S. Monjezi, R. P. Lively and C. W. Jones, *Energ. Fuel.*, 2015, **29**, 5467-5486.
4. C. Monn, *Atmos. Environ.*, 2001, **35**, 1-32.
5. J. H. Wang, H. Chen, Z. C. Hu, M. F. Yao and Y. D. Li, *Catal. Rev.*, 2015, **57**, 79-144.
6. J. H. Holles, R. J. Davis, T. M. Murray and J. M. Howe, *J. Catal.*, 2000, **195**, 193-206.
7. A. Srinivasan and C. Depcik, *Catal. Rev.*, 2010, **52**, 462-493.
8. J. Shibata, M. Hashimoto, K. Shimizu, H. Yoshida, T. Hattori and A. Satsuma, *J. Phys. Chem. B*, 2004, **108**, 18327-18335.
9. W. Z. An, Q. L. Zhang, K. T. Chuang and A. R. Sanger, *Ind. Eng. Chem. Res.*, 2002, **41**, 27-31.
10. R. Burch, J. P. Breen and F. C. Meunier, *Appl. Catal. B: Environ.*, 2002, **39**, 283-303.
11. M. Haneda, M. Todo, Y. Nakamura and M. Hattori, *Catal. Today*, 2017, **281**, 447-453.
12. S. B. Kang, J. B. Lim, D. Jo, I. S. Nam, B. K. Cho, S. B. Hong, C. H. Kim and S. H. Oh, *Chem. Eng. J.*, 2017, **316**, 631-644.
13. J. H. Holles, M. A. Switzer and R. J. Davis, *J. Catal.*, 2000, **190**, 247-260.
14. Z. P. Liu, S. J. Jenkins and D. A. King, *J. Am. Chem. Soc.*, 2004, **126**, 10746-10756.
15. Z. P. Liu, S. J. Jenkins and D. A. King, *J. Am. Chem. Soc.*, 2003, **125**, 14660-14661.
16. S. Furukawa and T. Komatsu, *ACS Catal.*, 2017, **7**, 735-765.
17. L. Zhang, I. A. W. Filot, Y. Q. Su, J. X. Liu and E. J. M. Hensen, *J. Catal.*, 2018, **363**, 154-163.
18. S. Furukawa, G. Nishimura and T. Komatsu, *J. Jpn. Petrol. Inst.*, 2016, **59**, 160-163.
19. B. Ravel and M. Newville, *J. Synchrotron Radiat.*, 2005, **12**, 537-541.
20. M. D. Segall, P. J. D. Lindan, M. J. Probert, C. J. Pickard, P. J. Hasnip, S. J. Clark and M. C. Payne, *J. Phys. Condens. Mat.*, 2002, **14**, 2717-2744.
21. D. Vanderbilt, *Phys. Rev. B*, 1990, **41**, 7892-7895.
22. J. P. Perdew, K. Burke and M. Ernzerhof, *Phys. Rev. Lett.*, 1996, **77**, 3865-3868.
23. A. Tkatchenko and M. Scheffler, *Phys. Rev. Lett.*, 2009, **102**, 073005-1–073005-4.
24. H. J. Monkhorst and J. D. Pack, *Phys. Rev. B*, 1976, **13**, 5188-5192.
25. J. Y. Ye, C. J. Liu and Q. F. Ge, *Phys. Chem. Chem. Phys.*, 2012, **14**, 16660-16667.
26. J. Ye, Q. Ge and C. J. Liu, *Chem. Eng. Sci.*, 2015, **135**, 193-201.
27. D. Loffreda, D. Simon and P. Sautet, *J. Catal.*, 2003, **213**, 211-225.
28. T. H. Fischer and J. Almlof, *J. Phys. Chem.*, 1992, **96**, 9768-9774.

29. N. Govind, M. Petersen, G. Fitzgerald, D. King-Smith and J. Andzelm, *Comp. Mater. Sci.*, 2003, **28**, 250-258.
30. T. A. Halgren and W. N. Lipscomb, *Chem. Phys. Lett.*, 1977, **49**, 225-232.
31. I. R. Harris, M. Norman and A. W. Bryant, *J. Less-Common Met.*, 1968, **16**, 427-440.
32. D. W. Lane, G. J. Conibeer, D. A. Wood, K. D. Rogers, P. Capper, S. Romani and S. Hearne, *J. Cryst. Growth*, 1999, **197**, 743-748.
33. T. Suzuki and Y. Oya, *J. Mater. Sci.*, 1981, **16**, 2737-2744.
34. M. H. Mendelsohn and D. M. Gruen, *J. Less-Common Met.*, 1981, **78**, 275-280.
35. H. C. Donkersloot and J. H. Vanvucht, *J. Less-Common Met.*, 1970, **20**, 83-91.
36. A. Kjekshus, R. Mollerud, A. F. Andresen and W. B. Pearson, *Philos. Mag.*, 1967, **16**, 1063-1083.
37. H. Seto, Y. Noda and Y. Yamada, *J. Phys. Soc. Jpn.*, 1990, **59**, 965-977.
38. C. Wang, D. P. Chen, X. Sang, R. R. Unocic and S. E. Skrabalak, *ACS Nano*, 2016, **10**, 6345-6353.
39. K. Krompholz and A. Weiss, *J. Less-Common Met.*, 1976, **50**, 213-222.
40. S. Bhan and H. Kudielka, *Z. Metallkd.*, 1978, **69**, 333-336.
41. L. Pauling, *J. Am. Chem. Soc.*, 1947, **69**, 542-553.
42. W. K. Kuhn, J. Szanyi and D. W. Goodman, *Surf. Sci.*, 1992, **274**, L611-L618.
43. T. Komatsu, M. Takasaki, K. Ozawa, S. Furukawa and A. Muramatsu, *J. Phys. Chem. C*, 2013, **117**, 10483-10491.
44. T. Hager, H. Rauscher and R. J. Behm, *Surf. Sci.*, 2004, **558**, 181-194.
45. N. Lopez and J. K. Norskov, *Surf. Sci.*, 2001, **477**, 59-75.
46. H. Iwamoto, S. Kameoka, Y. Xu, C. Nishimura and A. P. Tsai, *J. Phys. Chem. Solids*, 2019, **125**, 64-73.
47. A. V. Zeigarnik, *Kinet. Catal.*, 2003, **44**, 233-246.
48. D. R. Rainer, M. Koranne, S. M. Vesecky and D. W. Goodman, *J. Phys. Chem. B*, 1997, **101**, 10769-10774.
49. D. R. Rainer, S. M. Vesecky, M. Koranne, W. S. Oh and D. W. Goodman, *J. Catal.*, 1997, **167**, 234-241.
50. S. H. Oh, *J. Catal.*, 1990, **124**, 477-487.
51. S. H. Oh, G. B. Fisher, J. E. Carpenter and D. W. Goodman, *J. Catal.*, 1986, **100**, 360-376.
52. P. Granger, F. Dhainaut, S. Pietrzik, P. Malfoy, A. S. Mamede, L. Leclercq and G. Leclercq, *Top. Catal.*, 2006, **39**, 65-76.
53. P. Granger, C. Dujardin, J. F. Paul and G. Leclercq, *J. Mol. Catal. A: Chem.*, 2005, **228**, 241-253.

54. A. J. Bard, R. Parsons and J. Jordan, *Standard potentials in aqueous solution*, CRC press, 1985.
55. S. Furukawa, M. Endo and T. Komatsu, *ACS Catal.*, 2014, **4**, 3533-3542.
56. X. Wei, X.-F. Yang, A.-Q. Wang, L. Li, X.-Y. Liu, T. Zhang, C.-Y. Mou and J. Li, *J. Phys. Chem. C*, 2012, **116**, 6222-6232.
57. T. Engel and G. Ertl, *J. Chem. Phys.*, 1978, **69**, 1267-1281.
58. V. Zhdanov, *Surf. Sci.*, 1984, **137**, 515-526.
59. F. Zaera, J. Liu and M. Xu, *J. Chem. Phys.*, 1997, **106**, 4204-4215.
60. C. Zhang and P. Hu, *J. Am. Chem. Soc.*, 2001, **123**, 1166-1172.
61. A. Eichler, *Surf. Sci.*, 2002, **498**, 314-320.
62. B. Hammer, *Faraday Discuss.*, 1998, **110**, 323-333.
63. B. Hammer, *J. Catal.*, 2001, **199**, 171-176.
64. E. Ozensoy and D. W. Goodman, *Phys. Chem. Chem. Phys.*, 2004, **6**, 3765-3778.
65. C. Hess, E. Ozensoy, C.-W. Yi and D. W. Goodman, *J. Am. Chem. Soc.*, 2006, **128**, 2988-2994.
66. S. M. Vesecky, P. Chen, X. Xu and D. W. Goodman, *J. Vac. Sci. Technol., A*, 1995, **13**, 1539-1543.
67. S. Furukawa, R. Suzuki and T. Komatsu, *ACS Catal.*, 2016, **6**, 5946-5953.
68. B. Hammer and J. K. Norskov, *Nature*, 1995, **376**, 238-240.
69. B. Hammer and J. K. Norskov, *Surf. Sci.*, 1996, **359**, 306-306.
70. B. Hammer, Y. Morikawa and J. K. Norskov, *Phys. Rev. Lett.*, 1996, **76**, 2141-2144.
71. B. Hammer, *Top. Catal.*, 2006, **37**, 3-16.
72. F. Fuchs and F. Bechstedt, *Phys. Rev. B*, 2008, **77**, 155107.
73. L. Barbosa, D. Loffreda and P. Sautet, *Langmuir*, 2002, **18**, 2625-2635.
74. V. P. Zhdanov, *Surf. Sci. Rep.*, 1991, **12**, 185-242.

Chapter 3

A Cu-Pd Single-Atom Alloy Catalyst for Highly Efficient NO Reduction

3.1 Introduction

The reactions of nitric oxide (NO) have garnered intense interest from researchers in the human health,[1] and bioinorganic,[2] industrial,[3] and environmental chemistry fields.[4] Specifically, NO removal has long been studied as an indispensable process for exhaust-gas purification.[5] Platinum-group metals (PGMs) such as Pt, Pd, and Rh are known to be efficient catalysts for the reduction of NO using CO,[6,7] H_2,[8] NH_3,[9] and hydrocarbons[10] as reductants. The recent challenges in this field involve developing catalytic systems that function (1) at low temperatures under cold-start conditions,[11] (2) with minimum use of PGMs,[12,13] and (3) without emitting N_2O,[14–16] which is a potent greenhouse gas.[17] These issues have been individually studied using different materials. The development of a single material that enables (1)–(3) is therefore highly desirable. To the best of our knowledge, no such material has been reported. In particular, achieving both (1) and (3) is difficult because N_2O reduction to N_2 on PGMs requires relatively high temperatures (> 300°C).[18] Therefore, an appropriate catalyst design is needed to obtain not only outstanding catalytic activity toward NO reduction but also high selectivity to N_2 with minimal incorporation of PGMs.

A promising approach that overcomes these challenges is the single-atom alloying concept,[19] which is relevant to single-atom chemistry.[20,21] The dilution of PGM atoms with less active metal atoms not only substantially reduces the use of PGMs but also enables drastic modification of the electronic and geometric structures for enhanced catalysis.[22] For example, the isolation of Pt or Pd with group 11 metals (Au, Ag, and Cu) enables molecular transformations that hardly proceed in the absence of single-atom alloying, such as selective hydrogenation,[23–27] formic acid dehydrogenation,[28] and hydrosilylation.[29] In these systems, the group 11 metals act as inert elements but modify the electronic and geometric factors of the PGM and, thus, its catalytic properties. Conversely, for NO reduction, the group 11 elements are known to be capable of NO activation.[30–32] Therefore, applying the single-atom alloying concept to NO reduction systems should provide an unprecedented synergistic effect for efficient NO conversion.

In this study, I focused on Cu as a main component because of its intrinsic activity toward NO reduction and its high earth abundance. I found that Cu–Pd/Al_2O_3 (Cu/Pd =

5) acts as a highly efficient catalyst for NO reduction at low temperatures (> 150℃), without generating N_2O emissions. Herein, I report both an innovative catalytic system for efficient NO reduction and novel catalytic chemistry of single-atom alloys.

3.2 Experimental section

3.2.1. Catalyst preparation

Boehmite (γ-AlOOH) was supplied by SASOL Chemicals. γ-Al_2O_3 was prepared by the calcination of boehmite at 900℃ for 3 h. Pd/Al_2O_3 (Pd: 2 wt%) and Cu–Pd/Al_2O_3 (Cu: 6 wt%, Cu/Pd = 1) were prepared by a conventional impregnation method. The γ-Al_2O_3 support was added to a vigorously stirred aqueous. The solution containing $Pd(NH_3)_2(NO_2)_2$ (Kojima Chemicals, 4.765 wt% in HNO_3) and/or $Cu(NO_3)_2{\cdot}3H_2O$ (Sigma-Aldrich, 99%), followed by stirring for 3 h at room temperature (50 ml H_2O per gram of Al_2O_3). The mixture was dried under a reduced pressure at 50℃, followed by reduction under flowing H_2 (30 ml min^{-1}) at 400℃ (Pd) or 800℃ (CuPd) for 1 h. The Cu/Al_2O_3 (Cu: 6 wt%) and Cu–Pd/Al_2O_3 (Cu: 6 wt%, Cu/Pd = 3 and 5) catalysts were prepared by a deposition–precipitation method using urea. The γ-Al_2O_3 support was added to a vigorously stirred aqueous solution of $Cu(NO_3)_2{\cdot}3H_2O$ (50 ml H_2O per gram of Al_2O_3). Then, an aqueous solution of urea (Kanto, 99%) was added dropwise to the stirred mixture at room temperature (urea/Cu = 30). The mixture was sealed with a plastic film and kept with stirring at 70℃ for 10 h. After completing the precipitation of $Cu(OH)_2$, the supernatant was decanted and the resulting crude product was washed with deionized water three times, followed by drying under reduced pressure at 50℃ and calcination at 500℃ for 1 h. For Cu/Al_2O_3, the resulting CuO/Al_2O_3 was reduced under flowing H_2 at 400℃ for 1 h. For Cu-Pd/Al_2O_3 (Cu/Pd = 3 and 5), the resulting CuO/Al_2O_3 was used for the successive impregnation of Pd in a similar fashion to that mentioned above. The resulting Pd–CuO/Al_2O_3 was reduced under flowing H_2 at 400℃ for 1 h.

3.2.2 Reaction conditions

The catalyst (0.05 g) diluted with quartz sand (1.95 g, Miyazaki Chemical, 99.9%) was treated under flowing hydrogen (50 ml min^{-1}) at 400℃ for 0.5 h prior to the catalytic reactions. NO reduction by CO was performed in a fixed-bed continuous flow

system by feeding NO (5,000 ppm), CO (5,000 ppm), and He (balance) with a total flow rate of 96 ml min^{-1} (GHSV = 80,000 h^{-1}). The gas-phase was analyzed using an online thermal conductivity detection gas chromatograph (Shimadzu GC-8A, column: SHINWA SHINCARBON ST) located downstream. A stability test was done using twice the amount of catalyst (0.10 g) under similar conditions (GHSV = 40,000 h^{-1}). After a time-on-stream of 24 h, the catalyst was regenerated by flowing hydrogen (50 ml min^{-1}) at 400 C for 0.5 h, followed by continuing the catalytic run. A kinetic study was performed by changing the concentration of NO and CO between 0.3 and 0.6% with that of the counterpart fixed at 0.5%. The reaction temperature was maintained at 150℃ so that NO conversion did not exceed 30%, and the reaction rate (mol s^{-1} mol $_{Pd}{}^{-1}$) was calculated on the basis of NO conversion. NO + CO + O_2 and NO + CO + O_2 + C_3H_6 reactions were performed under stoichiometric conditions as follows: NO (5,000 ppm), CO (10,000 ppm), O_2 (2,500 ppm), He (balance) with a total flow rate of 96 ml min^{-1} (GHSV = 80,000 h^{-1}), and NO (5,000 ppm), CO (5,000 ppm), O_2 (5,625 ppm), C_3H_6 (1,250 ppm), and He (balance) with a total flow rate of 96 ml min^{-1} (GHSV = 80,000 h^{-1}), respectively.

3.2.3 Characterization

The crystal structure of the prepared catalyst was examined by powder X-ray diffraction (XRD) using a Rigaku MiniFlex II/AP diffractometer with Cu Kα radiation. High-angle annular dark-field scanning transmission electron microscopy (HAADF-STEM) was carried out using a JEOL JEM-ARM200 M microscope equipped with an energy dispersive X-ray (EDX) analyzer (EX24221M1G5T). STEM analysis was performed at an accelerating voltage of 200 kV. To prepare the TEM specimen, all samples were sonicated in ethanol and then dispersed on a Mo grid supported by an ultrathin carbon film.

The Fourier-transformed infrared (FT-IR) spectra of adsorbed CO were obtained with a JASCO FTIR-4200 spectrometer equipped with an MCT detector in transmission mode (resolution 4 cm^{-1}). The samples were prepared as self-supporting wafers (2.0 cm diameter, < 0.5 mm thickness) and were placed inside an IR cell with CaF_2 windows. A custom glass manifold was connected to the cell to control the gas for pretreatment and the amount of CO introduced. The cell was first purged with He and the sample was

reduced under flowing hydrogen (50 ml min^{-1}) at 400℃ for 30 min. After reduction, the wafer was cooled to 40℃ under flowing He. The wafer was exposed to CO (0.5%) and He (balance) with a total flow rate of 50 ml min^{-1} for 20 min. After the CO exposure, He was flowed for 5 min to remove the gas phase and weakly adsorbed CO, followed by IR spectral measurements.

X-ray absorption fine structure (XAFS) spectra were recorded on the BL14B2 station at SPring-8 of the Japan Synchrotron Radiation Research Institute. A Si(311) double-crystal monochromator was used. Energy calibration was performed using Pd foil. The spectra were recorded at the edges of Pd K in a transmission mode at room temperature. The pelletized sample was pre-reduced with H_2 at 400℃ for 0.5 h and then sealed in a plastic pack under a N_2 atmosphere together with an ISO A500-HS oxygen absorber (Fe powder). The obtained XAFS spectra were analyzed using Athena and Artemis software ver. 0.9.25 included in the Demeter package. The Fourier transformation of the k^3-weighted EXAFS from k space to R space was performed over a k range of 3.0–15 $Å^{-1}$. Some of the Fourier transformed EXAFS spectra in the R range of 1.2–3.0 Å were inversely Fourier transformed, followed by an analysis using a usual curve fitting method in a *k* range of 3.0–15 $Å^{-1}$. The backscattering amplitude or phase shift parameters were simulated with FEFF 6L and used to perform the curve fitting procedure. For Pd–Cu scattering, intermetallic Cu_3Pd with a Pm-3m structure was considered for the FEFF simulation. The amplitude reduction factor (S_0^2) of Pd was determined to be 0.775 by fitting the spectra of Pd black and then used for fitting of other EXAFS spectra.

3.2.4 Computational details

Periodic DFT calculations were performed using the CASTEP code[33] with Vanderbilt-type ultrasoft pseudopotentials[34] and the Perdew–Burke–Ernzerhof exchange–correlation functional based on the generalized gradient approximation.[35] The planewave basis set was truncated at a kinetic energy of 350 eV, and a Fermi smearing of 0.1 eV was utilized. Dispersion correlations were considered using the Tkatchenko–Scheffler method with a scaling coefficient of S_R = 0.94 and a damping parameter of d = 20.[36] The reciprocal space was sampled using *k*-point mesh with a spacing of typically 0.04 $Å^{-1}$, as generated by the Monkhorst–Pack scheme.[37] Geometry

optimization was performed on supercell structures using periodic boundary conditions. The surface was modeled based on Cu(211)-(2 × 3) (for NO and N_2O related reactions), Cu(111)-(2 × 2) (for CO oxidation), and Cu(111)-(3 × 3) (for N_2O decomposition) slabs that were six atomic layers thick with 13 Å of vacuum spacing. The convergence criteria for structural optimization and energy calculation were set to (a) an SCF tolerance of 1.0×10^{-6} eV per atom, (b) an energy tolerance of 1.0×10^{-5} eV per atom, (c) a maximum force tolerance of 0.05 eV $Å^{-1}$, and (d) a maximum displacement tolerance of 1.0×10^{-3} Å. The transition state search was performed using the complete linear synchronous transit/quadratic synchronous transit (LST/QST) method.[38,39] Linear synchronous transit maximization was performed, followed by energy minimization in the directions conjugate to the reaction pathway. The approximated TS was used to perform QST maximization with conjugate gradient minimization refinements. This cycle was repeated until a stationary point was found. Convergence criteria for the TS calculations were set to root-mean-square forces on an atom tolerance of 0.10 eV $Å^{-1}$.

3.3 Results and discussion

3.3.1. Bimetallic system of Cu-Pd catalyst

The monometallic Cu (6 wt%) and Pd (2 wt%) and the bimetallic Cu–Pd (Cu: 6 wt%, Cu/Pd = 1, 3, or 5; hereafter, Cu_xPd, x = 1, 3, or 5) catalysts were prepared using γ-Al_2O_3 as a support by deposition–precipitation and/or impregnation methods. X-ray diffraction (XRD) patterns of the prepared catalysts revealed that Cu–Pd solid-solution alloy phases with bimetallic compositions similar to the metal ratio in the feed were formed (Figure 3.1 and Table 3.1).

The crystallite sizes estimated using Scherrer's equation were 3–4 nm for all of the catalysts. Figure 3.2a and b show a high angle annular dark-field scanning transmission electron microscopy (HAADF-STEM) image of Cu_5Pd/Al_2O_3 and the size distribution of the nanoparticles, respectively. A relatively narrow size distribution between 2 and 6 nm with an area-weighted mean diameter of 4.2 nm was obtained, consistent with the crystallite size estimated by XRD (Table 3.1).

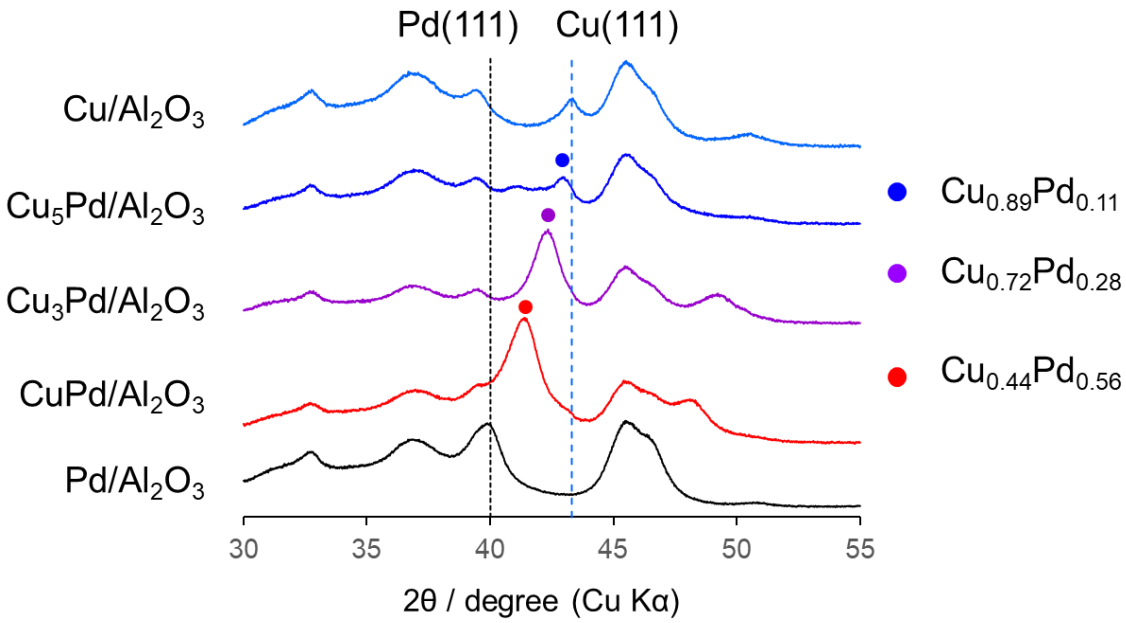

Figure 3.1. XRD patterns of Cu/Al_2O_3, Pd/Al_2O_3, and $Cu–Pd/Al_2O_3$. The Cu–Pd solid-solution alloy phases with bimetallic composition close to that of the fed ratio were formed: Cu/Pd = 1, $Cu_{0.5}Pd_{0.5}$; Cu/Pd = 3, $Cu_{0.75}Pd_{0.25}$; Cu/Pd = 5, $Cu_{0.83}Pd_{0.17}$. The diffraction peak intensity changes depending on the metal loadings as summarized in Table 1.

Table 3.1. Detailed information on the catalyst prepared in this study.

	Pd	CuPd	Cu_3Pd	Cu_5Pd	Cu
Pd loading (wt%)	2.0	10.1	3.4	2.0	0
Cu loading (wt%)	0	6	6.0	6.0	6.0
Cu fraction in the catalysts	0	0.50	0.75	0.83	1.0
Cu fraction in particle	0	0.44	0.72	0.89	1.0
Crystallite size/nm[a]	3.2	3.3	3.8	3.8 (4.2)[b]	4.0

[a] Estimated from Scherrer's equation using a Scherrer constant of 0.477 for the area-weighted mean diameter. [b] Area-weighted means diameter obtained from the TEM image.

Table 3.2. Summary of EXAFS curve fitting for Pd-based catalysts.

Sample	shell	N	R(Å)	ΔE (eV)	σ^2(Å^2)	R-factor
Pd black	Pd–Pd	12 (fix)	2.74 ± 0.00	6.1 ± 0.3	0.006	0.002
Pd/Al_2O_3	Pd–Pd	8.1 ± 0.7	2.73 ± 0.00	4.7 ± 0.6	0.009	0.010
$CuPd/Al_2O_3$	Pd–Cu	4.6 ± 0.6	2.60 ± 0.02	4.7 ± 2.5	0.004	
	Pd–Pd	6.0 ± 0.5	2.65 ± 0.01	3.9 ± 0.8	0.009	0.004
Cu_5Pd/Al_2O_3	Pd–Cu	8.4 ± 0.9	2.57 ± 0.01	2.1 ± 1.3	0.007	0.010

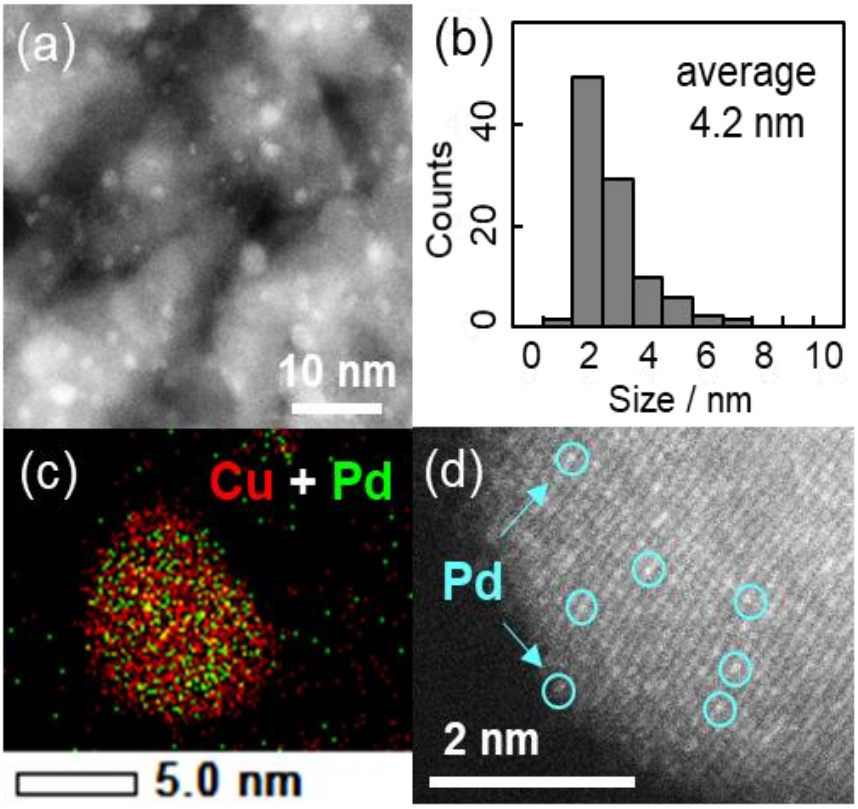

Figure 3.2. (a) HAADF-STEM image of Cu_5Pd/Al_2O_3 and (b) size distribution of the nanoparticles. (c) Elemental map of the Pd + Cu overlayer, as acquired by EDS. (d) High-resolution image of a single nanoparticle.

The energy-dispersive X-ray spectroscopy (EDS) analysis of a single nanoparticle revealed that the Cu and Pd atoms comprising the nanoparticle were homogeneously dispersed (Figure 3.2c). The high-resolution HAADF-STEM image shows an fcc crystal structure viewed along the [100] direction, consistent with the formation of a solid-solution alloy (Figure 3.2d). Moreover, the isolation of Pd atoms by Cu was indicated by the presence of atoms with distinct Z contrasts. Note that the corresponding HAADF-STEM image of Cu/Al_2O_3 showed a weak and uniform Z contrast compared with that of Cu_5Pd/Al_2O_3 (Figure 3.3).

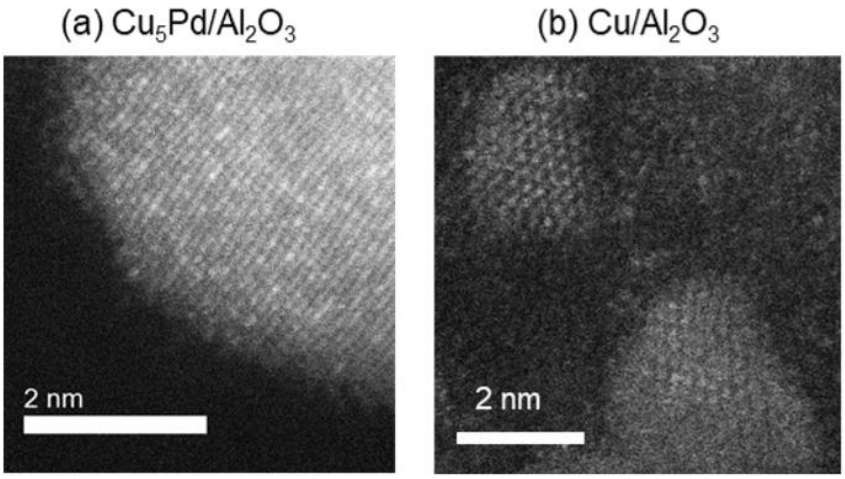

Figure 3.3. HAADF-STEM images of (a) Cu_5Pd/Al_2O_3 and (b) Cu/Al_2O_3

The degree of Pd isolation was further investigated by Fourier-transform infrared (FT-IR) and extended X-ray absorption fine structure (EXAFS) analyses (Figure 3.4). As shown in Figure 3.4a, the FT-IR spectra of CO adsorbed onto Pd/Al_2O_3 exhibited absorption peaks assigned to the stretching vibration of C=O adsorbed on top (2,086 cm^{-1}), bridge (1,975 cm^{-1}), and hollow sites (~1,880 cm^{-1}).[40] Similar absorption peaks were observed for $CuPd/Al_2O_3$, suggesting that the Pd–Pd ensembles largely remain even after 1 : 1 alloying. For Cu-rich samples, an absorption band assignable to CO adsorbed on metallic Cu was also observed at 2,100 nm^{-1}.[41] The peak intensities for the bridge and hollow CO substantially decreased and disappeared in the spectra of Cu_3Pd/Al_2O_3 and Cu_5Pd/Al_2O_3, respectively, indicating that Pd atoms at the surface were isolated upon 5 : 1 alloying. There remained a weak absorption band for linear CO on Pd in the spectrum for Cu_5Pd/Al_2O_3, suggesting that the isolated Pd atoms are also

present at the surface. Figure 3.4b shows the Fourier transforms of the Pd K-edge EXAFS spectra of the Pd-based catalysts $CuPd/Al_2O_3$ showed both Pd–Pd and Pd–Cu bonds, while Cu_5Pd/Al_2O_3 exclusively showed Pd–Cu bonds, suggesting that the Pd atoms in the bulk were also isolated by Cu upon 5 : 1 alloying. Thus, small Cu–Pd nanoparticles with a single-atom alloy structure were successfully formed on the Al_2O_3 support. Considering the limited sensitivity of EXAFS and FT-IR, I cannot completely exclude the presence of Pd–Pd interaction. However, only a small number of Pd–Pd sites, if any, seem not to contribute to the overall catalytic performance.

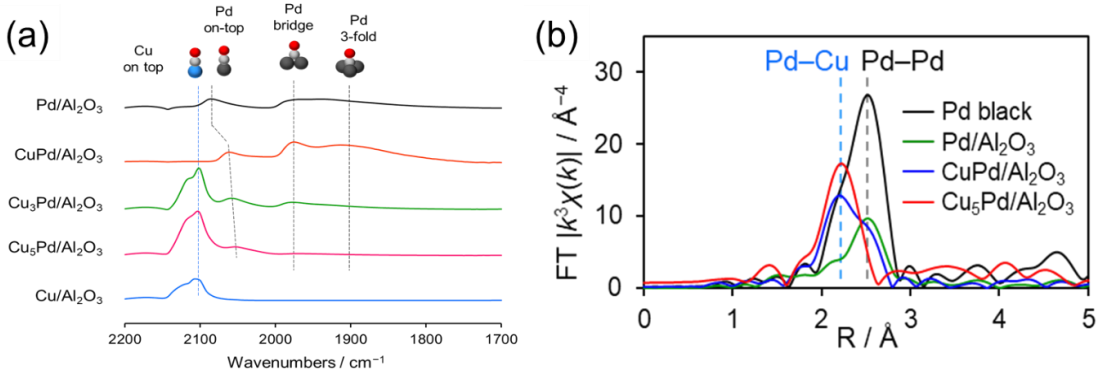

Figure 3.4. (a) FT-IR spectra of CO adsorbed on the prepared catalysts. (b) Fourier transforms of the Pd K-edge EXAFS spectra of the Pd-based catalysts.

3.3.2 Catalytic performance of Cu-Pd system

I next tested the catalytic activity of Cu_xPd/Al_2O_3 in NO reduction by CO (GHSV = 80,000 h^{-1}), as a model reaction for exhaust-gas purification. Figure 3.5a shows the NO conversion to N_2 (C_{N_2}) for the prepared catalysts as a function of reaction temperature. Here, C_{N_2} was obtained by multiplying the NO conversion and the N_2 selectivity (Figure 3.6). Pd/Al_2O_3 gave the lowest C_{N_2}, because of the poor N_2 selectivity < 40% (Figure 3.6b).

Cu/Al_2O_3 exhibited a higher C_{N_2} than Pd/Al_2O_3 because of its much higher N_2 selectivity (Figure 3.6b). $CuPd/Al_2O_3$ showed a C_{N_2} trend similar to that of Cu/Al_2O_3 because of the consequence of increased NO conversion and decreased N_2 selectivity (Figure 3.6). Thus, the 1 : 1 alloy of Cu and Pd gave an insufficient catalytic performance for selective NO reduction. Interestingly, however, both NO conversion and N_2 selectivity increased when the alloying ratio was increased to 3 : 1 and 5 : 1

(Figure 3.6), which resulted in great enhancements in C_{N_2} (Figure 3.5a). NO was completely converted to N_2 over Cu_5Pd/Al_2O_3 without generating N_2O emissions even at 200°C, where Pd showed a C_{N_2} of only 5%. Notably, on going from CuPd to Cu_5Pd, the catalytic activity increased even though the Pd content was decreased to 1/5 (Table 3.1). Therefore, a specific synergistic effect between Cu and Pd likely contributed to the unique properties of the single-atom alloy catalyst. I emphasize that using an excess amount of Pd/Al_2O_3 (0.50 g) with 10 times the equimolar Pd included in Cu_5Pd/Al_2O_3 (labeled as Pd x 10) still resulted in poor performance (Figure 3.5b), highlighting the outstanding performance of the single-atom alloy catalyst. I also tested the long-term stability of Cu_5Pd/Al_2O_3 in NO reduction by CO under standard conditions (GHSV = 40,000 h^{-1}), where 100% C_{N_2} was maintained at 175°C. Although a number of bimetallic catalysts for NO reduction have been reported thus far,[12-16, 42-48] to the best of our knowledge, the present work represents the first success in complete NO_x removal at a temperature less than 200°C. At 150°C, although C_{N_2} decreased slightly at the initial stage because of N_2O formation, it recovered after a short H_2 treatment. This result implies that the accumulation of oxygen species at the catalyst surface triggers the loss of N_2 selectivity and that the catalytic performance could be recovered under rich conditions.

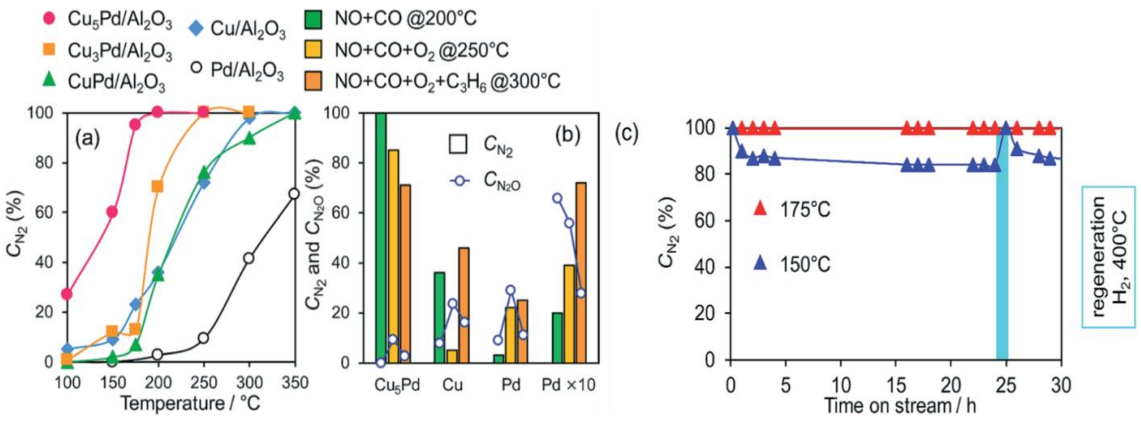

Figure 3.5. (a) NO conversion to N_2 during the NO reduction by CO over Pd, Cu, and Cu-Pd catalysts as a function of reaction temperature (NO, CO: 0.5%, GHSV = 80,000 h^{-1}). (b) Comparison between C_{N_2} and C_{N_2O} in NO reduction in the presence of O_2 and C_3H_6. (c) Stability test for Cu_5Pd/Al_2O_3 in the NO + CO reaction at low temperatures (NO, CO: 0.5%, GHSV = 40,000 h^{-1}).

I next examined the catalytic performance of Cu_5Pd/Al_2O_3 in NO reduction in the presence of O_2 and O_2 + C_3H_6; these conditions more closely resemble those encountered in practical use. Cu/Al_2O_3 delivered poor performance under NO + CO + O_2 conditions. By contrast, Cu_5Pd/Al_2O_3 exhibited much higher performance than Cu/Al_2O_3 and Pd/Al_2O_3. Notably, Cu_5Pd/Al_2O_3 still exhibited a performance better than or C_3H_6, respectively (Figure 3.5b and 7; a comparison with comparable to "Pd x 10" even in the presence of O_2 or O_2 + C_3H_6 temperature dependence and T_{50} is presented in Figure 3.7). Furthermore, N_2O evolution was sufficiently suppressed over Cu_5Pd, where the C_{N_2O} (NO conversion to N_2O, Figure 3.5b and 7) was much lower than those for Pd. Thus, the single-atom alloy catalyst enabled not only a decrease in the noble metal use to 1/10 but also highly selective NO_x removal. In the reactions conducted in the presence of O_2 and O_2 + C_3H_6, reaction temperatures greater than 200°C were needed to achieve sufficient catalytic performance (Figure 3.5 and 7). A possible explanation is that the number of active sites for NO reduction decreased because of the involvement of other reactions such as CO and/or C_3H_6 oxidation.

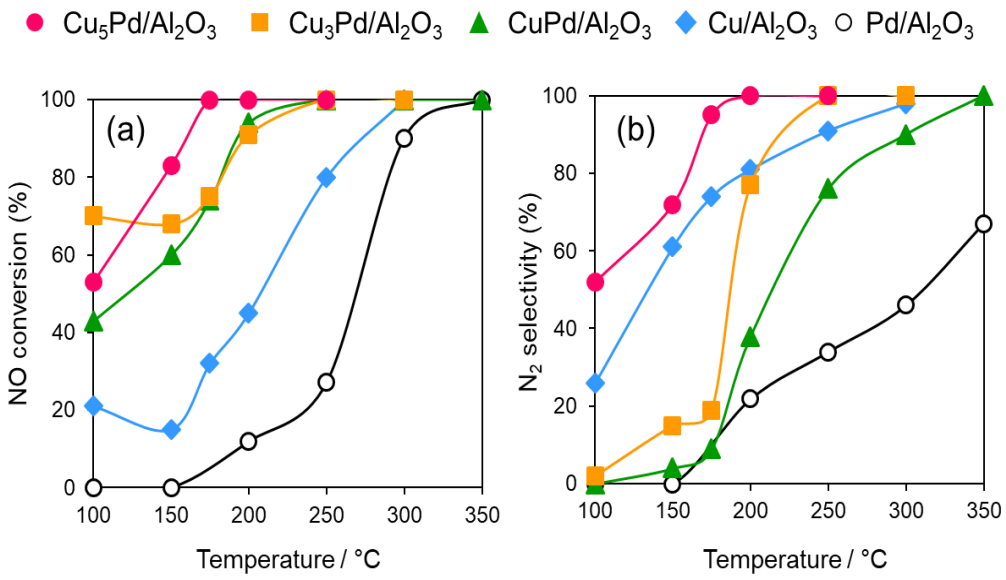

Figure 3.6. (a) NO conversion and (b) N_2 selectivity in NO + CO reaction over Pd/Al_2O_3, Cu/Al_2O_3, and Cu_xPd/Al_2O_3 catalysts.

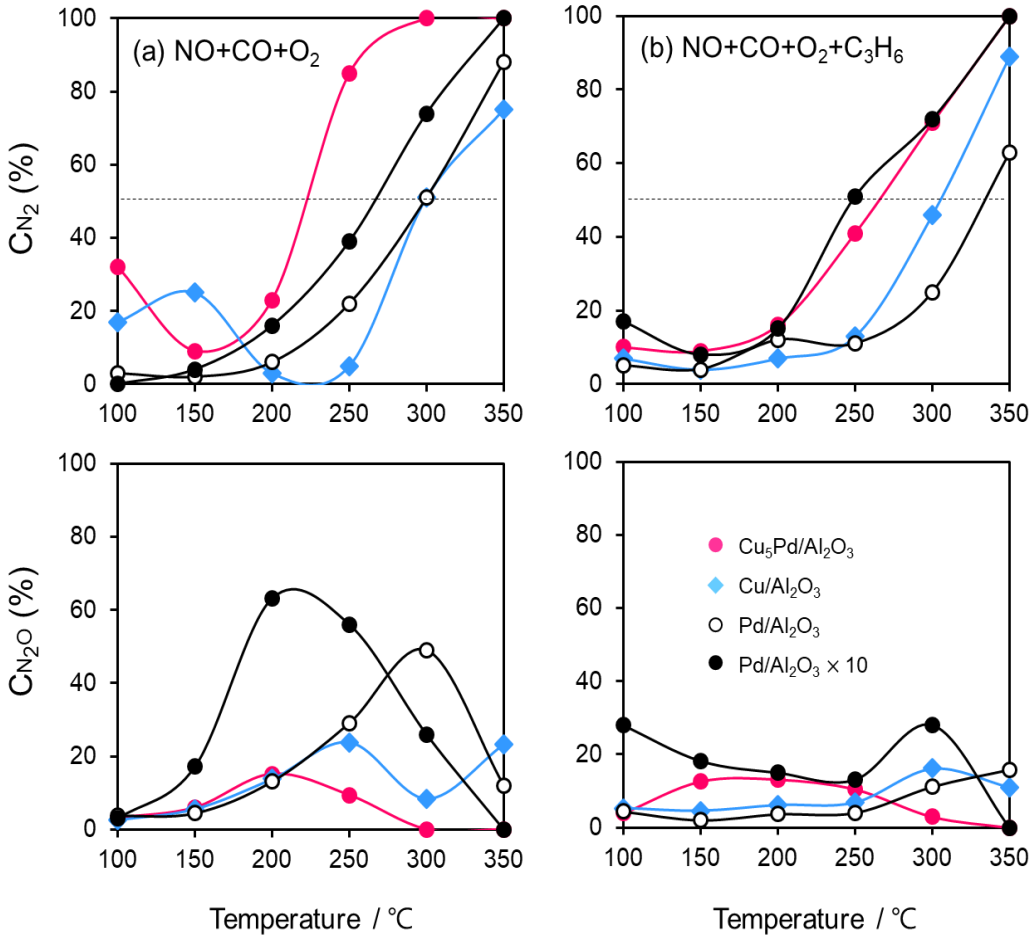

Figure 3.7. CN_2 and CN_2O in NO + CO + O_2 and NO + CO + O_2 + C_3H_6 reactions over Cu_5Pd/Al_2O_3, Cu/Al_2O_3, and Pd/Al_2O_3 catalysts.

3.3.3 Mechanistic study and DFT calculations

To clarify the nature of the synergistic effect, I conducted a mechanistic study based on kinetic analysis and density functional theory (DFT) calculations. First, the apparent activation energy (E_A) for NO reduction by CO was estimated for the representative catalysts. The corresponding Arrhenius-type plots and the resulting E_A values are shown in Figure 3.8 and Table 3.3, respectively.

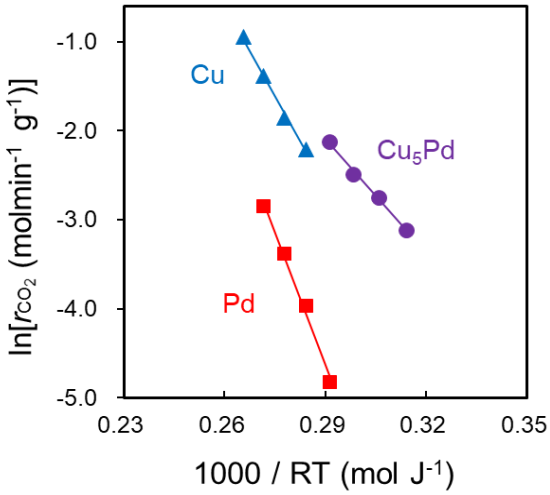

Figure 3.8. Arrhenius-type plots obtained in the NO+CO reaction over Cu_5Pd/Al_2O_3, Cu/Al_2O_3, and Pd/Al_2O_3 catalysts.

Table 3.3. Activation energies estimated from experiments and DFT calculations, along with reaction orders.

	E_A/kJ mol^{-1} (/eV)		
	Pd	Cu	Cu_5Pd
Experiment	99.5	60.8	42.7
DFT: N-O	100.2 [a]	59.8	47.9
DFT: CO + O	100.1 [b]	60.9	34.1
Reaction order			
P_{NO}	-	-0.27	-0.02
P_{CO}	-	1.93	0.44

[a] NO dissociation at the step of Pd(511).[16] [b] CO oxidation on Pd(111).[16]

Cu_5Pd gave an E_A value lower than those of Pd and Cu, which is consistent with the observed catalytic activity. In addition, I estimated the reaction orders for NO and CO pressures (P_{NO} and P_{CO}, respectively) to consider the rate-determining step (RDS). Both Cu and Cu_5Pd showed negative and positive orders for P_{NO} and P_{CO}, respectively (see Table 3.3). Unlike the case for Pd-based catalysts,[49] bond dissociation of N–O has been speculated to occur via $(NO)_2$ dimer formation on Cu surfaces.[50–52] Therefore, in the present study, an extended Langmuir–Hinshelwood model that includes $(NO)_2$ dimer

formation, the subsequent N–O scission (N_2O formation), and N_2O decomposition (N_2 formation) was considered. I solved the rate equation of each step regarded as the RDS by using the overall site balance and equilibrium constants for the other steps.

In most cases, the reaction order for P_{NO} is positive, which is inconsistent with the observed experimental results. Conversely, when the N–O scission of the $(NO)_2$ is considered as from 0 to 2, respectively, in agreement with the experimental the RDS, the orders for P_{NO} and P_{CO} range from -2 to 0 and from 0 to 2, respectively, in agreement with the experimental values. Thus, the kinetic study suggests that the N–O scission was the RDS in NO reduction by CO. Upon incorporation of Pd atoms into pure Cu, the order for P_{NO} becomes less negative, while that for P_{CO} decreases substantially. This result indicates that the strong adsorption of NO inhibits CO adsorption onto Cu, while the latter is enhanced in the presence of Pd. I performed DFT calculations for the relevant elemental steps on pure and Pd-doped Cu surfaces. On the basis of the literature,[53] the step site of the (211) surface was considered the active site for N–O scission (Figure 3.9). The corresponding energy diagrams are shown in Figure 3.10.

NO adsorption was weakened by the addition of Pd, which is consistent with the change in the reaction orders (Table 3.3). Dimerization occurs at the terrace site adjacent to the step site, with a negligible energy barrier. The subsequent N–O scission is triggered by the capture of an oxygen atom by the edge Cu atoms, resulting in the formation of an on-top N_2O with E_A values of 59.8 and 47.9 kJ mol^{-1} for pure and Pd-doped Cu, respectively. The calculated E_A values agree with the experimental values (Table 3.3). The lower E_A for the Pd-doped Cu appears to originate from the destabilized adsorption of the $(NO)_2$ dimer by Pd.

I also considered the CO oxidation process ($CO + O \rightarrow CO_2$), which is necessary for the catalytic cycle (Figure 3.11). The CO + O reaction over pure and Pd-doped Cu(111) surfaces gave E_A values of 60.9 kJ mol^{-1} and 34.1 kJ mol^{-1}, respectively (Table 3.3 and Figure 3.11). These values are very similar to or lower than those for N–O scission, which is consistent with the RDS being the scission of N–O. I also simulated the N_2O decomposition process ($N_2O \rightarrow N_2 + O$) on Cu(211) and (111) surfaces to understand

the intrinsic high N_2 selectivity of Cu (Figure 3.12 and 3.13; see 3.14 for the pictures of the optimized structures).

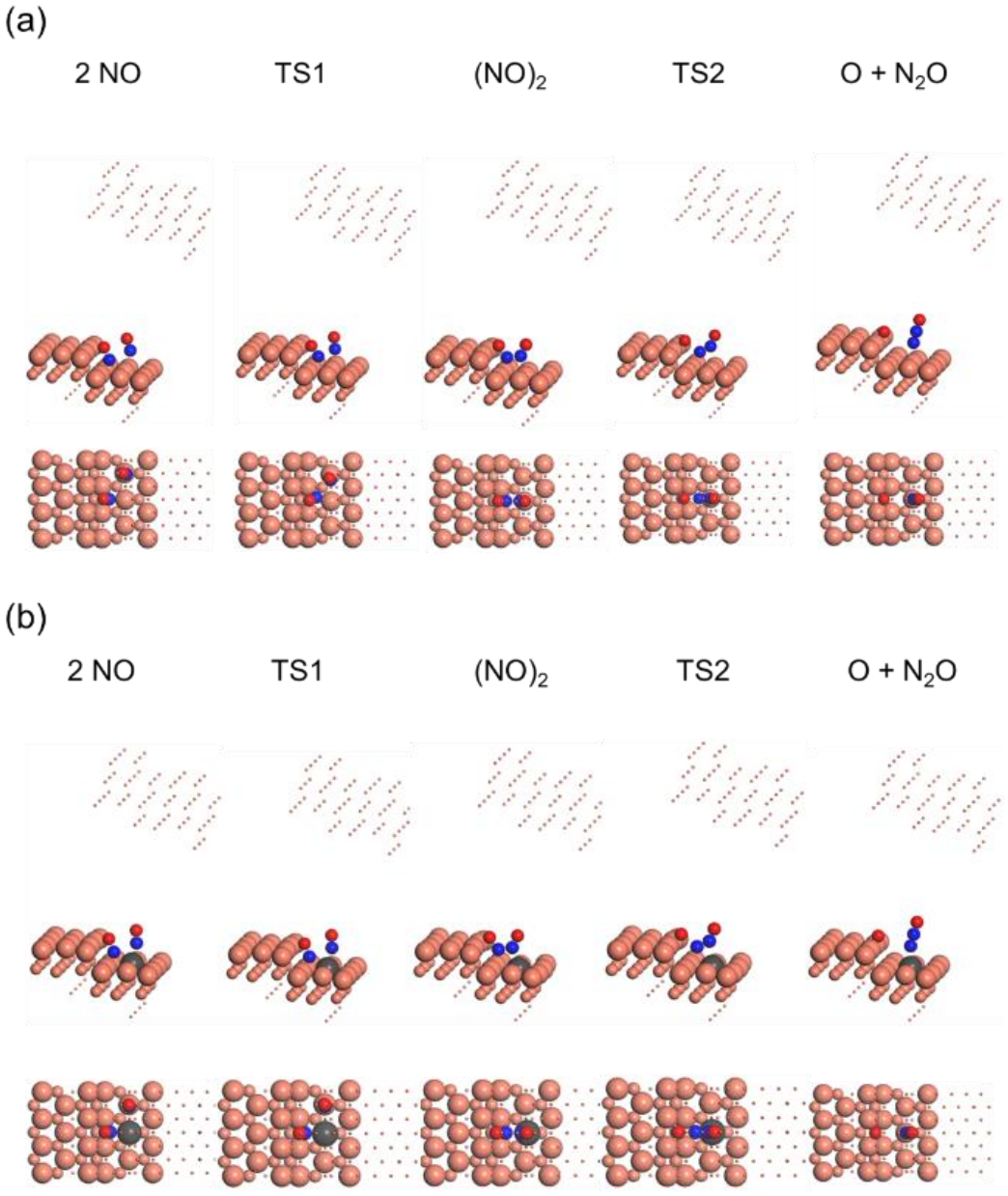

Figure 3.9. Optimized structures of adsorbates and the corresponding transition states during $(NO)_2$ dimer formation and its subsequent decomposition to N_2O and O over (a) Cu(211) and (b) Pd-substituted Cu(211). For clarity, metal atoms in the sub-surface region are shown as small dots.

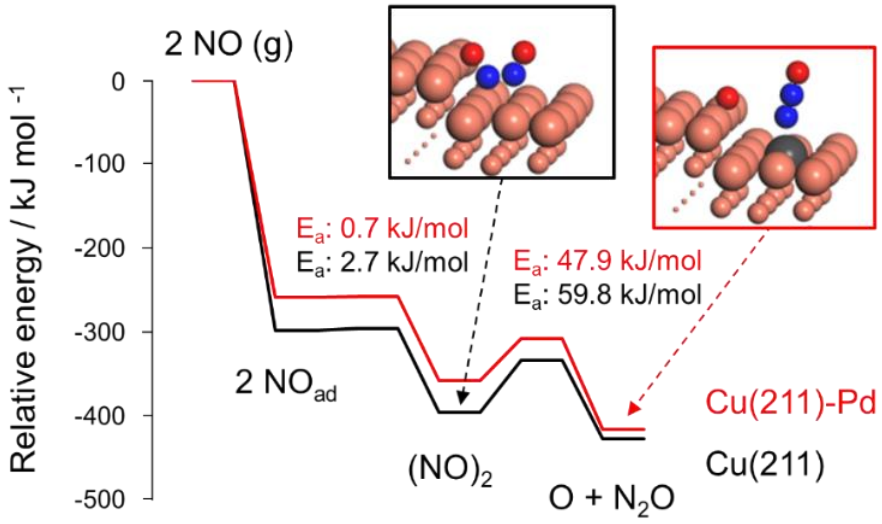

Figure 3.10. Energy diagrams of NO adsorption, dimerization, and the dimer's decomposition over pure and Pd-doped Cu(211) surfaces. The total energy of the slab and free NO was set to zero.

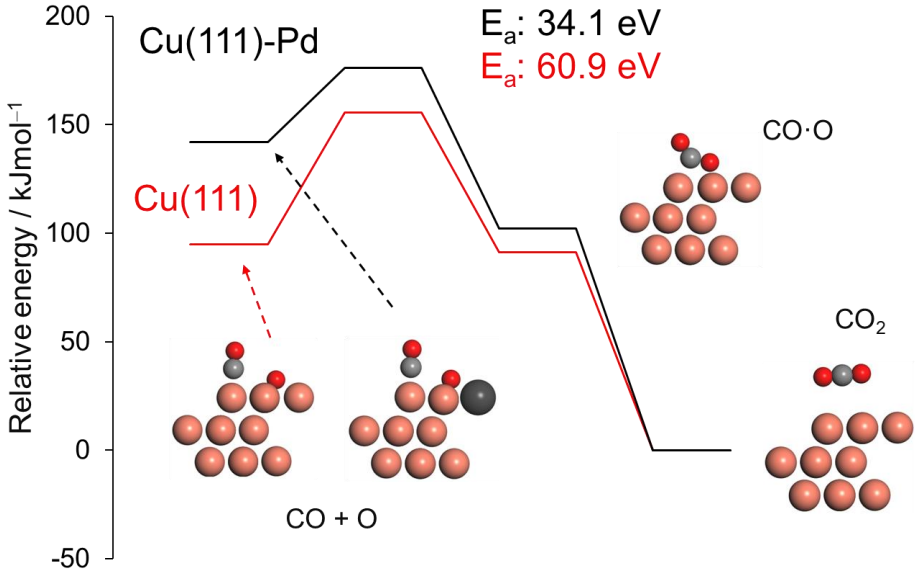

Figure 3.11. Energy diagrams of CO oxidation over Cu(111) and Pd-substituted Cu(111) surfaces. The total energy of the slab plus free CO_2 was set zero. TS search was performed with the intermediate structure (CO·O) as a tentative final state.

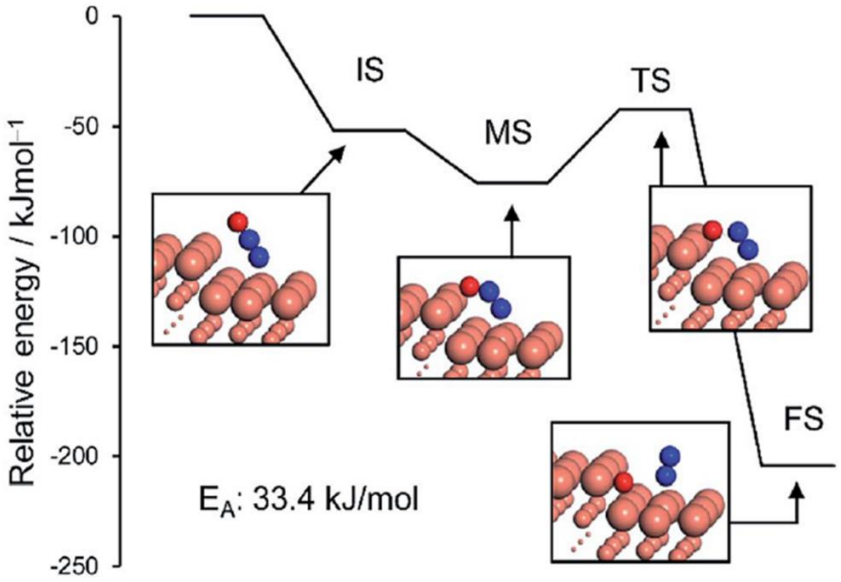

Figure 3.12. Energy diagrams of N_2O bending (initial (IS) to intermediate (MS) states) and its subsequent decomposition to N_2 and O (MS to the final state (FS)) over the Cu(211) surface. The total energy of the slab and free N_2O was set to zero.

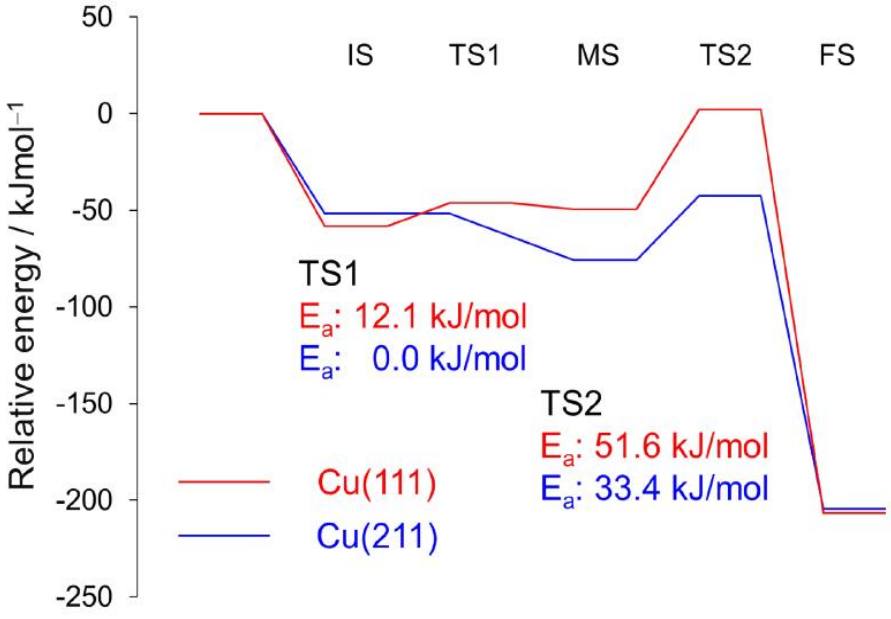

Figure 3.13. Energy diagrams of N_2O bending (IS → MS) and its subsequent decomposition to N_2 and O (MS → FS) over (a) Cu(111) and (b) Cu(211) surfaces. For Cu(211), conversion from IS to MS was barrier-less. The total energy of the slab and free N_2O was set to zero.

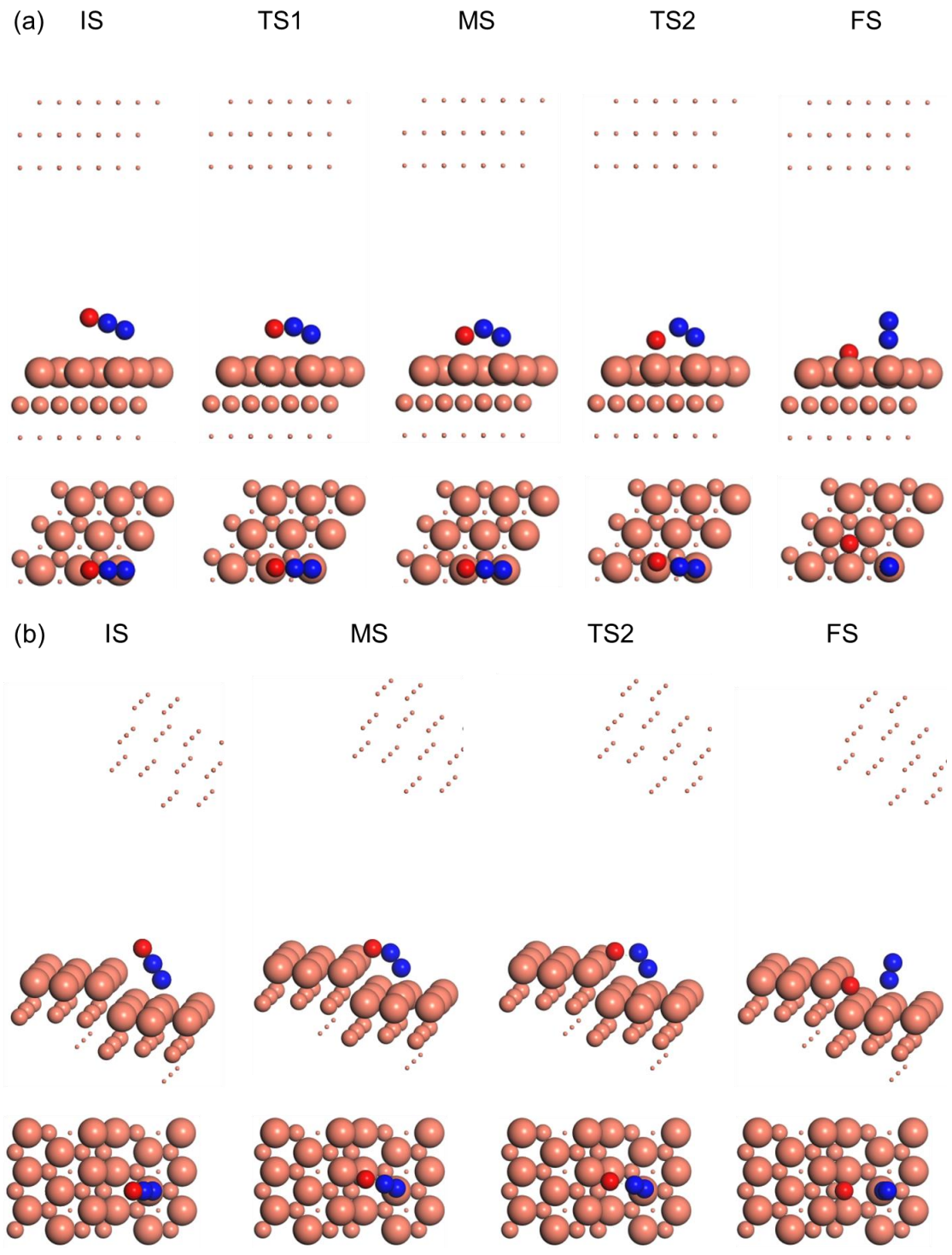

Figure 3.14. Optimized structures of adsorbates (IS, MS, and FS) and the corresponding transition states (TS1 and TS2) during N_2O bending and its subsequent decomposition to N_2 and O over (a) Cu(111) and (b) Cu(211) surfaces. For clarity, metal atoms in the sub-surface region are shown as small dots.

The monodentate linear N_2O was bent to form a bidentate N_2O at the edge site of the Cu(211) plane without an energy barrier. The bidentate N_2O was subsequently decomposed into N_2 and O with a low E_A of 33.4 kJ mol^{-1}, indicating that the N_2O once formed could be smoothly decomposed into N_2 to afford high N_2 selectivity. Although the Cu(111) surface was also active for N_2O decomposition in a similar fashion, the energy barrier was higher than that of Cu(211) (51.6 kJ mol^{-1}, Figure 3.13). Because large Cu–Cu ensembles are present on the surface of the Cu and Cu-rich catalysts (Cu_5Pd and Cu_3Pd), N_2O decomposition could also be enhanced on these catalysts. However, for CuPd, this effect is limited because of the dilution of Cu–Cu ensembles and the increase of Pd–Pd ensembles. Thus, the calculation rationalized the substantial enhancement in catalytic activity on the basis of the formation of the Cu–Pd single-atom alloy and the origin of the excellent selectivity for N_2 formation. The elucidated mechanism differs completely from those proposed for other bimetallic alloy systems. For example, for the Pt–Co system, Sato et al. reported that alloying with Co makes Pt electron-rich, which enhances back donation to adsorbed NO, inducing bond breaking.[13] Therefore, Co likely acts as a promoter for Pt. By contrast, in this system, the isolated Pd acts as an efficient promotor for Cu.

3.4 Conclusion

I prepared a series of $Cu–Pd/Al_2O_3$ catalysts for selective NO reduction at low temperatures. Alloying of Pd with a large amount of Cu (Cu/Pd = 5) isolates Pd and drastically improves both the catalytic activity and N_2 selectivity, affording outstanding catalytic performance. In the NO reduction by CO, NO is completely converted to N_2 even at 175℃, with long-term stability for at least 30 h. The high catalytic performance is also achieved in the presence of O_2 and C_3H_6, where the amount of Pd needed for a comparable performance can be reduced to 1/10, with minimum evolution of N_2O. For Cu/Al_2O_3 and Cu_5Pd/Al_2O_3, the N–O bond scission of the $(NO)_2$ dimer is the RDS in NO reduction by CO. This step is kinetically facilitated by the isolated Pd atoms. N_2O decomposition to N_2 smoothly proceeds on the Cu surface, which contributes to the excellent N_2 selectivity observed for Cu and Cu-rich catalysts. The key to this efficient catalysis is the sufficient isolation of Pd atoms by Cu, highlighting the importance of catalyst design based on single atom alloy structures. The insights gained in this study

provide not only a highly efficient deNO_x system with substantially reduced noble-metal content, but also open a new path for the chemistry of single-atom alloys.

References

1. P. Pacher, J. S. Beckman and L. Liaudet, *Physiol. Rev.*, 2007, **87**, 315–424.
2. B. C. Berks, S. J. Ferguson, J. W. B. Moir and D. J. Richardson, *Biochim. Biophys. Acta, Bioenerg.*, 1995, **1232**, 97–173.
3. F. Rezaei, A. A. Rownaghi, S. Monjezi, R. P. Lively and C. W. Jones, *Energy Fuels*, 2015, **29**, 5467–5486.
4. C. Monn, *Atmos. Environ.*, 2001, **35**, 1–32.
5. J. H. Wang, H. Chen, Z. C. Hu, M. F. Yao and Y. D. Li, *Catal. Rev.*, 2015, **57**, 79–144.
6. J. H. Holles, R. J. Davis, T. M. Murray and J. M. Howe, *J. Catal.*, 2000, **195**, 193–206.
7. A. Srinivasan and C. Depcik, *Catal. Rev.*, 2010, **52**, 462–493.
8. J. Shibata, M. Hashimoto, K. Shimizu, H. Yoshida, T. Hattori and A. Satsuma, *J. Phys. Chem. B*, 2004, **108**, 18327–18335.
9. W. Z. An, Q. L. Zhang, K. T. Chuang and A. R. Sanger, *Ind. Eng. Chem. Res.*, 2002, **41**, 27–31.
10. R. Burch, J. P. Breen and F. C. Meunier, *Appl. Catal., B*, 2002, **39**, 283–303.
11. V. Tomasic, *Catal. Today*, 2007, **119**, 106–113.
12. S. Hosokawa, K. Matsuki, K. Tamaru, Y. Oshino, H. Aritani, H. Asakura, K. Teramura and T. Tanaka, *Mol. Catal.*, 2017, **442**, 74–82.
13. K. Sato, A. Ito, H. Tomonaga, H. Kanematsu, Y. Wada, H. Asakura, S. Hosokawa, T. Tanaka, T. Toriyama and T. Yamamoto, *ChemPlusChem*, 2019.
14. T. Tanabe, T. Imai, T. Tokunaga, S. Arai, Y. Yamamoto, S. Ueda, G. V. Ramesh, S. Nagao, H. Hirata, S. Matsumoto, T. Fujita and H. Abe, *Chem. Sci.*, 2017, **8**, 3374–3378.
15. T. Imai, S. Ueda, S. Nagao, H. Hirata, K. R. Deepthi and H. Abe, *RSC Adv.*, 2017, **7**, 9628–9631.
16. J. Jeon, K. Kon, T. Toyao, K. Shimizu and S. Furukawa, *Chem. Sci.*, 2019, **10**, 4148–4162.
17. M. V. Twigg, *Appl. Catal., B*, 2007, **70**, 2–15.
18. P. Granger, C. Dujardin, J. F. Paul and G. Leclercq, *J. Mol. Catal. A: Chem.*, 2005, **228**, 241–253.
19. G. Kyriakou, M. B. Boucher, A. D. Jewell, E. A. Lewis, T. J. Lawton, A. E. Baber, H. L. Tierney, M. Flytzani- Stephanopoulos and E. C. H. Sykes, *Science*, 2012, **335**, 1209–1212.

20. A. Wang, J. Li and T. Zhang, *Nat. Rev. Chem.*, 2018, **2**, 65.
21. M. J. H¨ulsey, J. Zhang and N. Yan, *Adv. Mater.*, 2018, **30**, 1802304.
22. M. T. Greiner, T. E. Jones, S. Beeg, L. Zwiener, M. Scherzer, F. Girgsdies, S. Piccinin, .M. Armbruster, A. Knop-Gericke and R. Schlogl, *Nat. Chem.*, 2018, **10**, 1008–1015.
23. P. Aich, H. J. Wei, B. Basan, A. J. Kropf, N. M. Schweitzer, C. L. Marshall, J. T. Miller and R. Meyer, *J. Phys. Chem. C*, 2015, **119**, 18140–18148.
24. G. X. Pei, X. Y. Liu, A. Q. Wang, A. F. Lee, M. A. Isaacs, L. Li, X. L. Pan, X. F. Yang, X. D. Wang, Z. J. Tai, K. Wilson and T. Zhang, *ACS Catal.*, 2015, **5**, 3717–3725.
25. X. X. Cao, A. Mirjalili, J. Wheeler, W. Xie and B. W. L. Jang, *Front. Chem. Sci. Eng.*, 2015, **9**, 442–449.
26. F. R. Lucci, J. L. Liu, M. D. Marcinkowski, M. Yang, L. F. Allard, M. Flytzani-Stephanopoulos and E. C. H. Sykes, *Nat. Commun.*, 2015, **6**, 8550.
27. J. L. Liu, J. J. Shan, F. R. Lucci, S. F. Cao, E. C. H. Sykes and M. Flytzani-Stephanopoulos, *Catal. Sci. Technol.*, 2017, **7**, 4276–4284.
28. M. D. Marcinkowski, J. L. Liu, C. J. Murphy, M. L. Liriano, N. A. Wasio, F. R. Lucci, M. Flytzani-Stephanopoulos and E. C. H. Sykes, *ACS Catal.*, 2017, **7**, 413–420.
29. H. Miura, K. Endo, R. Ogawa and T. Shishido, *ACS Catal.*, 2017, **7**, 1543–1553.
30. P. Bera, K. C. Patil and M. S. Hegde, *Phys. Chem. Chem. Phys.*, 2000, **2**, 3715–3719.
31. P. Miguel, P. Granger, N. Jagtap, S. Umbarkar, M. Dongare and C. Dujardin, *J. Mol. Catal. A: Chem.*, 2010, **322**, 90–97.
32. H. Iwamoto, S. Kameoka, Y. Xu, C. Nishimura and A. P. Tsai, *J. Phys. Chem. Solids*, 2019, **125**, 64–73.
33. M. D. Segall, P. J. D. Lindan, M. J. Probert, C. J. Pickard, P. J. Hasnip, S. J. Clark and M. C. Payne, *J. Phys.: Condens. Matter*, 2002, **14**, 2717–2744.
34. D. Vanderbilt, *Phys. Rev. B: Condens. Matter Mater. Phys.*, 1990, **41**, 7892–7895.
35. J. P. Perdew, K. Burke and M. Ernzerhof, *Phys. Rev. Lett.*, 1996, **77**, 3865–3868.
36. A. Tkatchenko and M. Scheffler, *Phys. Rev. Lett.*, 2009, **102**, 073005.
37. H. J. Monkhorst and J. D. Pack, *Phys. Rev. B*, 1976, **13**, 5188– 5192.
38. N. Govind, M. Petersen, G. Fitzgerald, D. King-Smith and J. Andzelm, *Comput. Mater. Sci.*, 2003, **28**, 250–258.
39. T. A. Halgren and W. N. Lipscomb, *Chem. Phys. Lett.*, 1977, **49**, 225–232.
40. W. K. Kuhn, J. Szanyi and D. W. Goodman, *Surf. Sci.*, 1992, **274**, L611–L618.
41. O. Dulaurent, X. Courtois, V. Perrichon and D. Bianchi, *J. Phys. Chem. B*, 2000, **104**, 6001–6011.
42. S. Zhou, B. Varughese, B. Eichhorn, G. Jackson and K. McIlwrath, *Angew. Chem., Int.*

Ed., 2005, **44**, 4539–4543.

43. M. Fern´andez-Garcia, A. Martinez-Arias, C. Belver, J. Anderson, J. Conesa and J. Soria, J. Catal., 2000, 190, 387–395.
44. F. Gao, Y. Wang and D. W. Goodman, *J. Catal.*, 2009, **268**, 115–121.
45. T. Hirano, Y. Ozawa, T. Sekido, T. Ogino, T. Miyao and S. Naito, *Catal. Commun.*, 2007, **8**, 1249–1254.
46. A. Hungrıa, A. Iglesias-Juez, A. Martınez-Arias, M. Fern´andez-Garcıa, J. Anderson, J. Conesa and J. Soria, *J. Catal.*, 2002, **206**, 281–294.
47. T. Komatsu, H. Kobayashi, K. Kusada, Y. Kubota, M. Takata, T. Yamamoto, S. Matsumura, K. Sato, K. Nagaoka and H. Kitagawa, *Chem.–Eur. J.*, 2017, **23**, 57–60.
48. A. Hungr´ıa, M. Fern´andez-Garc´ıa, J. Anderson and A. Mart´ınez-Arias, *J. Catal.*, 2005, **235**, 262–271.
49. D. R. Rainer, S. M. Vesecky, M. Koranne, W. S. Oh and D. W. Goodman, *J. Catal.*, 1997, **167**, 234–241.
50. W. Brown, R. Sharma, D. King and S. Haq, *J. Phys. Chem.*, 1996, **100**, 12559–12568.
51. A. Bogicevic and K. Hass, *Surf. Sci.*, 2002, **506**, L237–L242.
52. N. Takagi, K. Ishimura, H. Miura, T. Shishido, R. Fukuda, M. Ehara and S. Sakaki, *ACS Omega*, 2019, **4**, 2596–2609.
53. R. Burch, S. Daniells and P. Hu, *J. Chem. Phys.*, 2004, **121**, 2737–2745.

Chapter 4

Highly Efficient deNO_x System using Pseudo-Binary Alloy as Catalyst: Effective NO Reduction even in the Excessive Lean Conditions

4.1 Introduction

The combustion of fossil fuel by air in automotive engines, power plants, and other industrial processes produces exhaust gases which contain nitrogen oxides (NO_x), carbon monoxide (CO), and unburned non-methane hydrocarbons (HCs) as air pollutants.[1] Among the exhaust gases, NO_x is major air pollution, which induces many environmental problems, e.g., photochemical smog, acid rain, and global warming. NO_x removal has long been studied as an indispensable process for exhaust gas purification. To solve this exhaust gas problem, researcher has been focused on some clean technologies to protect the global environment.[2]

As a part of deNO_x technologies, NO_x Storage and Reduction (NSR)[3–7], Selective Catalytic Reduction (SCR)[5,8–10], and the combination thereof were developed. Among them, the exhaust gas purification catalyst for the gasoline engine is known as a three-way catalyst (TWC) and is indispensable for removal of CO, hydrocarbons, and NO_x generated as exhaust gases from internal combustion engines.[11–15] Figure 4.1 shows the air-to-fuel ratio window of TWC with respect to the concentration of exhaust gases.[15–18] At the outside of the window, conversion of reductants (CO, HC) and NO_x become lower under rich and lean conditions, respectively. In lean conditions, excess oxygen is included in the exhaust gas, which causes preferential oxidation of the reductants. Consequently, the performance of the catalytic reduction of NO_x ($NO+NO_2$) strongly depends on oxygen concentration.[18,19] Recently developed lean NO_x Trap (LNT) catalysts use Ba, Sr, or K, etc. as a trapping agent for NO_x.[3,4] However, it is desired to develop a deNO_x catalyst that works well even under lean conditions.

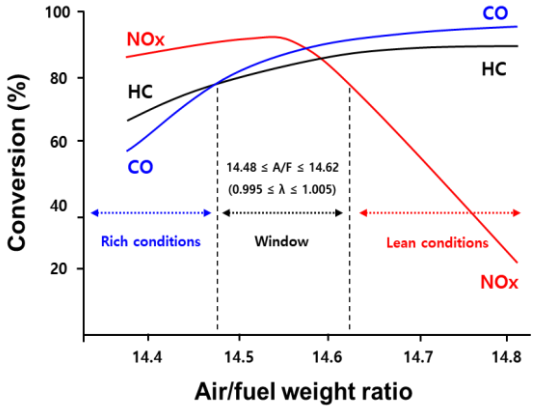

Figure 4.1. Air/fuel (A/F) ratio curve of TWCs. The ratio is far from the operating window results in a significant loss of catalytic performance.

Nowadays, ultra-high fuel efficiency and environment-friendly technology have been developed in the automobile industry. The application of ultra-high efficiency fuel economy engine technology to improve the fuel efficiency of the vehicle lowers the exhaust gas emission temperature and decreases the activity of the purification catalyst optimized for the existing system.[20] This indicates that the existing purification systems cannot satisfy the recent tight environmental regulations. Therefore, it is desired to develop a new catalytic purification system suitable for the latest high fuel efficiency engine system. In the case of the next generation three-way catalyst technology, it is necessary to solve the above-mentioned problem: low catalytic activity at low temperatures and low NO_x conversion to N_2 under lean conditions.

Intermetallic compounds, which are ordered alloys typically composed of metal elements that are separated each other in the periodic table, can be attractive inorganic materials for sophisticated catalyst design.[21] An appropriate combination of metal elements would provide significantly modified electronic and geometric structures that are suitable for efficient NO reduction even under severe conditions. As shown in Chapter 2, a highly efficient NO reduction system at the low-temperature region was developed using the catalyst design based on pseudo-binary alloys.[22,23] In this study, this catalyst design was applied to solve the issue on the deNO_x catalysis under lean conditions. A series of PGM catalysts including pseudo-binary alloys by using alumina and ceria as supports and tested them in NO–CO–O_2 and NO–CO–O_2–C_3H_6 reactions. The effect of alloying on improved deNO_x performance under lean conditions was deeply investigated using several characterization techniques.

4.2 Experimental section

4.2.1 Catalyst preparation

Boehmite (γ-AlOOH) was supplied by SASOL chemicals. γ-Al_2O_3 was prepared by calcination of boehmite at 900℃ for 3 h. CeO_2 was supplied by Daiichi Kigenso Kagaku Kogyo. Ltd. and no calcination was done before use. A series of monometallic catalysts (M/support, M = Pd, Pt and Rh, support = Al_2O_3, CeO_2) were prepared by an impregnation method using an excess amount of water (ca. 25 ml of ion-exchanged water per g of support). The support (γ-Al_2O_3, CeO_2) was added to a vigorously stirred mixed aqueous solution of $Pd(NH_3)_2(NO_2)_2$ (Kojima Chemicals, 4.765 wt% in HNO_3), $Rh(NO_3)_3$

(Furuya Metal Co. Ltd., 4.87 wt% Rh), and $Pt(NH_3)_2(NO_3)_2$ (Furuya Metal Co. Ltd., 4.96 wt% of Pt). Bimetallic catalysts (PdN/support, N =Pt, In) were prepared by a co-impregnation method using an excess amount of water (ca. 25 ml of ion-exchanged water per g of support). The support (γ-Al_2O_3, CeO_2) was added to a vigorously stirred mixed aqueous solution of $Pd(NH_3)_2(NO_2)_2$ and second metal salt ($In(NO_3)_3 \cdot nH_2O$ (Kanto, 99%), $Cu(NO_3)_2 \cdot 3H_2O$ (Sigma-Aldrich), or $Pt(NH_3)_2(NO_3)_2$) followed by stirring for 3 h. The mixture was dried under a reduced pressure at 50℃, followed by reduction under flowing H_2 (30 ml min^{-1}) at 400℃ for 1 h. The metal loading and the atomic ratio of M/In were adjusted to 0.5 or 3.0 wt% and 1 (M = Pd). For trimetallic catalysts, the metal loading of Pd was also adjusted to 0.5 or 3.0 wt% and the atomic ratio of Pd/(In + Cu) was one. Substituting a part of Pd in PdIn with Pt, $(Pd_{0.5}Pt_{0.5})$In catalysts was prepared with the metal loading of Pd of 0.25 wt% or 1.5 wt% and the atomic ratio of (Pd + Pt)/In equal to one. The impregnated catalysts were reduced under flowing H_2 at 400℃ for 1 h**.**

4.2.2 Catalytic reaction

The catalyst (0.09 g) diluted with quartz sand (1.91 g, Miyazaki chemical 99.9%) was treated under flowing hydrogen (50 ml min^{-1}) at 400℃ for 0.5 h prior to the catalytic reactions. The gas-phase was analyzed using an online thermal conductivity detection gas chromatography (Shimazu GC-8A, column: SHINWA SHINCARBON ST) located downstream. In the quasi-static test, NO–CO–O_2 and NO–CO–O_2–C_3H_6 reactions were performed under the following condition: NO (5,000 ppm), CO (10,000 ppm), O_2 (0-10,000 ppm), He (balance) with a total flow rate of 96 ml min^{-1} (GHSV = 40,000 h^{-1}), and NO (5,000 ppm), CO (5,000 ppm), O_2 (0-11,250 ppm), C_3H_6 (1,250 ppm), and He (balance) with a total flow rate of 96 ml·min^{-1} (GHSV = 40,000 h^{-1}), respectively.

$$2CO + 1NO + 1/2O_2 \rightarrow 2CO_2 + 1/2N_2$$

$$C_3H_6 + 4\,NO + 4\,CO + 9/2\,O_2 \rightarrow 2\,N_2 + 7\,CO_2 + 3\,H_2O$$

For better understanding, the lambda (λ) parameter, as defined below, was introduced as an indicator of the oxygen concentration or stoichiometric balance, where $[X]_y$ is the

concentration of *X* at the actual (y=a) or stoichiometric condition (y=s)

$$\lambda = ([NO]_a + [CO]_a + 2[O_2]_a)/([NO]_s + [CO]_s + 2[O_2]_s)$$

During a lean-rich cycle reaction test, the catalyst was treated under the same conditions. the model exhaust gas was repeatedly changed from a lean condition (λ =1.25; NO 5,000 ppm, CO 10,000 ppm, O_2 5,000 ppm and He balance, 96 ml·min^{-1}) to a rich condition (λ =0.75; NO 5,000 ppm, CO 10,000 ppm, O_2 0 ppm and He balance, 96 ml·min^{-1}) every 0.5 h. The gas switch was repeated five times. The concentration of the outlet gas was quantified about every 0.5 h.

4.2.3 Characterization

High angle annular dark-field scanning TEM microscopy (HAADF-STEM) was carried out using a JEOL JEM-ARM200 M microscope equipped with an energy dispersive X-ray (EDX) analyzer (EX24221M1G5T). The STEM analysis was performed at an accelerating voltage of 200 kV. To prepare the TEM specimen, all samples were sonicated in ethanol and then dispersed on a Mo grid supported by an ultrathin carbon film.

CO pulse chemisorption was performed using BELCAT II (Microtrac BEL) to estimate the Pd dispersion of the prepared catalysts. Prior to chemisorption, the catalyst was pretreated under a 5% H_2/Ar flow (40 mL min^{-1}) at 400°C for 0.5 h. After the reduction pretreatment, He was introduced at the same temperature for 10 min to remove the chemisorbed hydrogen, followed by cooling to room temperature. A 10% CO/He pulse was introduced into the reactor, and the supplied CO flow was quantified downstream by a thermal conductivity detector. For example, Pd dispersion for Pd/Al_2O_3 (Pd: 3 wt%) was estimated as 13.6%.

The Fourier-transformed infrared (FT-IR) spectra of adsorbed CO were obtained with a JASCO FTIR-4200 spectrometer equipped with an MCT detector in the transmission mode (resolution 4 cm^{-1}). The samples were prepared as self-supporting wafers (2.0 cm diameter. < 0.5 mm thickness) and were placed inside an IR cell with CaF_2 windows. A custom glass manifold was connected to the cell to control the gas for pretreatment and the amount of CO introduced. The cell was first purged with He, and

the sample was reduced under flowing hydrogen (50 ml min^{-1}) at 400℃ for 0.5 h. After reduction, the wafer was cooled to 40℃ under He flow. The wafer was exposed to CO (0.5%) and He (balance) with a total flow rate of 50 ml min^{-1} for 20 min. After the CO exposure, He was followed for 5 min to remove the gas phase and weakly adsorbed CO, followed by IR spectra measurements.

4.3. Results and discussion

4.3.1 Metallic catalysts of Pd-Pt pseudo-binary system

The monometallic Pd (3 wt% or 0.5wt%) and Pt (3 wt% or 0.5 wt%) and the bimetallic $Pd_{0.5}Pt_{0.5}$ (Pd: 1.5 wt% or 0.25 wt%, Pd/Pt = 1) and PdIn (Pd: 3 wt% or 0.5 wt%, Pd/In = 1) and the trimetallic $(Pd_{0.5}Pt_{0.5})In$ (Pd: 1.5 wt% or 0.25 wt%, (Pd+Pt)/In = 1) catalysts were prepared using γ-Al_2O_3 as a support by co-impregnation method. X-ray diffraction (XRD) patterns of the prepared catalysts revealed that Pd-Pt solid-solution alloy phases with bimetallic compositions similar to the metal ratio in the feed were formed (Table 4.1 and Figure 4.1).

Table 4.1. Detailed information on the catalyst prepared in this study.

	Pd	Pt	$Pd_{0.5}Pt_{0.5}$	PdIn	$(Pd_{0.5}Pt_{0.5})In$
Pd loading (wt%)	3 (0.5)	0	1.5 (0.25)	3 (0.5)	1.5 (0.25)
Pt loading (wt%)	0	3 (0.5)	2.7 (0.45)	0	2.7 (0.45)
In loading (wt%)	0	0	0	11.5	11.5
Pd fraction in the catalysts	1.0	0.0	0.50	0.5	0.25
Pd fraction in particle	1.0	0.0	0.47	0.5	-
Metal dispersion (%)	13.6 (71.8)[b]	38.4 (87.3)[b]	25.1 (34.8)[b]	12.1 (45.9)[b]	31.1 (13.6)[b]
Crystallite size/nm[a]	7.6	5.5	7.3	6.6 (7.2)[c]	(3.6)[c]

[a] Estimated from Scherrer's equation using a Scherrer constant of 0.477 for the area-weighted mean diameter. [b] Dispersion of the low loading amount catalyst. [c] Area-weighted means diameter obtained from the TEM image.

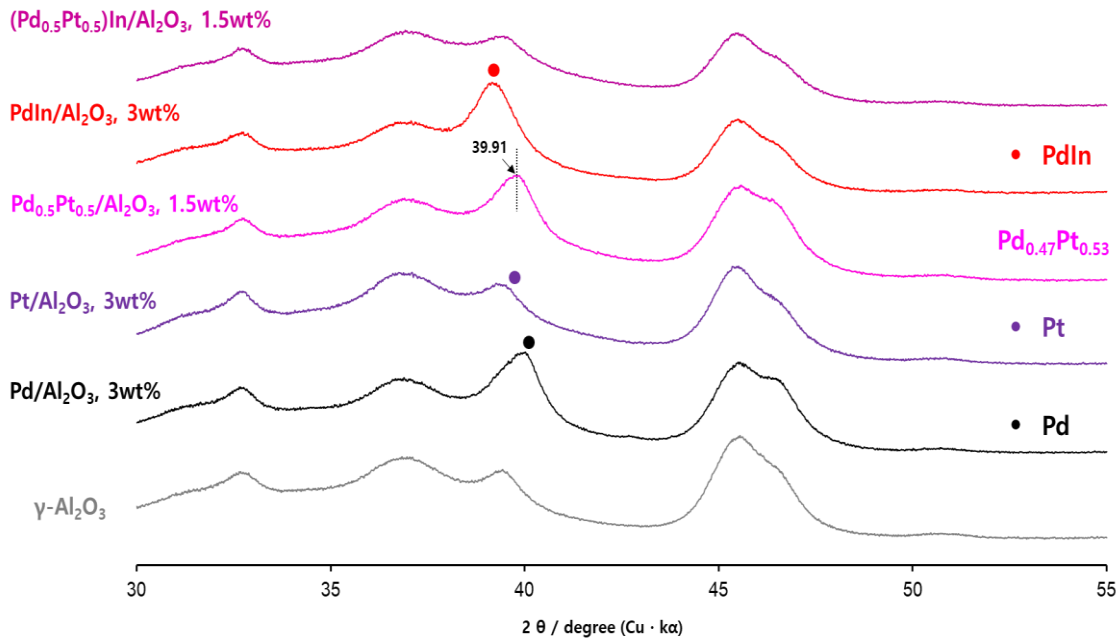

Figure 4.1. XRD patterns of Pd/Al_2O_3, Pt/Al_2O_3, Pd–Pt/Al_2O_3, $PdIn/Al_2O_3$ and (Pd–Pt)In/Al_2O_3. The Pd–Pt solid-solution alloy phase with a bimetallic composition close to that of the feed ratio was formed: Pd/Pt = 1, $Pd_{0.47}Pt_{0.53}$. The diffraction peak intensity changes depending on the metal loadings as summarized in Table 4.1.

The crystallite sizes estimated using Scherrer's equation were 5-7 nm for catalysts showing diffraction peaks other than those of alumina support. For Pt/Al_2O_3 and (Pd–Pt)In/Al_2O_3, there is no peak assignable to metallic phases, suggesting that the formed nanoparticles are too small to be detected by XRD (< 3 nm). Therefore, I performed a HAADF-STEM analysis for the structural analysis of $(Pd_{0.5}Pt_{0.5})In$ the tri-metallic catalyst. Figure 4.2a shows the HAADF-STEM image of (Pd$_{0.5}$Pt$_{0.5}$)In/Al_2O_3. The EDX mapping for some nanoparticles showed that Pd, Pt and In were homogeneously dispersed and constituted the nanoparticles (Figure 4.2b-d). A relatively narrow size distribution between 2 and 5 nm with an area-weighted mean diameter of 3.6 nm was obtained (Figure 4.2e), which is consistent with the result of XRD. A high-resolution image of a single nanoparticle displayed the atomic arrangement of a CsCl-type crystal viewed along the [111] direction with 2.30 Å of the interplanar distance of {110} planes (Figure 4.2f). The observed interplanar distance is consistent with the corresponding theoretical value for (Pd$_{0.5}$Pt$_{0.5}$)In estimated by applying Vegard's law on the basis of their atomic radii and ratio (Pd: 1.373 Å, Pt: 1.385

Å, In: 1.660 Å, 1:1:2, Figure 3)[26]. Moreover, the presence of Pt was also indicated as bright spots (high Z contrast) in Figure 4.2f.

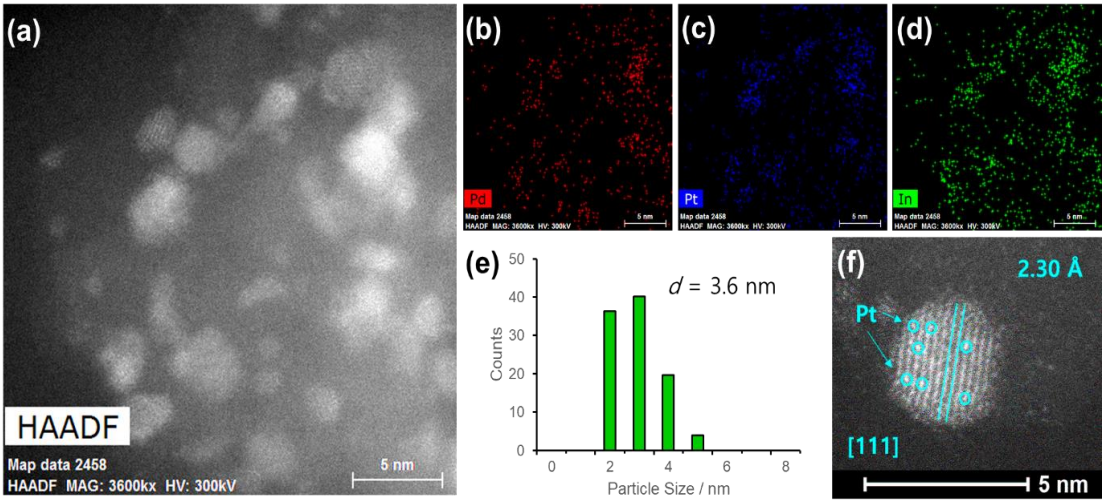

Figure 4.2. (a) HAADF-STEM image of $(Pd_{0.5}Pt_{0.5})In/Al_2O_3$ and elemental maps of (b) Pd, (c) Pt, and (d) In acquired using EDX. (e) the size distribution of the nanoparticles. (f) High-resolution STEM image of a nanoparticle.

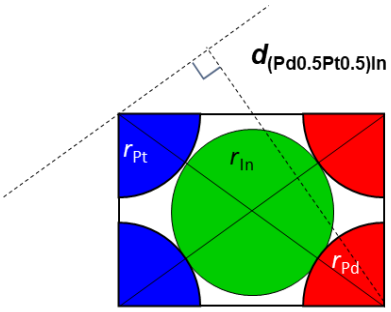

$r_{Pd0.5Pt0.5} + r_{In}$ = (1.373 x 0.5 + 1.385 x 0.5) + 1.66

= 3.039

(0.20 % expansion)

Figure 4.3. Estimation of the lattice constant using Vegard's law with each atomic size and ratio (Pd: 1.373 Å, Pt: 1.385 Å, In: 1.660 Å, 1:1:2) at (110) plane.

FT-IR analysis was also performed for the Pd-Pt based catalysts by using CO adsorption to obtain information about the electronic and geometric environment at the surface (Figure 4.4). Pd/Al_2O_3 showed three different features assigned to the stretching vibration of CO adsorbed on top (2,086 cm^{-1}), bridge (~1,950 cm^{-1}), and threefold hollow (~1,860 cm^{-1}) sites of Pd.[27] For Pt/Al_2O_3, the corresponding three features were observed at 2,068 cm^{-1} (top), ~1,825 cm^{-1} (bridge), and ~1790 cm^{-1} (hollow).[28] For $PdIn/Al_2O_3$, the peak position of linear CO was red-shifted (2,068 cm^{-1}) and the peak corresponding to the bridge CO almost vanished. This indicates that the (1) Pd in PdIn is electron-enriched by In, the (2) Pd–Pd ensembles are completely diluted by In, and (3) the catalyst surface is also of intermetallic PdIn.[29] For $Pd_{0.5}Pt_{0.5}/Al_2O_3$, the peak position of linear CO (2,055 cm^{-1}) and bridge (1,955 cm^{-1}) were also red-shifted.[30] $(Pd_{0.5}Pt_{0.5})In/Al_2O_3$ showed a peak feature similar to that of PdIn, whereas two different peaks for linear CO were observed. These could be assigned to linear CO adsorbed on Pt and Pd. Note that peaks assignable to multifold CO disappeared, indicating the formation of intermetallic surface and consistent with the corresponding pseudo-binary alloy structure (Figure 4.4c). If Pt is substituted exclusively with In such as Pd_2Pt or Pt_2Pd hollow sites are allowed at (110) surface (Figure 4.4b), probably resulting in the appearance of threefold CO. Thus, the FT-IR study supported the formation of the pseudo-binary alloy structure at the catalyst surface.

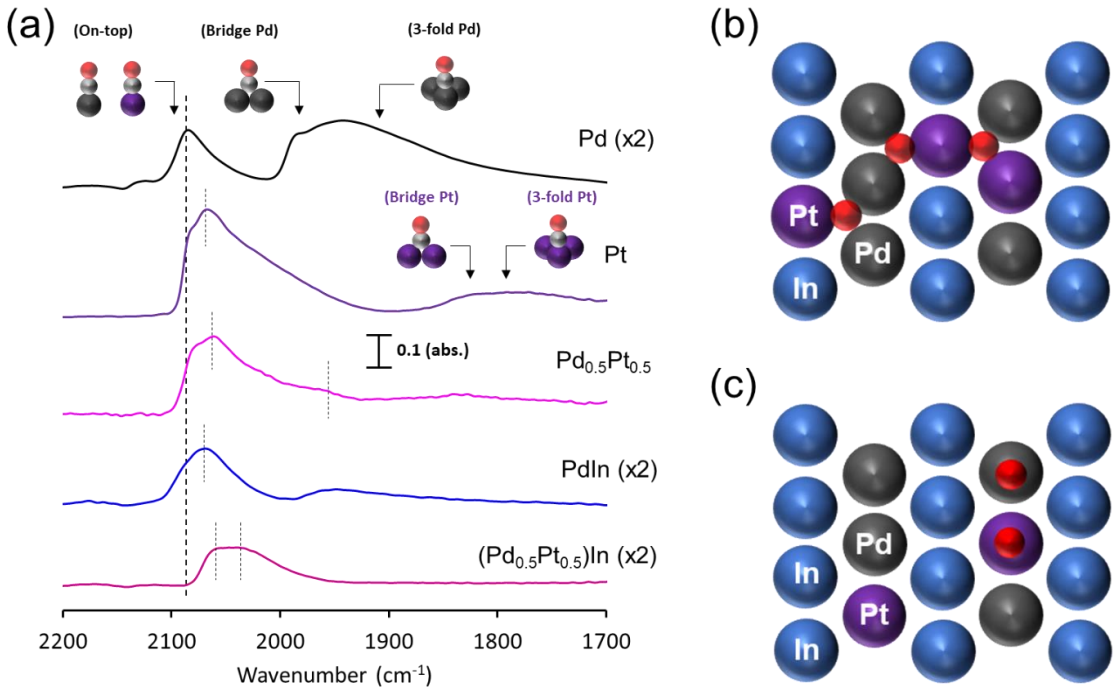

Figure 4.4. (a) FT-IR spectra of CO adsorbed on Pd/Al_2O_3, Pt/Al_2O_3, $Pd_{0.5}Pt_{0.5}/Al_2O_3$, $PdIn/Al_2O_3$ and $(Pd_{0.5}Pt_{0.5})In/Al_2O_3$ (Pd:Pt:In = 1:1:2) catalysts. The atomic arrangement of the most stable (110) surface of $(Pd_{0.5}Pt_{0.5})In$ assuming (b) In-Pt and (c) Pd-Pt replacement. Pd_2Pt and Pt_2Pd hollow sites are formed in (b).

4.3.2 NO reduction by CO under excessive O_2

I then tested the catalytic performance of monometallic PGM (M/Al_2O_3; M = Pd, Pt, and Rh; M = 0.5 wt%) and Pd based alloy catalysts supported on Al_2O_3 in NO–CO–O_2 reaction. Figure 4.5 shows the oxygen concentration dependences of each catalyst on NO conversion to N_2. Note that a harsh condition (NO = 5,000 ppm, CO = 10,000 ppm, O_2 = 0-10,000 ppm, GHSV = 40,000 h^{-1}) was employed so that the difference in catalytic performances became obvious. As expected, N_2 yield significantly decreased when going to lean conditions ($1.0 < \lambda$). At 250°C (Figure 4.5a), Pd, Pt, $Pd(In_{0.33}Cu_{0.67})$ and $(Pd_{0.5}Pt_{0.5})In$ showed similar N_2 yields (≤ 20%). PdIn showed a high N_2 yield (≤ 40%) and similar than that of Rh. For PdIn and Rh catalysts, the reduction performance of NO was maintained up to the oxygen concentration of 5,000 ppm (λ=1.25). N_2 yield monotonously increased as the reaction temperature increased (Figure 4.5b, c) in the rich region ($\lambda < 1.0$). At 300°C (Figure 4.5b), PdIn showed good catalytic activity similar to that of Rh. However, a decrease in NO conversion was more clearly observed

under higher temperature lean conditions (1.0 < λ) due to preferential oxidation of reducing agent CO with excess O_2 (Figure 4.6). In contrast, interestingly, $(Pd_{0.5}Pt_{0.5})In$ catalyst exhibited a high N_2 yield than other catalysts at extreme lean condition (λ = 1.5). This trend was observed at 300℃ (Figure 4.5b) and clearly distinguished at 350℃ (Figure 4.5c). Unfortunately, however, $(Pd_{0.5}Pt_{0.5})In$ did not exhibit sufficient performance in rich conditions. therefore, if the performance of $(Pd_{0.5}Pt_{0.5})In/Al_2O_3$ catalyst in rich condition can be improved, the purpose of this study would be achieved.

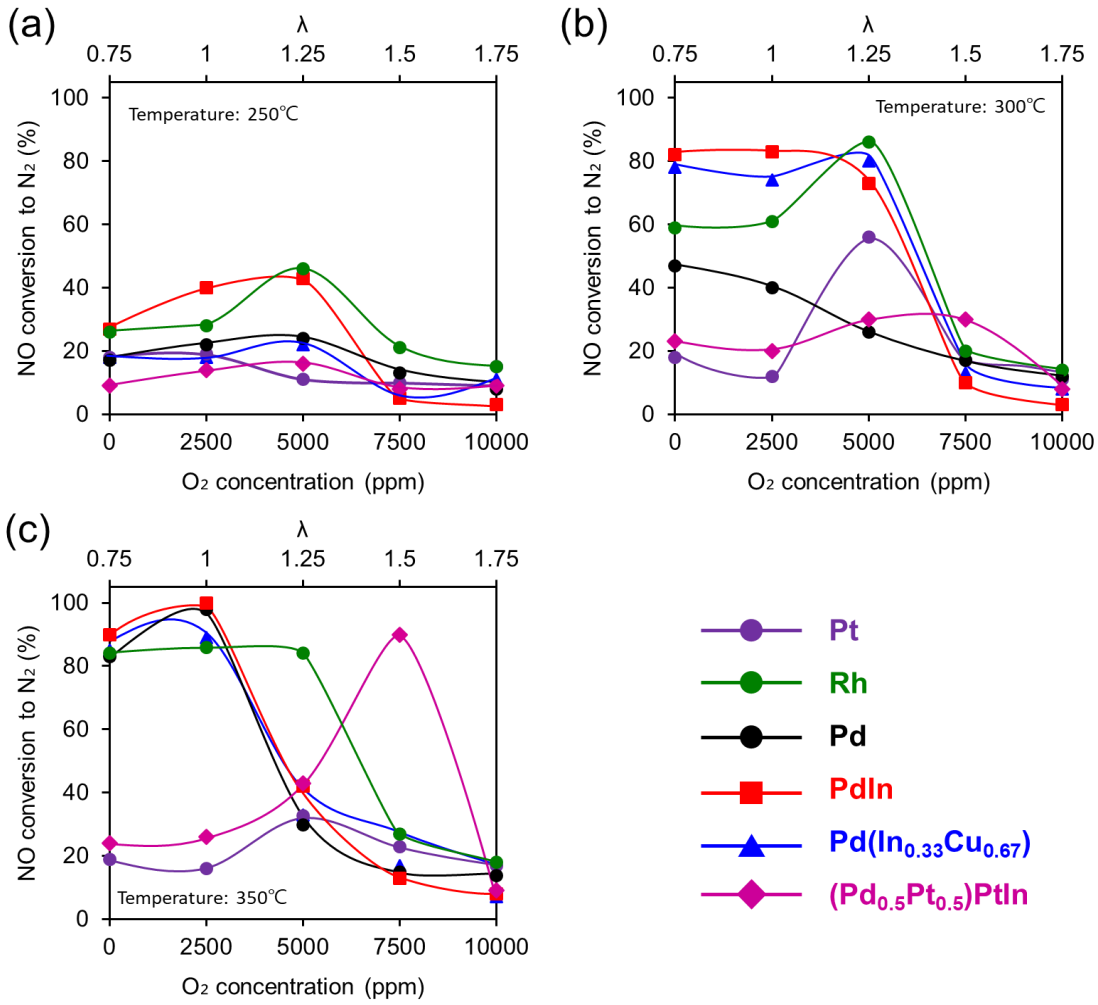

Figure 4.5. NO conversion to N_2 at (a) 250℃, (b) 300℃ and (c) 350℃ in NO–CO–O_2 reaction using Al_2O_3-supported catalysts.

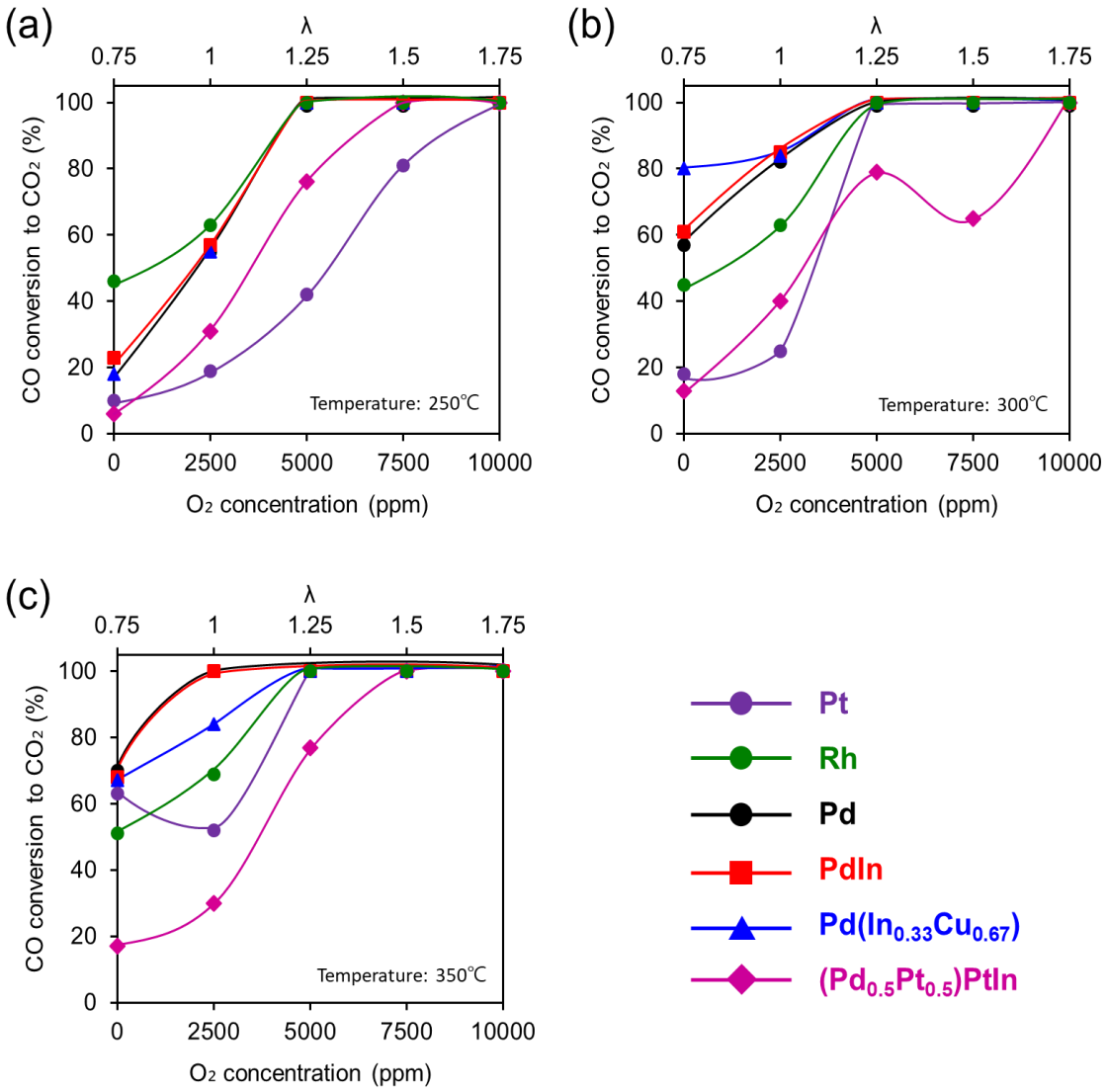

Figure 4.6. CO conversion to CO_2 at (a) 250℃, (b) 300℃ and (c) 350℃ in NO–CO–O_2 reaction using Pd based Al_2O_3 catalysts.

Next, I focused on the use of CeO_2 support as a promoter to act as an oxygen storing/releasing material due to the Ce^{4+}/Ce^{3+} redox reaction.[31,32] Figure 4.7 shows the results of NO–CO–O_2 reaction using the corresponding CeO_2-supported catalysts (see Figure 4.8 for CO conversion to CO_2). Overall, the catalytic activity of CeO_2-supported catalysts was increased compared with the Al_2O_3-supported catalysts and CO oxidation was markedly improved (Figure 4.8). Particularly, N_2 yield at 250℃ (Figure 4.7a) was dramatically improved. Pd/CeO_2 shows low N_2 yield when going to lean conditions on a stoichiometric condition (λ = 1.0). PdIn/CeO_2 showed excellent catalytic activity for a wide range of λ at 250℃, which even greater than Rh/CeO_2. This trend is more prominent at 300℃ (Figure 4.7b) However, at 350℃, the catalytic activity drastically decreased for a high λ of 1.5. On the contrary, $(Pd_{0.5}Pt_{0.5})In$ exhibited a remarkably high N_2 yield even under this harsh condition (Figure 4.7c); therefore, some positive hybrid effect of substituted Pt was suggested. Although Pt/CeO_2 also showed an improved activity at λ = 1.50, the activity turned to decrease when going to the lower λ. Thus, the pseudo-binary alloy catalyst $(Pd_{0.5}Pt_{0.5})In$ exhibited the best catalytic performance under wide ranges of oxygen concentration and temperature. A physical mixture of PdIn/CeO_2 and Pt/CeO_2 was also tested to clarify the effect of Pd-Pt substitution at an atomic level, which showed much poorer catalytic activity. These results strongly suggest that Pd, Pt, and In should be adjacent to each other at an atomic level for the excellent catalytic performance and demonstrating the necessity of catalyst design based on the pseudo-binary alloy.

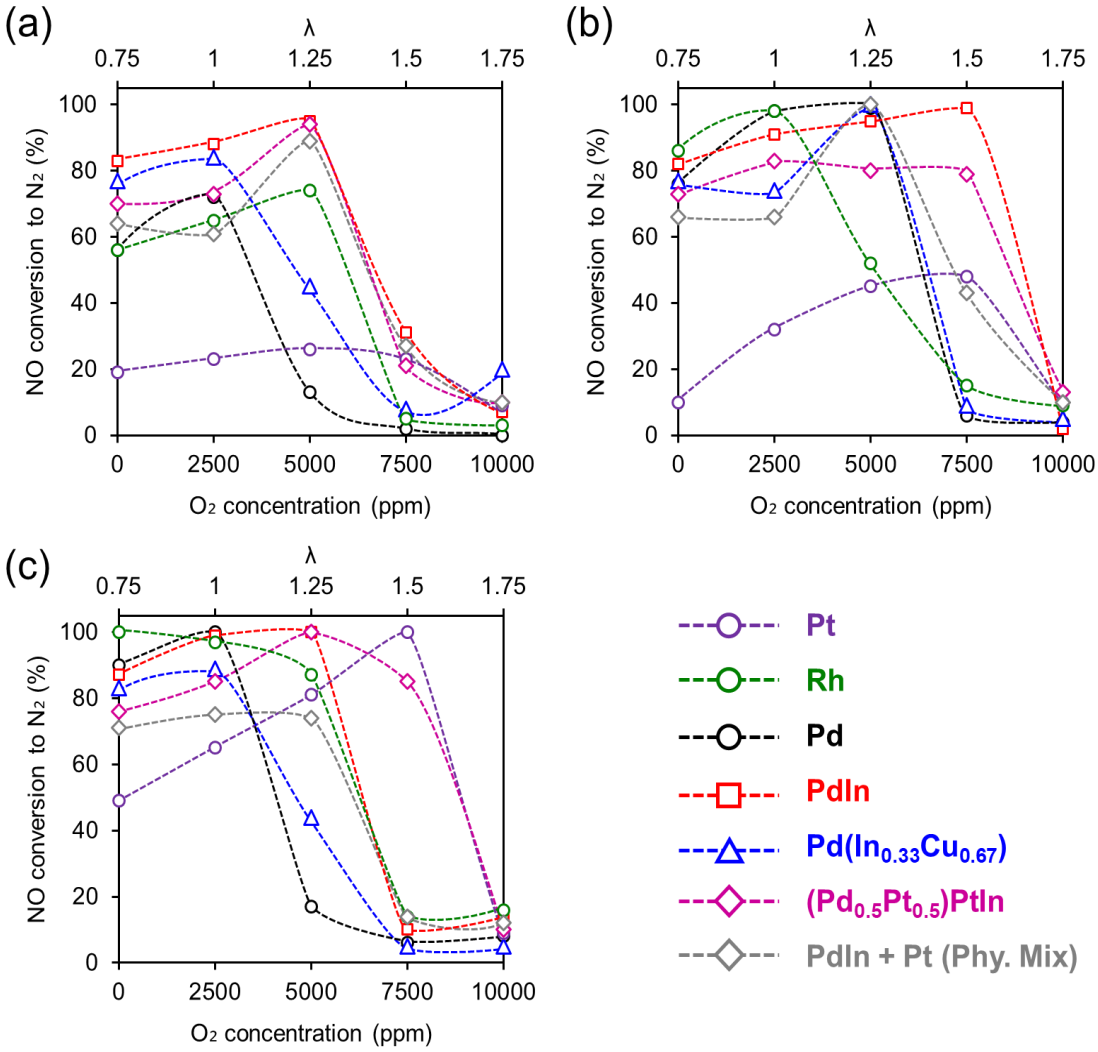

Figure 4.7. NO conversion to N_2 at (a) 250°C, (b) 300°C and (c) 350°C in NO–CO–O_2 reaction using CeO_2-supported catalysts.

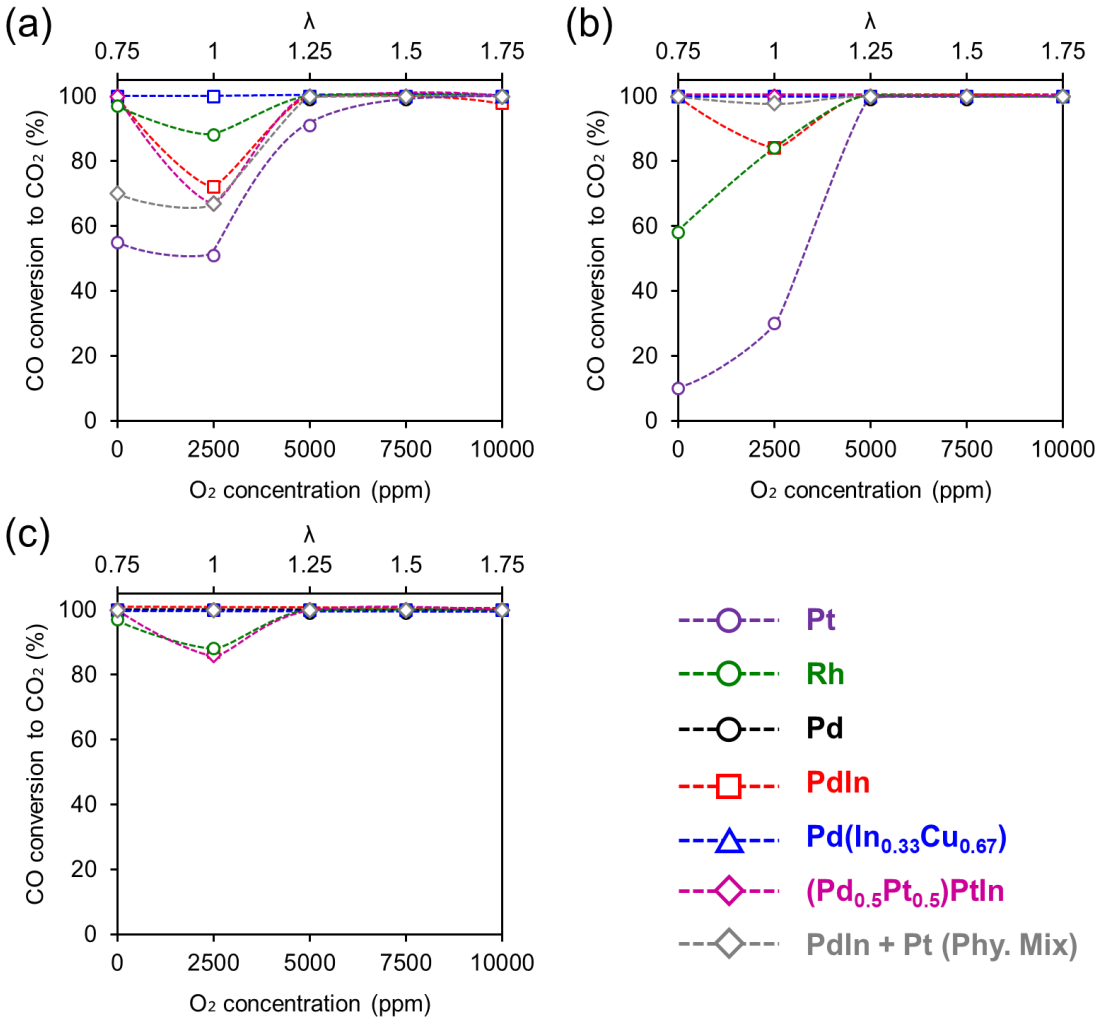

Figure 4.8. CO conversion to CO_2 at (a) 250°C, (b) 300°C and (c) 350°C in NO–CO–O_2 reaction using CeO_2-supported catalysts.

The exhaust gas concentration is very variable depending on the actual driving conditions. Hence, I examined the effect of switching the oxygen concentration during NO reduction. Figure 4.9 shows the results of the lean-rich cycle test during the NO reduction over some prepared catalysts at 300℃ (the summary is shown in Figure 4.10). For the first 30 minutes under rich conditions, the reduction activity of each catalyst moderately decreased. When the reaction conditions were changed from rich to lean, Pd/Al_2O_3 showed increased N_2O yield. After several iterations, the same behavior was observed (Figure 4.9a). By contrast, $PdIn/Al_2O_3$ catalyst exhibited different catalytic behavior. Although NO conversion was low, the N_2 yield was retained even after several cycles (Figure 4.9b). Moreover, the performances in the lean and rich conditions were not so different. Figure 4.9c, d, e, and f show the corresponding results of the CeO_2-supported catalysts. As shown in Figure 4.9c and d, Pd/CeO_2 exhibited higher NO conversion than $PdIn/CeO_2$. However, Pd/CeO_2 showed a significant drop in catalytic activity and N_2 selectivity under lean condition compared with the rich condition. A similar trend was also observed for Rh/CeO_2. On the contrary, $(Pd_{0.5}Pt_{0.5})In$ exhibited a good catalytic activity and N_2 selectivity under both conditions without significant change. Thus, the pseudo-binary alloy catalyst showed high stability and steady performance under a variable condition, which is highly important for practical use.

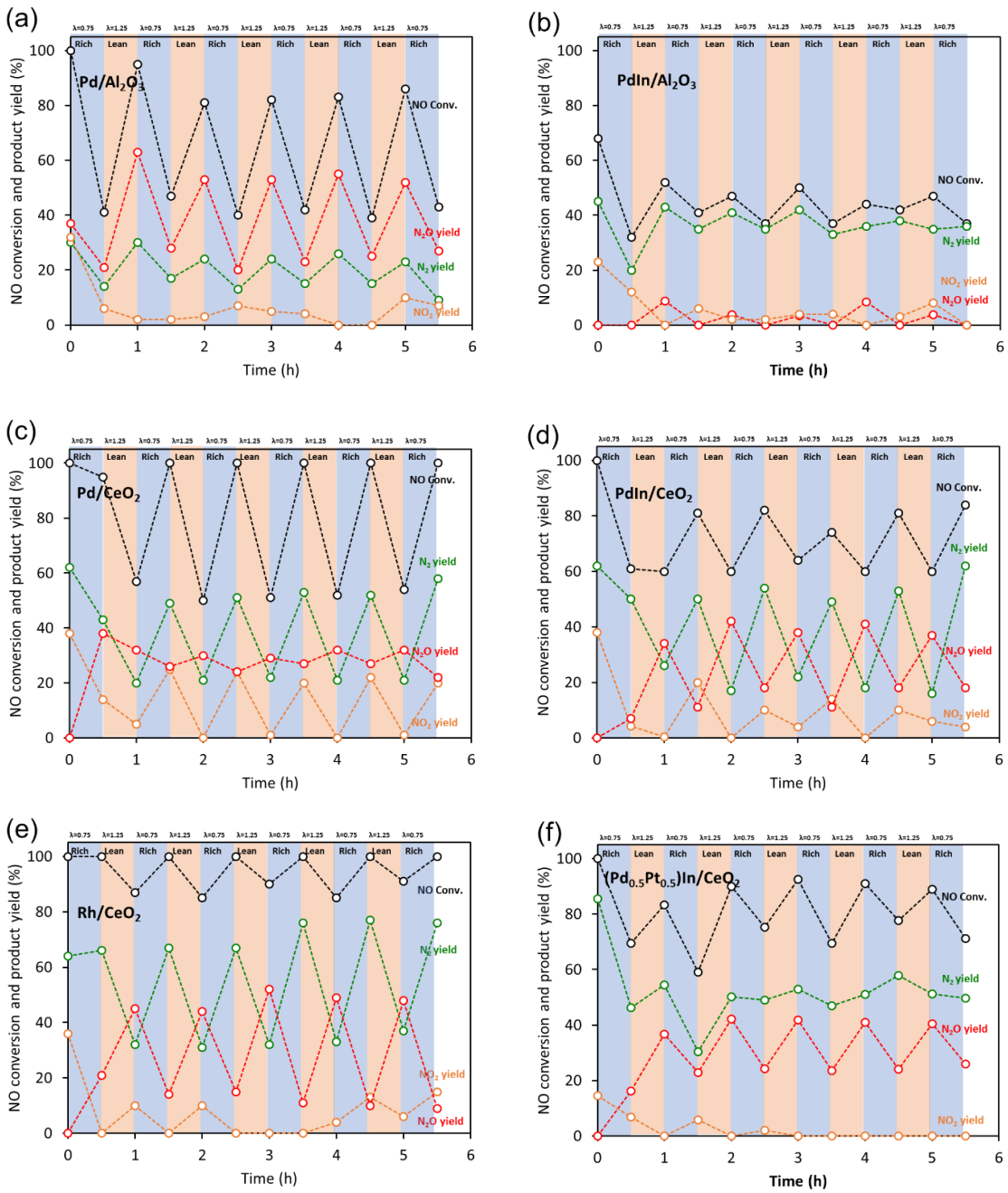

Figure 4.9. NO reduction during lean-rich cycle test over (a) Pd/Al_2O_3, (b) $PdIn/Al_2O_3$, (c) Pd/CeO_2, (d) $PdIn/CeO_2$, (e) Rh/CeO_2 and (f) $(Pd_{0.5}Pt_{0.5})In/CeO_2$ at 300°C.

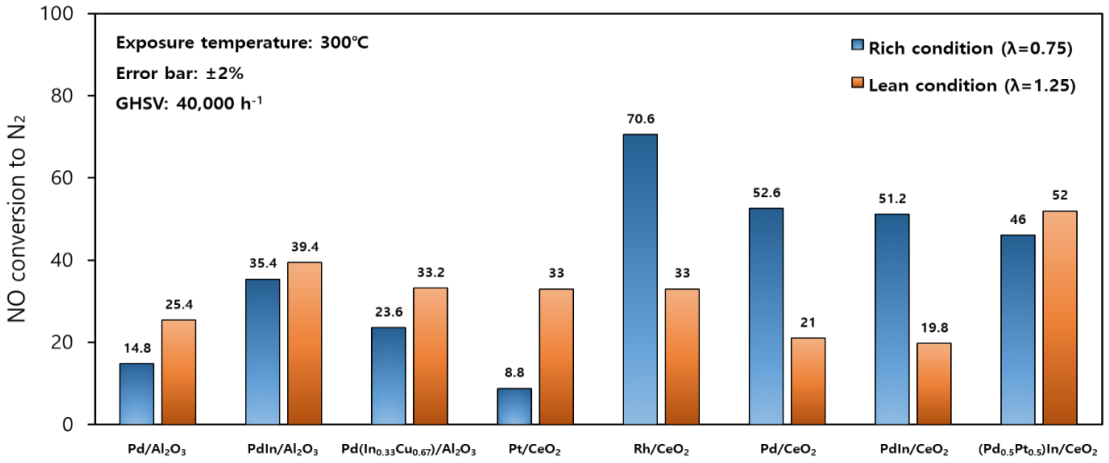

Figure 4.10. Summary of the lean-rich cycle test using prepared catalysts.

4.3.3 NO–CO–O_2–C_3H_6 reaction under excessive O_2

I tested the catalytic performance of prepared catalysts in NO–CO–O_2–C_3H_6 reaction, which is close to the real exhaust gas composition. Figure 4.11 shows the temperature dependence of NO conversion to N_2 in NO–CO–O_2–C_3H_6 reaction ($\lambda = 1.0$) using Pd based Al_2O_3-supported catalysts. Generally, since propylene (C_3H_6) is adsorbed on surface metal sites more strongly than CO and NO, NO reduction to N_2 is suppressed in the presence of propylene than in the absence. Therefore, the higher reaction temperature is needed to obtain high conversion in NO–CO–O_2–C_3H_6 reaction than NO–CO and NO–CO–O_2 reaction. This trend can be clearly observed in Figure 4.11.

Next, I also tested the catalytic performance of prepared catalysts in NO–CO–O_2–C_3H_6 reaction in the presence of excess O_2 as shown in Figure 4.12. For Pd/Al_2O_3 (Figure 4.12a), the catalytic activity increased with increasing temperature and decreased rapidly in a lean condition. A similar result was also reported in the literature. In the case of $PdIn/Al_2O_3$ (Figure 4.12b), the catalytic activity was improved in the rich condition region of 250°C. As the temperature increased to a high temperature, the catalytic activity was further improved in the lean condition region. The catalytic activity of the $PdIn/Al_2O_3$ was greatly improved by using CeO_2 as support (Figure 4.12c). By comparing $PdIn/CeO_2$ and $(Pd_{0.5}Pt_{0.5})In/CeO_2$, $PdIn/CeO_2$ showed the highest catalytic activity in rich conditions below 300°C. The improvement in the

catalytic activity in lean condition was also exhibited at 350℃ and the higher, as well as that of PdIn/Al_2O_3. However, a further increase in temperature (> 400℃) resulted in a significant drop of the N_2 yield. On the contrary, ($Pd_{0.5}Pt_{0.5}$)In/CeO_2 (Figure 4.12d) exhibited excellent catalytic performance in a wide range of λ even at high-temperature region (> 400℃). Thus, the pseudo-binary alloy catalyst was also effective in NO–CO–O_2–C_3H_6 reaction.

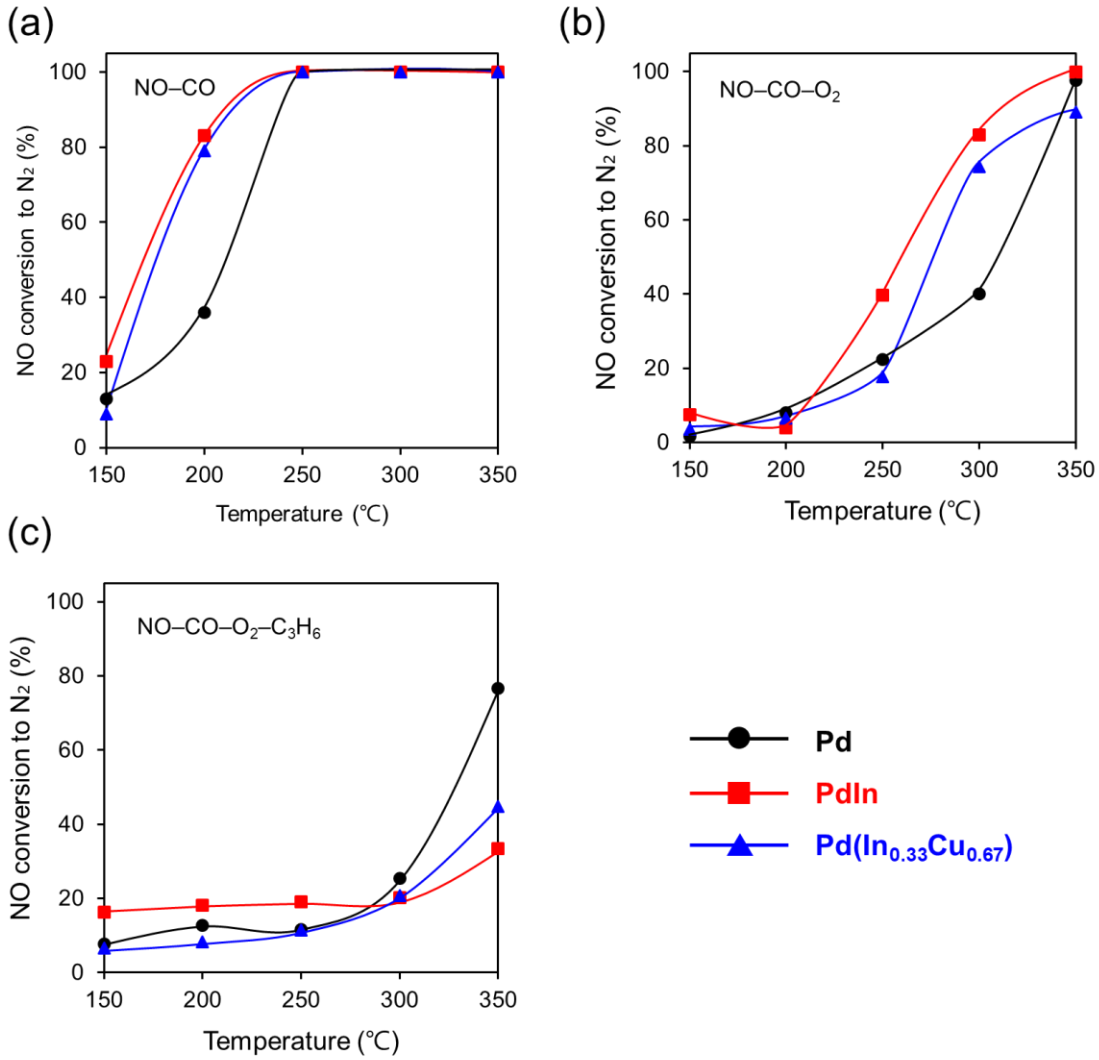

Figure 4.11. Temperature dependence of NO conversion to N_2 in (a) NO–CO reaction, (b) NO–CO–O_2 reaction and (c) NO–CO–O_2–C_3H_6 reaction using Pd based Al_2O_3-supported catalysts.

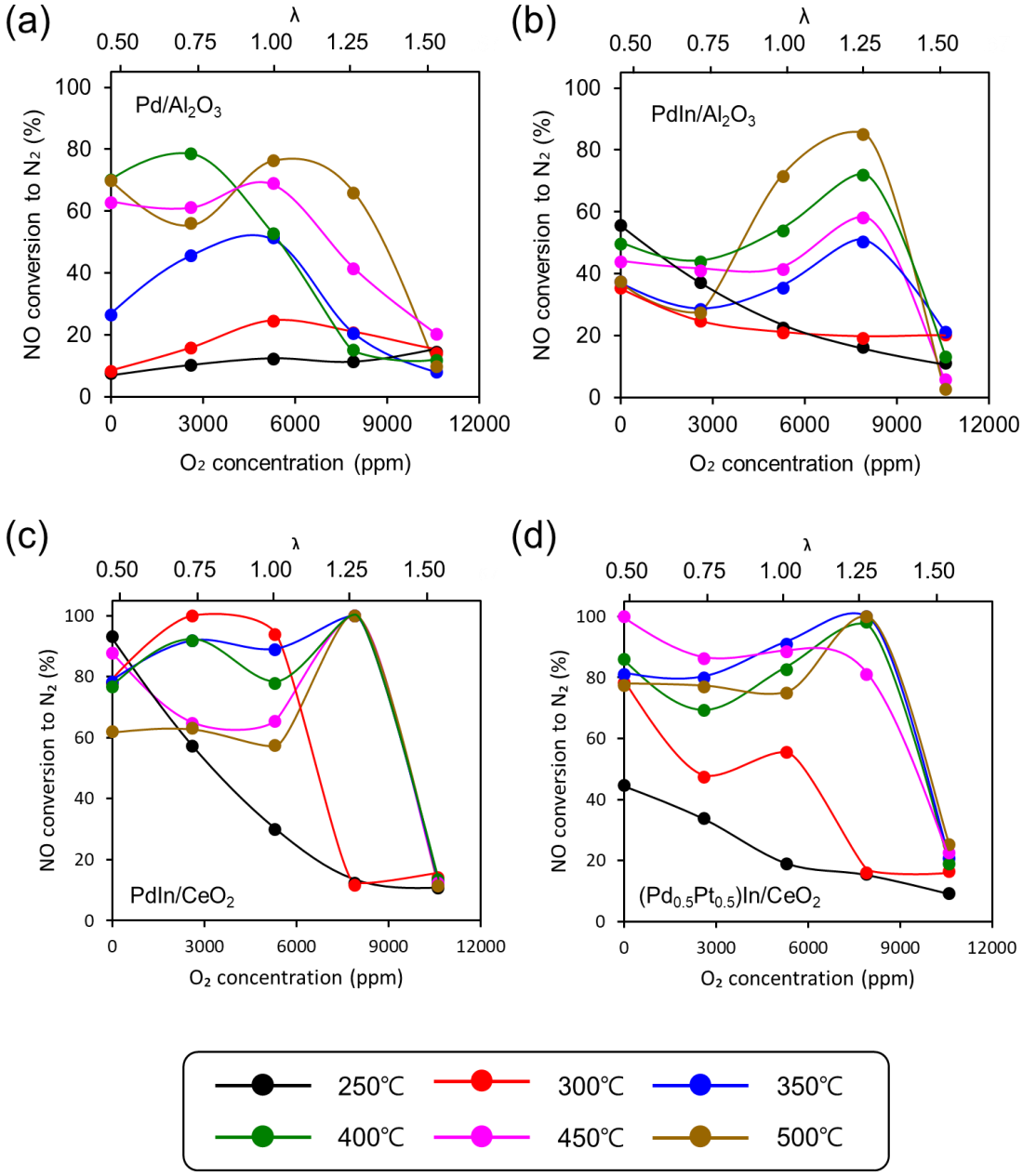

Figure 4.12. NO conversion to N_2 profile of (a) Pd/Al_2O_3, (b) $PdIn/Al_2O_3$ (c) $PdIn/CeO_2$ and (d) $(Pd_{0.5}Pt_{0.5})In/CeO_2$ catalysts under NO–CO–O_2–C_3H_6 reaction.

4.3.4 Discussion on NO conversion under lean condition

As shown in Chapter 2, CO oxidation is the rate-determining step (RDS) in NO reduction by CO in the low-temperature region (< 225℃). In contrast to the low-temperature region (< 225℃), N–O bond dissociation is the RDS at high-temperature region (> 250℃).[22] Considering the temperature range focused in Chapter 4, the RDS might be the N–O dissociation step. For NO–CO–O_2 reaction, In atom and CeO_2 support act as acceptors of oxygen during the reaction, which could accelerate N–O dissociation and improve CO oxidation efficiency, thereby enhancing the overall reaction rate (Figure 4.13). Moreover, In also accept oxygen atoms from O_2, which would provide improved oxygen tolerance: greater catalytic performance in lean conditions. The incorporation of Pt further improved the oxidation tolerance of PdIn. This may be explained by enhanced redox property of In by Pt. Reduction of oxygen captured In (indium oxide species) to metallic In would be accelerated by CO on Pt. However, for NO–CO–O_2–C_3H_6 reaction, C_3H_6 is adsorbed on surface active sites more strongly than CO and NO; therefore, NO adsorption on metallic sites is inhibited by competitive adsorption of C_3H_6.[33] Higher reaction temperature is required to remove C_3H_6 by combustion so that the reaction site for NO reduction is liberated. On the contrary, incorporation of Pt, which has strong combustion ability for hydrocarbon, to PdIn promotes oxidation of C_3H_6, which accelerates NO reduction under lean condition.

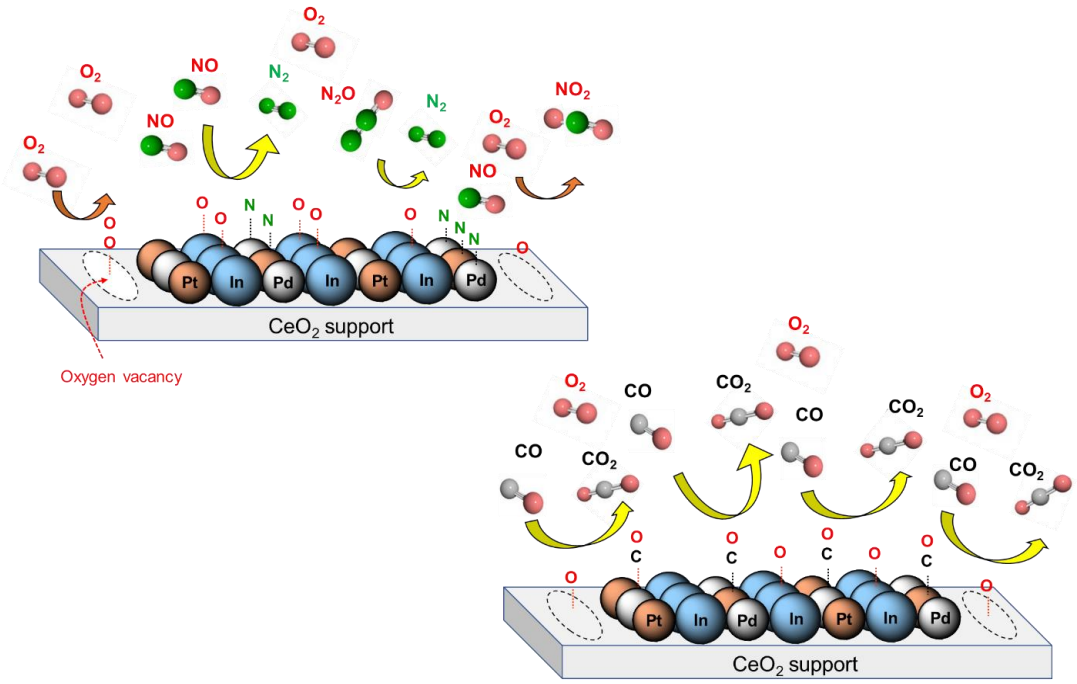

Figure 4.13. Scheme of redox mechanism of $(Pd_{0.5}Pt_{0.5})In/CeO_2$ catalyst.

4.4 Conclusion

In summary, I developed a Pd-based pseudo-binary alloy catalyst for deNO_x in lean conditions. The catalytic performance of PdIn catalyst was further improved by substituting a part of Pd with Pt, where a $(Pd_xPt_{1-x})In$ pseudo-binary alloy structure was formed. The formation of the pseudo-binary alloy structure was confirmed by the combination of HAADF-STEM-EDS and FT-IR analyses. The optimized catalyst, $(Pd_{0.5}Pt_{0.5})In/CeO_2$, improved the N_2 yield (80%) even in the presence of excess oxygen (from rich λ= 0.75 to lean λ =1.50), which allowed to expand the operating window of NO–CO–O_2 reaction. This catalyst also exhibited high purification efficiency in NO–CO–O_2–C_3H_6 reaction with a wide range of operating widow. The adjacency of three elements (Pd, Pt, and In) in an atomic level provides individual roles in catalysis to the active site; Pd: NO_x reduction, In: N_2O decomposition for high selectivity to N_2, oxygen acceptor, and redox property, Pt: hydrocarbon combustion and redox promoter for In. The catalyst design based on pseudo-binary alloy enables the combination of these positive effects, which allows to develop a highly efficient catalytic system of deNO_x reaction under lean conditions.

References

1. B. K. Bose, L. Fellow and C. Science, *IEEE Ind. Electron. Mag.*, 2010, **1**, 6–17.
2. K. Skalska, J. S. Miller and S. Ledakowicz, *Sci. Total Environ.*, 2010, **408**, 3976–3989.
3. I. Nova, L. Lietti and P. Forzatti, *Catal. Today*, 2008, **136**, 128–135.
4. S. Du, S. Wang, Y. Guo, X. Lu, W. Tang, Y. Ding, X. Mao and P. X. Gao, *Appl. Catal. B Environ.*, 2018, **236**, 348–358.
5. S. A. Malamis, M. Li, W. S. Epling and M. P. Harold, *Appl. Catal. B Environ.*, 2018, **237**, 588–602.
6. Z. Zhou, M. P. Harold and D. Luss, *Appl. Catal. B Environ.*, 2019, **240**, 79–91.
7. Q. Zhang, L. Lv, J. Zhu, X. Wang, J. Wang and M. Shen, *Catal. Sci. Technol.*, 2013, **3**, 1069–1077.
8. L. Wang, C. Yin and R. T. Yang, *Appl. Catal. A Gen.*, 2016, **514**, 35–42.
9. T. Liu, Y. Yao, L. Wei, Z. Shi, L. Han, H. Yuan, B. Li, L. Dong, F. Wang and C. Sun, *J. Phys. Chem. C*, 2017, **121**, 12757–12770.
10. B. Wen, *Fuel*, 2002, **81**, 1841–1846.
11. Z. Hu, C. Z. Wan, Y. K. Lui, J. Dettling and J. J. Steger, *Catal. Today*, 1996, **30**, 83–89.
12. M. Fernández-García, A. Iglesias-Juez, A. Martínez-Arias, A. B. Hungría, J. A. Anderson, J. C. Conesa and J. Soria, *J. Catal.*, 2004, **221**, 594–600.
13. H. Asakura, T. Onuki, S. Hosokawa, N. Takagi, S. Sakaki, K. Teramura and T. Tanaka, *Phys. Chem. Chem. Phys.*, 2019, **21**, 18816–18822.
14. K. Ueda, M. Tsuji, J. Ohyama and A. Satsuma, *ACS Catal.*, 2019, **9**, 2866–2869.
15. T. Kobayashi, T. Yamada and K. Kayano, *Appl. Catal. B Environ.*, 2001, **30**, 287–292.
16. M. Shelef and G. W. Graham, *Catal. Rev.*, 1994, **36**, 433–457.
17. H. S. Gandhi, G. W. Graham and R. W. McCabe, *J. Catal.*, 2003, **216**, 433–442.
18. R. J. Farrauto, M. Deeba and S. Alerasool, *Nat. Catal.*, 2019, **2**, 603–613.
19. Y. Nagao, Y. Nakahara, T. Sato, H. Iwakura, S. Takeshita, S. Minami, H. Yoshida and M. Machida, *ACS Catal.*, 2015, **5**, 1986–1994.
20. H. Y. Chen and H. L. R. Chang, *Johnson Matthey Technol. Rev.*, 2015, **59**, 64–67.
21. S. Furukawa and T. Komatsu, *ACS Catal.*, 2017, **7**, 735–765.
22. J. Jeon, K. ichi Kon, T. Toyao, K. ichi Shimizu and S. Furukawa, *Chem. Sci.*, 2019, **10**, 4148–4162.
23. F. Xing, J. Jeon, T. Toyao, K. Shimizu and S. Furukawa, *Chem. Sci.*, 2019, **10**, 8292-8298.
24. B. Ravel and M. Newville, *J. Synchrotron Radiat.*, 2005, **12**, 537–541.
25. I. R. Harris, M. Norman and A. W. Bryant, *J. Less-Common Met.*, 1968, **16**, 427–440.
26. L. Pauling, *J. Am. Chem. Soc.*, 1947, **69**, 542–553.
27. W. K. Kuhn, J. Szanyi and D. W. Goodman, *Surf. Sci.*, 1992, **274**, L611-L618.

28. C. De La Cruz and N. Sheppard, *Spectrochim. Acta Part A Mol. Spectrosc.*, 1994, **50**, 271–285.
29. Y. Cao, Z. Sui, Y. Zhu, X. Zhou and D. Chen, *ACS Catal.*, 2017, **7**, 7835–7846.
30. R. M. Navarro, B. Pawelec, J. M. Trejo, R. Mariscal and J. L. G. Fierro, *J. Catal.*, 2000, **189**, 184–194.
31. P. Bera, A. Gayen, M. S. Hegde, N. P. Lalla, L. Spadaro, F. Frusteri and F. Arena, *J. Phys. Chem. B*, 2003, **107**, 6122–6130.
32. P. Fornasiero, M. Graziani and J. Kaspar, *Catal. Today*, 1999, **50**, 285–298.
33. H. Jeong, G. Lee, B. S. Kim, J. Bae, J. W. Han and H. Lee, *J. Am. Chem. Soc.*, 2018, **140**, 9558–9565.

Chapter 5

General Conclusion

In this research, I focused on selective NO_x reduction for exhaust gas purification. For this purpose, pseudo-binary alloy and single atom alloy systems were applied as a novel catalyst design. Application to this system achieved the development of highly active and selective NO_x reduction to N_2 (N_2 yield: 100%) in the low-temperature region (below the 200°C). Besides, CeO_2 supported Pd based catalysis was found to be more effective for NO reduction in a lean condition. The developed catalyst showed higher N_2 yield than previous mono- and bi-metal catalyst for deNO_x reactions in a lean condition. These newly developed bi- and tri-metallic materials will provide effective post-treatment catalysts for automobiles and environmentally friendly technology.

Chapters 2, 3 conclude that a Pd based alloy, Pd($In_{0.33}Cu_{0.67}$) and Cu_5Pd, effectively catalyzed NO reduction by CO with high N_2 selectivity at low temperatures. In the case of the Pd($In_{0.33}Cu_{0.67}$) system, In accelerates CO oxidation, which is the RDS at the low-temperature region, thus providing a higher number of vacant active sites for NO dissociation and N_2O decomposition. Cu improves NO adsorption and dissociation. Thus, the combination of the positive effects of In and Cu enables the development of a highly active and selective NO reduction by CO at various temperature regions. For the Cu_5Pd system, the N-O bond scission of $(NO)_2$ dimer is the RDS in NO reduction by CO. This step is kinetically facilitated by the isolated Pd atoms. Besides, N_2O decomposition to N_2 smoothly proceeds on the Cu surface, which contributes to the excellent N_2 selectivity observed for Cu_5Pd catalyst. Thus, the sufficient isolation of Pd atoms by Cu enables the highly active and selective NO reduction by CO.

Chapters 4 concludes that a PdPt based pseudo-binary alloy, ($Pd_{0.5}Pt_{0.5}$)In, effectively catalyzed the NO reduction by CO in a lean condition. Substituted Pt in this alloy structure provided an expanded operating window for the three-way catalytic system. Moreover, the combination of the positive effects of Pt and PdIn enabled the development of highly active and selective NO reduction by CO at various O_2 concentrations and temperatures.

In summary, the newly developed alloy structures are capable of drastically improving the catalytic performance of Pd in selective deNO_x reactions. Atomically aligned two or three kinds of metal elements provide different promotion effects in catalysis and their synergy to realize the highly challenging molecular conversion. This

study provides not only highly efficient catalytic systems for selective deNO_x but also important insights of catalyst design based on alloy materials for efficient catalysis.

List of publication

1. Paper (related to this thesis)

1. Jaewan Jeon, Ken-ichi Kon, Takashi Toyao, Ken-ichi Shimizu, Shinya Furukawa, "Design of Pd-based pseudo-binary alloy catalysts for highly active and selective NO reduction" *Chemical Science.*, 2019, 10, 4148-4162. (Selected as the Back Cover)

2. Feilong Xing, Jaewan Jeon, Takashi Toyao, Ken-ichi Shimizu, Shinya Furukawa, "A Cu-Pd single atom alloy catalyst for highly efficient NO reduction" *Chemical Science*, 2019, 10, 8292-8298. (Selected as the Front Cover & a HOT article) (Highlighted in Chemistry World)

2. Other Paper (not related to this thesis)

1. Md. Nurnobi Rashed, Abeda Sultana Touchy, Chandan Chaudhari, Jaewan Jeon, S. M. A. Hakim Siddiki, Takashi Toyao, Ken-ichi Shimizu, "Selective 3-alkenylation of oxindole with aldehydes using heterogeneous CeO_2 catalyst" *Chinese Journal of Catalysis*, 2020, 41, 970-976.

2. Woosung Choi, Kyungmin Min, Chaehoon Kim, Young Soo Ko, Jaewan Jeon, Hwimin Seo, Yong-Ki Park, Minkee Choi, "Epoxide-functionalization of polyethyleneimine for synthesis of stable carbon dioxide adsorbent in temperature swing adsorption" *Nature communications*, 2016, 7(1), 1-8.

3. Jaewan Jeon, Young Soo Ko, "Synthesis of CO_2 Adsorbent with Various Aminosilanes and its CO_2 Adsorption Behavior" *Applied Chemistry for Engineering*, 2016, 27(1), 80-85

3. International Conferences

1. Shinya Furukawa, Jaewan Jeon, Kenichi Kon, Ken-ichi Shimizu, "Design of palladium-based alloy catalyst for highly active and selective NO reduction" APCAT-8, Oral, Aug. 4-7, 2019, Bangkok, Thailand

2. Jaewan Jeon, Kenichi Kon, Takashi Toyao, Ken-ichi Shimizu, Shinya Furukawa, "Highly active and selective deNO_x catalyst using $Pd(In_{1-x}Cu_x)Al_2O_3$

pseudo-binary alloy" Cardiff Catalysis Institute-Hokkaido ICAT Joint International Symposium on Catalysis, Poster, Jan. 16, 2019, Cardiff, UK

3. Jaewan Jeon, Shinya Furukawa, Kenichi Kon, Ken-ichi Shimizu, "Selective deNO_x catalysts using Pd-based intermetallic compounds supported on Al_2O_3" TOCAT-8, Poster, Aug. 5-10, 2018, Yokohama, Japan

4. Jaewan Jeon, Shinya Furukawa, Kenichi Kon, Ken-ichi Shimizu, "Development of highly selective Pd based alloy catalysts for deNO_x reaction" Pre-conference of TOCAT8 and the 5th International Symposium of Institute for Catalysis, Poster, Aug. 3-4, 2018, Institute for Catalysis, Hokkaido University, Japan

4. Domestic Conferences

1. Jaewan Jeon, Ken-ichi Shimizu, Shinya Furukawa, "Highly efficient deNO_x systems using pseudo-binary alloys as catalysts" 第５回統合物質機構シンポジウム, Poster, Nov. 12, 2019, Institute for Catalysis, Hokkaido University, Japan

2. Feilong Xing, Jaewan Jeon, Ken-ichi Shimizu, Furukawa Shinya, "Cu-Pd single-atom alloy catalyst for highly efficient deNO_x at low temperatures" Summer presentation meeting, Chemical Society of Japan, Hokkaido branch, Oral, July. 20, 2019, National Institute of Technology, Tomakomai College, Japan

3. Shinya Furukawa, Jaewan Jeon, Kenichi Kon, Ken-ichi Shimizu, "NO-CO 反応に高い活性選択性を示す$Pd(In_{0.33}Cu_{0.67})$擬二元系合金の開発とその作用機構"
123th Meeting of Catalysis Society of Japan, Oral, Mar. 20-21, Osaka City University, Japan

4. Jaewan Jeon, Kenichi Kon, Takashi Toyao, Ken-ichi Shimizu, Shinya Furukawa, "Design of Pd-based alloy catalysts for Highly active and selective NO reduction" 10th KSEA Subcommittee, Poster, Korean Scientists and Engineers Association in Japan, Feb. 11, 2019, Korean Embassy in Japan, Japan

5. Feilong Xing, Jaewan Jeon, Ken-ichi Shimizu, Shinya Furukawa, "Highly active and selective deNO_x catalysts using Cu-Pd alloys" Winter presentation meeting, Oral, Chemical Society of Japan, Hokkaido branch, Jan. 22-23, 2019, Hokkaido University, Japan

6. Jaewan Jeon, Shinya Furukawa, Kenichi Kon, Ken-ichi Shimizu, “Highly active and selectivity deNO_x catalyst using PdIn intermetallic compound” Winter presentation meeting, Oral, Chemical Society of Japan, Hokkaido branch, Jan. 22-23, 2019, Hokkaido University, Japan

7. Jaewan Jeon, Shinya Furukawa, Kenichi Kon, Ken-ichi Shimizu, “NO–CO反応に高い選択性を示すPd系合金触媒の開発”122th Meeting of Catalysis Society of Japan, Oral, Sep. 26-28, 2018, Hokkaido University of Education, Hakodate Campus, Hokkaido, Japan

8. Feilong Xing, Jaewan Jeon, Shinya Furukawa, Ken-ichi Shimizu, “Highly active and selective deNO_x catalysts using Cu-Pd alloys” The 58th Aurora seminar, Chemical Society of Japan, Hokkaido branch, Poster, Jul. 8-9, 2018, Hokkaido, Japan

9. Jaewan Jeon, Shinya Furukawa, Kenichi Kon, Ken-ichi Shimizu, “Pd-based intermetallic compound catalyst effective for NO–CO reaction” Winter presentation meeting, Oral, Chemical Society of Japan, Hokkaido branch, Jan. 23-24, 2018, Hokkaido University, Japan

10. Jaewan Jeon, Shinya Furukawa, Kenichi Kon, Takashi Toyao, Ken-ichi Shimizu, “Pd系金属間化合物上でのNO–CO反応におけるN_2選択性の変化” The 57th Aurora seminar, Chemical Society of Japan, Hokkaido branch, Poster, Jul. 23-24, 2017, Hokkaido, Japan

Acknowledgments

I am extremely grateful to all those who helped me to concentrate on the study the Institute for Catalysis at Hokkaido University as a doctoral student. I am deeply grateful to Graduate school of Chemical Science and Engineering (CSE) I would like to acknowledge the AGS (Advanced Graduate School) scholarship for financial support.

First of all, I am extremely appreciative of my supervisor Professor Shinya Furukawa. He gives me not only fundamental background of metallic alloy catalysts but also serves as a paragon, demonstrating the attitude of a true scientist. I would like to acknowledge the opportunity to study in Japan as a Ph.D. student. It was a great privilege to be one of the members of the Catalyst Material Research Division.

I would also like to express my gratitude to the advisory committee members, Professor Ken-ichi Shimizu, Professor Jun-ya Hasegawa, and Professor Atsushi Fukuoka for their invaluable suggestions and advice.

I would also like to express my deep appreciation to FOHRED members, Professor Takuya Yoshihara, Professor Yoshichika Iida, and Professor Naoki Higuchi for their counselling job search in japan.

I am much indebted to Professor Young Soo Ko who was my supervisor during my undergraduate & master's program at the Kongju National University. He is my mentor and inspires me to continue researching ceaselessly. I would also like to thank Professor Jong-Ki Jeon of the Kongju National University for providing valuable comments and learning motivation of fundamental catalysts.

In addition, I would like to express my deep appreciation to our staff for their help with the initial experimental introduction and taking care of the huge obstacles that I faced in my daily life. I will never forget the good memories and friendships with Shimizu laboratory members that were formed. I am really happy to have met our lab members. Moreover, I also thank Won-tae Kim who is motivated to graduate together this year. He gave me a lot of advice in sapporo life. I truly cheer him up. I also thank Dong-Geun Lee who now works in the USA as a post-doc. and Cheong Kim who now works in Hokkaido University as a post-doc.

I would also like to thank the members of the Korean Student Association in Hokkaido University.

My gratitude extends to Dong-woo Lee, Jae-hun Jeong, Ho-Jun Song, Jong-Tak Do, Sung-Heuk Choi, and Sung-Jin Choi. They have always answered my calls warmly to help to mitigate my homesickness. I am proud of them as they are my precious friends. My fiancée Ayaka Tanimoto, thank you for supporting me mentally for 3 years with my Ph.D. course.

Last, but not least, I would like to give special thanks to my beloved family. They always gave me their full emotional support. I would like to dedicate my thesis to my family.

Jaewan Jeon